

International WOCE Newsletter



Number 31

ISSN 1029-1725

June 1998

IN THIS ISSUE

❑ Guest Editorial

- Ocean Circulation and Climate – The WOCE Conference *John A. Church* 2

❑ Data Assimilation

- Toward an Estimate of the Global Circulation from WOCE Data
and a General Circulation Model *Detlef Stammer* 7
- Data Assimilation for Australian Climate Variability Studies *Peter McIntosh and Andreas Schiller* 10
- Assimilation of TOPEX Data into the OCCAM Model *A. Fox, et al.* 12

❑ Technology Developments

- The Along Track Scanning Radiometer Programme *Chris Mutlow* 42
- At-Sea Test of a New XCTD System *Alexander Sy* 45

❑ General Science

- Did the Overflow from the Nordic Seas Intensify in 1996–1997? *Michael McCartney, et al.* 3
- The Rate of Formation of the Subtropical Underwater (STUW)
in the North and South Pacific from Drifter and Tracer Data *Bridgette M. O'Connor, et al.* 18
- South Atlantic Chlorofluoromethane Distributions
Along the WHP Lines A17, A13 and A14 *Marie-José Messias and Laurent Memery* 21
- Heat Flux Estimates Across A6 and A7 WOCE Sections *F. Marin, et al.* 28
- Lagrangian and Infrared Observations of Surface Currents
in the Brazil-Malvinas Confluence Zone, 1993–1994 *Ronald Buss de Souza and Ian S. Robinson* 32
- Water Mass Transformation Theory and the
Meridional Overturning Streamfunction *A. J. G. Nurser and R. Marsh* 36
- Cruise 36 of RV Professor Shtokman to the North Atlantic *A. V. Sokov and V. P. Tereschenkov* 39
- TOPEX/POSEIDON Altimetry Captures Cycles of the Indian Ocean *Steven D. Meyers, et al.* 41

❑ Miscellaneous

- Ocean Model Data Storage *Peter McIntosh* 16
- Erratum *Eric Firing* 20

❑ Meetings

- WOCE Indian Ocean Workshop 15
- First Announcement: WOCE-AIMS Tracer Workshop 17
- WOCE/CLIVAR Workshop on Ocean Modelling for Climate Studies 31
- Summary of a GODAE/WOCE Meeting on
Large-Scale Ocean State Estimation *D. Stammer, et al.* 38

Ocean Circulation and Climate – The WOCE Conference

*John A. Church, WOCE SSG Co-Chair, CSIRO Division of Marine Research, Hobart, Tasmania, Australia.
john.church@marine.csiro.au*

The WOCE Conference, Ocean Circulation and Climate, held in Halifax, Canada, 24–29 May was a stimulating meeting for the 380 attendees from 29 countries. The Conference was a celebration of the success of the observational phase of WOCE, an opportunity to assess our current state of knowledge of the ocean circulation and its relation to climate, and an opportunity to refocus on what needs to be done to meet the WOCE goals of developing and testing ocean models useful for predicting climate and providing the basis for the rational design of future ocean observing systems.

Highlights of the WOCE Conference included the distribution to all of the Conference attendees a set of 16 CD-ROMs of WOCE data, the series of invited overview talks and 320 posters.

WOCE data sets distributed

The production of the CD-ROM data set covering all of the WOCE data streams is a significant achievement. Credit for this success must go to the Data Products Committee, particularly its retiring Chair Eric Lindstrom, all of the Data Assembly Centres and Special Analysis Centres, and the individual PIs who provided data sets and products. Additional sets of the CD-ROMs will be available from the WOCE IPO. A second and third set of CD-ROMs of WOCE data are planned for release over the next few years. These CD-ROMs are an opportunity for those who have not yet submitted their data to have it included within the global data set. Plans are in place by the WOCE Atlas Committee in conjunction with individual PIs for the compilation of atlases of the WOCE data sets which will be available on the WWW, on CD-ROMs and eventually in hard-copy form.

High quality posters

The posters were of high quality, covered an impressive range of ocean science and, if the animated discussion occurring during the poster sessions was any guide, generated considerable interest and enthusiasm among the participants. They covered the full spectrum of WOCE activities including a set of posters on ocean carbon storage and fluxes. Electronic versions of the posters are currently being linked to the WOCE IPO web page where they can be viewed at

www.soc.soton.ac.uk/OTHERS/woceipo/wconf/posters

Documenting understanding of ocean circulation and climate

A book tentatively titled “Ocean Circulation and Climate” is planned. The book will be edited by Gerold Siedler and myself and is designed to present our current state of knowledge of the role of ocean circulation in climate. The book will include contributions from an impressive array of oceanographers, including many of the invited speakers plus additional authors to ensure a comprehensive coverage of relevant material. We anticipate publication in 1999 at a price that will allow individual purchases as well as inclusion in library collections.

Continuing the WOCE AIMS phase

However, it is also clear that much more is yet to be achieved. One example of this was the small number of heat flux estimates that have been made from the WOCE data sets. Assembly and analysis of the WOCE data must continue with a growing emphasis of integrating different data streams, looking at the basin and global scale and using the analyses to critically test ocean models and their value for climate prediction purposes.

The SSG met briefly at Halifax and felt that there was a need for maintaining the momentum of the WOCE AIMS phase. We will continue to facilitate the AIMS phase through a programme of workshops, several of which are advertised in this edition of the Newsletter. The SSG would welcome suggestions for additional workshops that would further the achievement of WOCE goals. They were also positive about the need for a further international WOCE conference and would welcome feedback on the format and timing of such a conference.

Thank you

Finally, I would like to thank Gerold Siedler and the Scientific Organising Committee for the Conference, Allyn Clarke and the Local Organising Committee, John Gould and the Staff of the WOCE IPO, Ardenne International, and the commercial and institutional supporters of the Conference. It was the hard work and dedication of all of these people which was responsible for the success of the Conference.

John A. Church

Did the Overflow from the Nordic Seas Intensify in 1996–1997?

Michael McCartney, Woods Hole Oceanographic Institution, Woods Hole, USA; Kathy Donohue, University of Hawaii, Honolulu, USA; Ruth Curry, Woods Hole Oceanographic Institution, USA; C. Mauritzen, Service Hydrographique et Océanographique de la Marine, Brest, France; and Sheldon Bacon, Southampton Oceanography Centre, Southampton, UK.
mmccartney@whoi.edu



Warm subtropical waters are transformed to cold deep waters at higher latitudes in the North Atlantic, a meridional overturning circulation releasing considerable heat to the atmosphere. A northward-turning branch of the North Atlantic Current initiates this transformation, which occurs along two distinct pathways, one in the subpolar gyre and one farther north in the Nordic and Polar Seas. Mauritzen (1996a,b) gives a complete discussion of the circulation pathways and mean transformation rates for the latter region; here we present indirect evidence for recent changes there – indirect as the measurements are in the deep flow farther south.

A chilled remnant of the North Atlantic Current enters the Nordic Seas across the Iceland-Scotland Ridge as the initial stage of the high latitude transformation. After additional cooling and freshening along a circuit around the Nordic and Polar Seas, cold, fresh, and very dense waters spill over the Greenland-Iceland-Faroe-Scotland Ridge feeding a Deep Northern Boundary Current (DNBC) system. The dense waters entrain thermocline and intermediate waters as they descend into the DNBC and are joined by a confluence of resident deep waters into the DNBC. The Iceland-Scotland Overflow Water (ISOW) is carried by the DNBC from the Iceland Basin to the Irminger Basin through the Charlie Gibbs Fracture Zone. West of Iceland, Denmark Strait Overflow Water (DSOW) spills over the Greenland-Iceland Ridge to join the ISOW and deep waters from farther south in the western basin. The combined outflow of Nordic Seas waters is estimated as about 6 Sverdrups (Sv) near the overflow sills. The entrained thermocline and intermediate waters and the deep-water confluences approximately double the transport: the multi-year direct measurements of dense-water transport of the DNBC off Angmagssalik, Greenland by Dickson and Brown (1994) indicate an amplitude of about 11 Sv below density 27.8.

It is natural to wonder about possible shifts in the intensity of the overflows themselves as well as the water masses carried by the DNBC and its transport. Dickson and Brown (1994) reported transports that were remarkably stationary. In contrast, several investigators have documented that water-mass characteristics of the DNBC/DWBC in the Labrador Basin in the Overflow density range (beneath the local convection of Labrador Sea Water) are significantly variable (Brewer et al., 1983; Swift, 1984; Lazier, 1988). Questions linger as to whether that measured variability is interannual, decadal or partly aliased by higher frequencies. Dickson et al. (1996) link high/low North Atlantic Oscillation (NAO) index to weak/strong forcing of Nordic Seas water-mass transformation, and

strong/weak forcing of subpolar gyre water-mass formation. The NAO index reflects basin-scale changes in wind speed and direction, air temperature, and humidity; fluctuations in the NAO index thus are linked to changes in buoyancy- and wind-driven forcing. This could affect the DNBC in at least four ways. First, changes in buoyancy forcing could alter the amount as well as the salinity and temperature of water transformed into specific density ranges within the Nordic and Polar Seas and exported to lower latitudes by the Overflows. Second, changes in the wind-driven forcing could affect the nature of the large cyclonic circulation system centred on Iceland which includes (and links) the Nordic Seas and the subpolar gyre and their wind-driven exchanges. We are unaware of a study of the relative intensities and patterns of wind-driven circulation that might accompany strongly contrasting wind fields of high and low NAO index states. Third, if the overflow system involves hydraulic control, then the alterations of density structure within the Nordic Seas (“upstream”) could alter that control, including the intensity of overflow. Fourth, the amount and characteristics of warmer subpolar waters entrained into the overflows could change with NAO variations of buoyancy- and wind-forcing of the subpolar gyre and alter DNBC characteristics and transport.

Bacon (1997a,b) has examined the variability of the DNBC by estimating transports of the DSOW denser than 27.8 in the DNBC in the southern Irminger basin, south-east of Cape Farewell, Greenland. His estimates are for the most part geostrophic relative to 1000 m reference levels, but a case is made for a link to absolute transport changes. His analysis shows DSOW transports that are relatively weak in 1955–67, relatively strong in 1978–88, and relatively weak again in 1991–97, with a major data gap in 1968–77. Concentrating here on the later two of the three periods of data, the low-transport phase of 1991–97 averages 4.3 Sv, ranging roughly between 3.4 (in 1995) to 5.4 Sv (in 1991), while the high-transport phase of 1978–90 averages about 7.7 Sv with a range 6.7 to 8.7 Sv. The difference in transport in these two multi-year periods is nearly a factor of two (1.8). We report here evidence that the system may be recovering from that low-transport phase.

Bacon used a forward integration of an NAO index to visualise accumulated forcing of Nordic Seas transformation to illustrate that the ocean integrates forcing history. Here we use simple averaging of Hurrell’s NAO index (Hurrell, 1995, and personal communication 1997 for an update through winter 1996–97). The 11-year high-transport phase of the DNBC had an average NAO index of 0.56, while the 6-year low-transport phase had an average NAO index of 1.67. Both periods are thus relatively high NAO index

compared to a long 132-year average, with the early 1990's particularly high. As Bacon noted, this is suggestive of a causal link between atmospheric conditions and the intensity of the DSOW transport. It is not definitive due to a lack of a circulation scheme or process interpretation that links the DNBC intensity at a point to all the impacts of variable atmospheric forcing.

We now move to new measurements we have been involved with, in connection with the US-funded ACCE program. These data are supplemented by a UK-funded Cape Farewell section from late August 1997. We have combined the latter with two ACCE sections at nearly the same location from May 1997 and November 1996 to give a set of three Cape Farewell sections spanning about eight months. Farther north the ACCE program repeated sections in November 1996, May 1997 and October 1997 to give a set of three Angmagssalik sections spanning nearly a year, near the location of Dickson and Brown's long-term monitoring array in the 1980's and early 1990's. Fig. 1 shows the locations of the stations crossing the DNBC and interior of the Irminger Basin for all sections.

Fig. 2a,b (page 23) shows the potential-temperature distribution for the three sections at each of the two locations. The DSOW is found as a thin layer along the continental slope of eastern Greenland stretching from the abyss "uphill" to depths shallower than 2000 metres. The westward rise of the DSOW is the signature of its southward geostrophic flow relative to a mid-depth reference level. The sections are striking because the degree of onshore rise of the DSOW varies. The onshore rise seems to progressively increase during the year spanning the measurements at the Angmagssalik location, Fig. 2a, amounting to a net uplift

of the shallow onshore edge of the DSOW of about 600 metres. Associated with this uplift is a strongly enhanced vertical temperature gradient between the onshore edge of the DSOW and the overlying warmer waters of the East Greenland Current in fall, 1997. In Fig. 3a (page 23) we show potential temperature-salinity relations for the Angmagssalik stations which demonstrate a progressive freshening of the DSOW accompanying this alteration of structure. At station 71 of the October 1997 section, where the vertical temperature gradient is most extreme, a linear potential temperature-salinity relation bridges the fresh DSOW to the East Greenland Current water bypassing the normally intervening Labrador Sea Water (LSW), which has been totally "squeezed out". This may indicate enhanced vertical mixing between these waters induced by the DSOW uplift.

Estimates of transport for the three Angmagssalik sections are shown in Fig. 4. Transports for $\sigma_0 = 27.80$, (left column) indicate a progressive increase of baroclinic transport (relative to 1000 m) from 2 Sv through 4 Sv to 6 Sv. The indicated small transport ranges for each curve reflect insensitivity to details of the "bottom triangles" below the deepest common level of station pairs. Simple referencing to ADCP data breaks down the orderliness of this time-progressive transport increase, but still shows the existence of a substantial transport increase. Most of the "noise" induced by the ADCP referencing seems to occur for the lighter parts of the DSOW. Fig. 4 (right column) shows similarly estimated transports for the $\sigma_0 = 27.86$ layer, roughly coinciding with the 2.4°C (shaded on these plots). In the first two realisations there is little difference between the ADCP-referenced transports and the 1000 m referenced transports. In the third realisation they are almost uniformly offset, with ADCP referencing giving an enhancement of about 1.5 Sv. This offset occurs for the contributions involving station 71 – which was noted above as having enhanced vertical temperature gradient and an absence of LSW. The ADCP data combined with the shear indicates a strong barotropic flow associated with station 71.

At Cape Farewell differs somewhat from that at Angmagssalik. The potential temperature sections, Fig. 2b, show that a thickening of the cold DSOW and an uplifting of its onshore edge occurred between the first and second realisations, but little additional change between the second and third realisations. Potential temperature-salinity data (Fig. 3; right panel) shows some freshening of the DSOW between the first two realisations, but little additional freshening in the third realisation. The impression we get is that the initial phase of freshening observed at Angmagssalik had arrived at Cape Farewell in spring 1997, but that the very fresh phase of October 1997 observed at Angmagssalik has not reached Cape Farewell in late August 1997. Fig. 5 shows two columns of transport estimations for Cape Farewell in the same arrangement as Fig. 4. The baroclinic transport at Cape Farewell for $\sigma_0 = 27.80$ relative to 1000 m is about 3.8 Sv in November 1996, which is somewhat lower than Bacon's average of 4.3 Sv for earlier

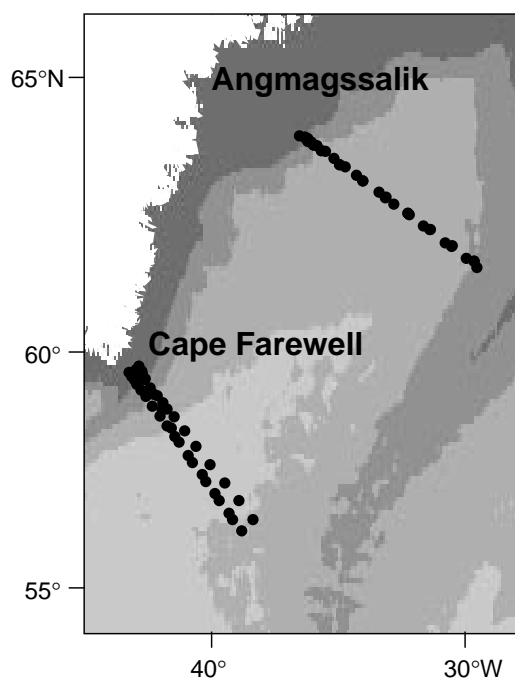


Figure 1. Positions of hydrographic stations used in this study. Bathymetry is shaded in 1000 m depth intervals.

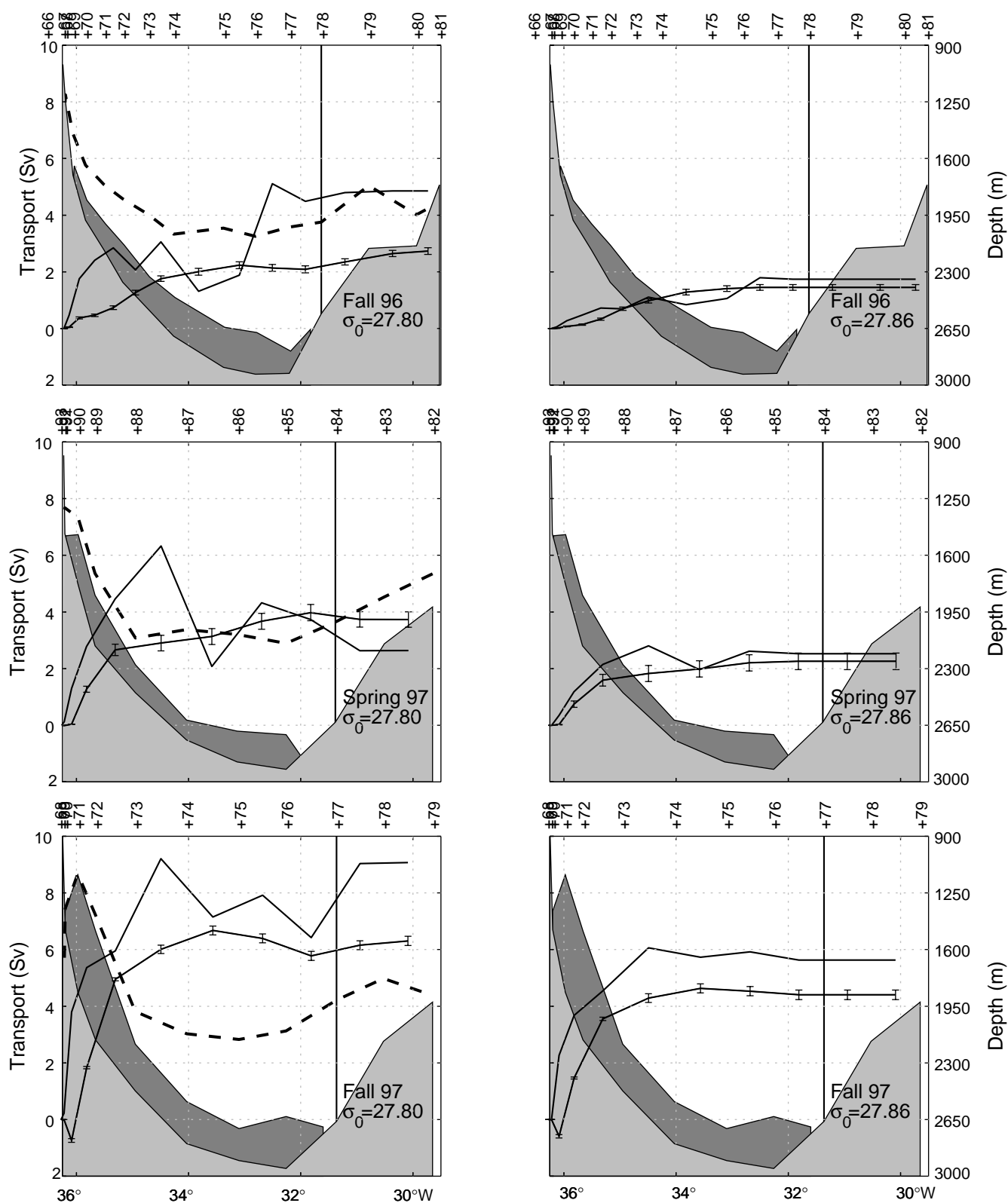


Figure 4. Transports for the Angmagssalik sections accumulated from Greenland (positive is southwestward). Transport below the deepest common level (DCL) is estimated with two methods, using a fixed speed (the DCL speed) or extrapolation of the deep shear from above the DCL. Geostrophic transports plotted are the average of the two methods, and the short vertical bars give the range of the two forms of estimates. ADCP-referenced transports use the average of the underway ADCP velocity normal to the section as a reference speed, and for this curve the range reflecting the two DCL methods is not included in the plot. Bathymetry is shaded light grey. Dark grey shading represents potential temperatures $< 2.4^{\circ}\text{C}$. The dashed line is the $\sigma_0 = 27.80$ contour. Right (left) panels are transports $\sigma_0 = 27.80$ (27.86). The vertical line corresponds to the first offshore stations without potential temperatures less than 2.5°C , and this is used as an estimate of the offshore edge of the DNBC.

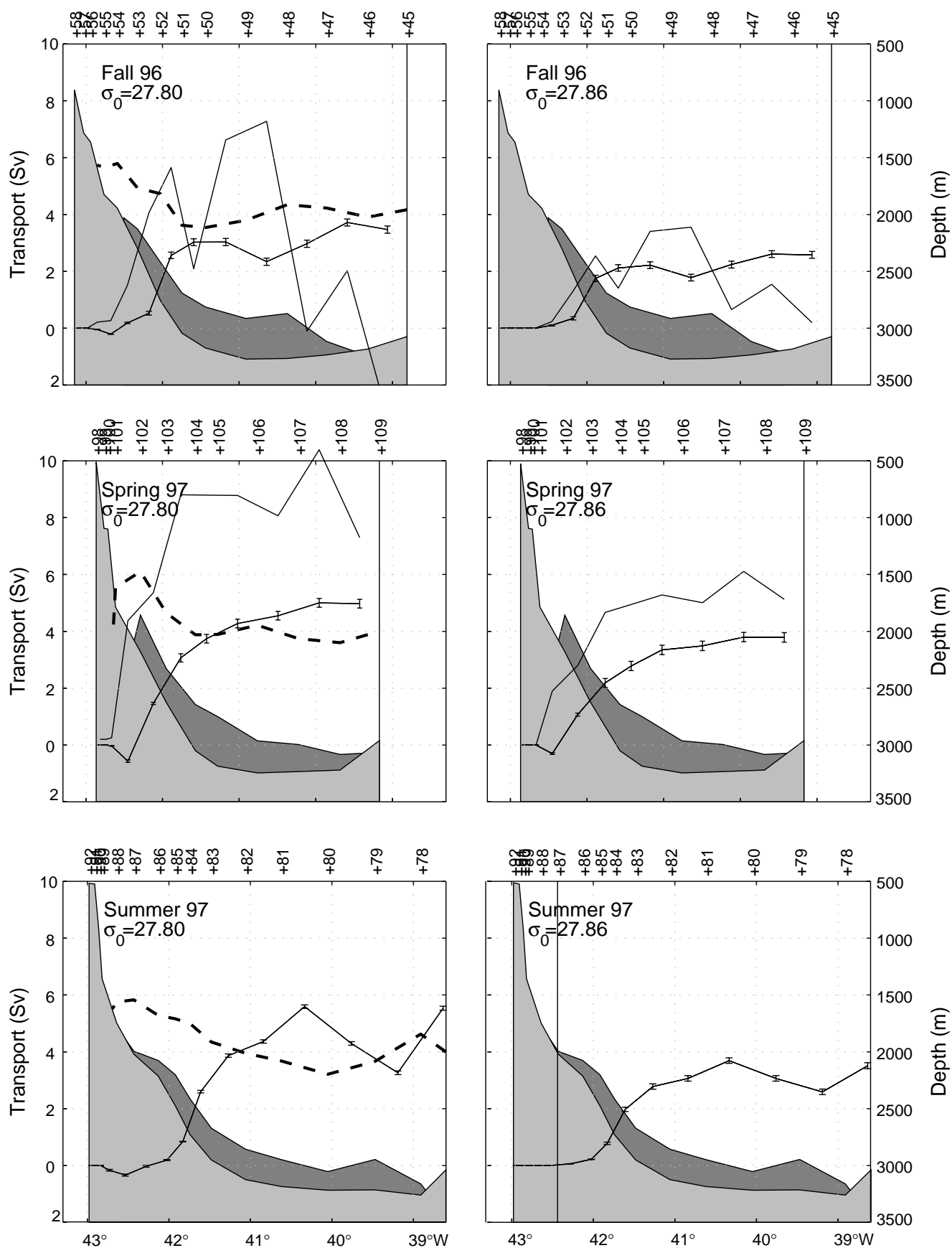


Figure 5. Same as Fig. 4 but for the Cape Farewell sections.

1990–1996 data. In the second realisation there is a transport increase to about 5 Sv, and in the third realisation maximum transport approach 6 Sv. Overall these baroclinic estimates are suggestive of a trend of increasing transport at this site in parallel with that at Angmagssalik, but offshore reversals of flow in the third realisation at Cape Farewell cloud the issue (there is an eddy of some sort at station 79, see also Fig. 2b). ADCP data is not yet available for this third realisation. The two ADCP-referenced estimates available now suggest that the DSOW transport was greatly enhanced in the second realisation compared to the first at Cape Farewell, but we will await the ADCP data for the third realisation to reassure us on the reality of simultaneous transport growth at both locations.

Returning to the question of forcing, the last two winters are notable for the abrupt shift of the NAO index from its very high values in the earlier 1990's. In winter 1995–96, the NAO index (Hurrell, personal communication) dropped from the second highest recorded value +3.94 (in 132 years, the highest was 1989, +5.07), to the second lowest, -3.88. The index recovered in winter 1996–97 only to a slightly positive value of +0.41. Thus our observations of an apparently intensifying and freshening flow of DSOW at Angmagssalik, and related signals at Cape Farewell, occurred one-to-two years after a precipitous drop of the NAO index. The very low-index winter of 1995–96 certainly would have strongly enhanced buoyancy forcing of water-mass transformation compared to the preceding several years of very high NAO index. This again suggests but does not prove a causal link between the atmospheric conditions and the intensity of DSOW transport. We await with curiosity additional measurements to be made by the international community along the coast of Greenland in 1998 as well as wondering what the current winter will yield for a NAO index.

The Overflow system east of Iceland may also have changes in this period. Our three Angmagssalik sections (Fig. 2a) are the western ends of sections reaching to the eastern boundary (Rockall Trough). In mid-basin we obtained three crossings of the ISOW near 60°N where the DNBC carries the ISOW south-west along the eastern flank of the Reykjanes Ridge towards the Charlie Gibbs Fracture Zone. In the third of these crossings, Fall 1997, the coldest ISOW exhibited a cold bottom layer near 2.06°C, about

0.2°C colder than in the earlier two realisations and colder than regional average historical data. In the Iceland Basin the main thermocline is deeper than in the Irminger Basin, so we use a 1500 db reference level to make preliminary baroclinic transport estimates of 4.1, 3.4, and 5.0 Sv for the water 27.80 in fall 1996, spring 1997, and fall 1997, respectively, indicating here too an enhanced dense water transport by late 1997. Thus it is possible that the entire DNBC system accelerated in 1997, and that this may be a reflection of NAO-induced change in the forcing of both DSOW and ISOW.

Acknowledgements

The authors thank Lynne Talley and Eric Firing for the use of the spring 1997 ACCE data.

References

- Bacon, S., 1997a: Decadal variability of the North Atlantic Overflows. *Int. WOCE News.*, 26, 29–30.
- Bacon, S., 1997b: Decadal variability in the Outflow from the Nordic Seas to the Deep North Atlantic. *Nature*, subjudice.
- Brewer, P. G., W. S. Broecker, W. J. Jenkins, P. B. Rhines, C. G. Rooth, J. H. Swift, T. Takahashi, and R. T. Williams, 1983: A climatic freshening of the deep Atlantic north of 50°N over the past 20 years. *Science*, 222, 1237–1239.
- Dickson, R. R., and J. Brown, 1994: The production of North Atlantic Deep Water: Sources, rates and pathways. *J. Geophys. Res.*, 99, 12319–12341.
- Dickson, R. R., J. R. N. Lazier, J. Meincke, P. Rhines, and J. Swift, 1996: Long-term coordinated changes in the convective activity of the North Atlantic. *Prog. Oceanogr.*, 38, 241–295.
- Hurrell, J. W., 1995: Decadal Trends in the North Atlantic Oscillation Regional Temperatures and Precipitation. *Science*, 269, 676–679.
- Lazier, J. R. N., 1988: Temperature and salinity changes in the deep Labrador Sea, 1962–1986. *Deep-Sea Res.*, 35, 1247–1253.
- Mauritzen, C., 1996a: Production of Dense Overflow Waters Feeding the North Atlantic Across the Greenland-Scotland Ridge. Part 1: Evidence for a revised Circulation Scheme. *Deep-Sea Res.*, 43, 769–806.
- Mauritzen, C., 1996b: Production of Dense Overflow Waters Feeding the North Atlantic Across the Greenland-Scotland Ridge. Part 2: An Inverse Model. *Deep-Sea Res.*, 43, 807–835.
- Swift, J. H., 1984: A recent T-S shift in the deep water of the northern North Atlantic. In: *Climate processes and climate sensitivity*, J. E. Hansen and T. Takahashi, editors. *Geophysical Monographs*, 29, Maurice Ewing Volume 5, American Geophysical Union, Washington DC, 39–47.

Toward an Estimate of the Global Circulation from WOCE Data and a General Circulation Model

Detlef Stammer, Massachusetts Institute of Technology, USA. detlef@lagoon.mit.edu



A primary objective of WOCE is to obtain an understanding of the absolute time-varying large-scale circulation of the world ocean, and its impact on climate. To meet this goal, all available data need to be evaluated jointly and in a way consistent with data uncertainties and with our best knowledge about dynamics as it is embodied in modern

Ocean General Circulation Models (OGCMs). All important aspects of the circulation and its transport properties can be studied subsequently from the estimated ocean state and its uncertainty. Here we illustrate preliminary results of such a global estimation system for the time-evolving, absolute circulation of the ocean and describe work in progress.

The state estimation system is based on a general circulation model and its adjoint, which have been developed recently by a group at the Massachusetts Institute of Technology (see Marotzke et al., 1998). The forward component is the general circulation model developed by John Marshall and his group and is described in Marshall et al. (1997a,b). The adjoint (backward) component is obtained from the forward component by using the Tangentlinear and Adjoint Model Compiler (TAMC) which was written by Ralf Giering (Giering and Kaminsky, 1997). This system is extremely flexible since it allows one to easily regenerate the adjoint code whenever a change in the forward code is necessary.

First results

Our present focus is on the evolving global circulation as it emerges as a base-line solution from altimetric measurements alone. Precise and accurate TOPEX/POSEIDON (T/P) sea surface height observations are now available on a routine basis for 5+ years covering the period September 1992 through the present. Combined with a general circulation model, they carry unprecedented information about the large-scale circulation (see Wunsch and Stammer, 1998 for a recent review of satellite altimetry). Information from WOCE in situ data such as XBTs, floats and the WOCE hydrography is being used first as independent information to test the results. These data will subsequently be included in the estimation process.

In a preliminary attempt, configured to test a real ocean state estimation system, the model was run with 2° horizontal resolution and 20 levels in the vertical. The model was then constrained by absolute T/P sea surface height data from the year period covering 1993, relative to the most recent geoid estimate (Lamoiné et al., 1997) (the forward model was constrained separately in the mean and time-dependent components of surface pressure, thus separating the geoid error from the distinctly different error in the time-evolving components) as well as NCEP surface forcing fields (wind stress, heat and fresh water fluxes) and the mean Levitus et al. (1994) hydrography. To bring the model into consistency with the observations, the initial potential temperature (θ) and salinity (S) fields are modified, as well as the surface forcing fields. Changes in those fields (often referred to as “control” terms) are determined as a best-fit in a least-squares sense of the model state to the observations and their uncertainties over the full data period. In that configuration, there are 1.5×10^6 elements in the control vector.

The MIT Ocean State Estimation Group includes Carl Wunsch, Detlef Stammer, Jochem Marotzke, Ralf Giering, Kate Zhang, Bruno Ferron, Nadia Ayoub as well as John Marshall, Chris Hill and Alistair Adcroft on the model development side.

To indicate the potential of the system, a few results from the preliminary run are shown here (all results obtained after the cost function was reduced close to the desired minimum value) which illustrate a time-evolving model state which differs from both the forward model and the data. A full presentation of the output can be seen at the web-site <http://puddle.mit.edu/~detlef/global.html>.

Fig. 1 (page 24) shows the optimised monthly mean fields of the surface elevation together with the velocity at 120 m depth for October 1993. Apart from the missing eddy variability, major elements of the general circulation are present in both fields. In contrast to the pure T/P observations, various spurious elements in the data due to errors in the geoid are absent in the combined estimate. This is especially clear in the tropical Pacific and the North Atlantic where previously known inconsistencies in the geoid led to unacceptable features in the inferred ocean circulation (Stammer and Wunsch, 1994).

Changes in the estimated model state relative to the unconstrained model are illustrated in Fig. 2 (page 24) from variations in the velocity and temperature fields taken from the same month at 120 m and 610 m depth, respectively. Various spatially coherent temperature changes on eddy-to-basin scales can be seen. Maximum amplitudes are associated with western boundary currents in the northern hemisphere and along the Antarctic Circumpolar Current.

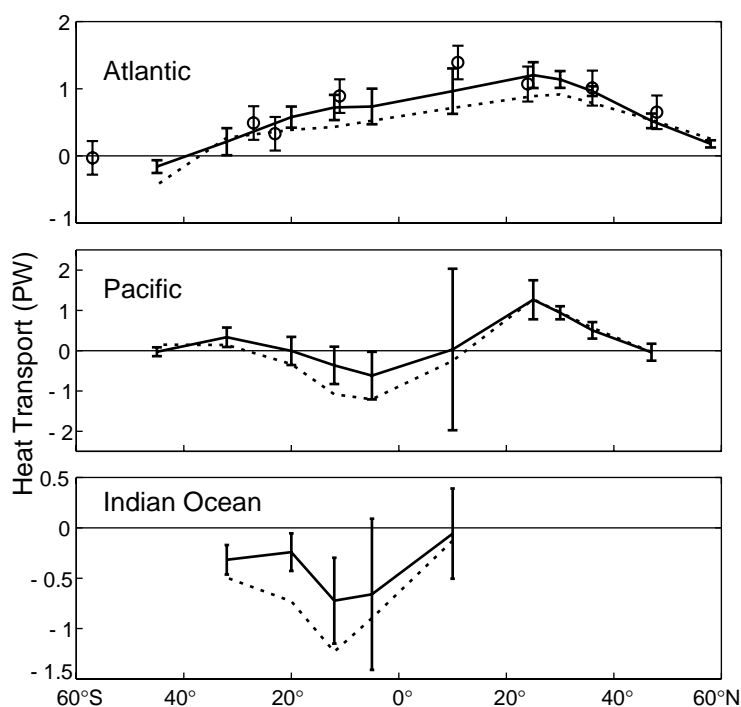


Figure 3. Time-mean meridional heat transport (in 10^{15} W) estimated from the last 6 months of the constrained (solid lines) and unconstrained model (dashed lines) for the Atlantic, Pacific, and Indian Oceans, respectively. Solid bars represent the rms variability of the transports estimated over individual 10-day periods. Also shown as open circle and error bars are the heat flux estimates and their uncertainties obtained by Macdonald and Wunsch (1996) in the Atlantic from their box-inversion of the global ocean.

As an example, the path of the North Atlantic Current is characterised by increased temperatures relative to the unconstrained solution. Note also the wave-like pattern in the velocity corrections of the tropical Pacific and Indian Ocean and the enhanced boundary currents at many locations of the world ocean. T/P surface observations demand changes in the model state over the entire water column.

The impact of the T/P data on estimates of oceanic transports are illustrated in Fig. 3 in terms of meridional heat transports from the Atlantic, the Pacific and the Indian Oceans. Estimates are shown of the annual-average transports from the unconstrained run (dashed lines) and the constrained estimate (solid lines). In the North Atlantic, the T/P data inquire an increase in the model-alone estimate of northward heat transport from about 0.8 PW to almost 1.2 PW at 25°N. Note that the estimates from the constrained state are consistent with previous results from Macdonald and Wunsch (1996) and their errors estimates which are shown as open circles and error bars. An exception can be found at 10°N, where the model estimate is significantly lower than the former result. The basis for this "adjustment" is a strengthening of the vertical overturning flow field with an up to 1 cm/s stronger and about 1°C warmer poleward flow in the Gulf Stream, and an enhanced and colder return flow at depth.

Work in progress

Computations now underway are directed at greatly extending and improving the preliminary computation. Improvements will include an increased model resolution to 1°, an extended estimation period to 6 years (1992 through 1997), as well as more accurate representations of straits and sills in the topography. Equally important, a complete mixed layer model (Large et al., 1994) and an eddy parameterisation (Gent and McWilliams, 1990) have been incorporated into the adjoint model. Moreover, a full (non-diagonal) geoid error covariance matrix is being used as well as other improvements in the remaining weights.

Data now include the absolute and time-varying T/P data from October 1992 through December 1997, SSH anomalies from the ERS-1 and ERS-2 satellites, monthly mean SST data (Reynolds and Smith, 1994), time-varying NCEP Re-Analysis fluxes of momentum, heat and freshwater, and NSCAT estimates of wind stress errors are being employed. Monthly means of the model state are required to remain within assigned bounds of the monthly mean Levitus et al. (1994) climatology. The control vector now contains 8 million elements.

Special attention is necessary for the hydrographic data weights for future WOCE WHP applications, which in principle requires the knowledge of the 3 dimensional frequency-wavenumber spectrum of the ocean temperature and salinity field. Ultimately one needs error covariance estimates for all components involved, including the model

itself and the atmospheric forcing fields provided by meteorological centres.

As a complementary effort, regional experiments are being run with enhanced resolution. These experiments are nested into the global estimates and use the T,S and horizontal flow field at the open boundaries as part of the control vector. They are being run in the Indian Ocean (PI: J. Marotzke) and in the Atlantic Ocean north of 30°S as part of the regional WOCE AIMS efforts. Another effort being addressed at MIT is the generation of uncertainty estimates of results and their sensitivity to specific data (R. Giering and C. Wunsch).

The set of computations now underway is still regarded as preliminary. The model resolution will eventually be greatly increased and as much as possible of the entire WOCE data set will be used. The combination of the OGCM with data, each appropriately weighted by its uncertainty estimates, should provide a useful basic description of the ocean circulation and its variability. Among many possible applications, one expects the production of much better estimates of property flux divergences, and the study of oceanic biogeochemical cycles which are dependent upon the circulation.

References

- Gent, P. R., and J. C. McWilliams, 1990: Isopycnal mixing in ocean models. *J. Phys. Oceanogr.*, 20, 150–155.
- Giering, R., and T. Kaminsky, 1997: Recipes for adjoint code construction ACM. *Trans. Math. Software*. In press.
- Large, W. G., J. C. McWilliams, and S. C. Doney, 1994: Oceanic vertical mixing: a review and a model with non-local boundary layer parameterization. *Rev. Geophys.*, 32, 363–403.
- Lamoine, F., and 17 others, 1997: The development of the NASA GSFC and NIMA Joint Geopotential Model. In *Gravity, Geoid and Marine Geodesy*, International Association of Geodesy Symposia, 117, ed. Segawa et al. Springer-Verlag., Berlin Heidelberg.
- Levitus, S., R. Burgett, and T. Boyer, 1994: World Ocean Atlas 1994, Vol. 3, Salinity, and Vol. 4, Temperature, NOAA Atlas NESDIS 3 & 4, US Dept. of Comm., Washington, DC.
- Macdonald, A., and C. Wunsch, 1996: The global ocean circulation and heat flux. *Nature*, 382, 436–439.
- Marotzke, J., Q. K. Zhang, R. Giering, D. Stammer, C. N. Hill, and T. Lee, 1998: The linearization and adjoint of the MIT general circulation model. In preparation.
- Marshall, J., A. Adcroft, C. Hill, L. Perelman, and C. Heisey, 1997a: A finite-volume, incompressible navier-stokes model for studies of the ocean on parallel computers. *J. Geophys. Res.*, 5753–5766.
- Marshall, J., C. Hill, L. Perelman, and A. Adcroft, 1997b: Hydrostatic, quasi-hydrostatic and non-hydrostatic ocean modeling. *J. Geophys. Res.*, 5733–5752.
- Reynolds, R. W., and T. M. Smith, 1994: Improved global sea surface temperature analyses using optimum interpolation. *J. Climate*, 7, 929–948.
- Stammer, D., and C. Wunsch, 1994: Preliminary assessment of the accuracy and precision of TOPEX/POSEIDON altimeter data with respect to the large scale ocean circulation. *J. Geophys. Res.*, 99, 24584–24604.
- Wunsch, C., and D. Stammer, 1998: Satellite Altimetry, the Marine Geoid and the Oceanic General Circulation, *Annual Reviews of Earth and Planetary Sciences*. In press.

Data Assimilation for Australian Climate Variability Studies



Peter McIntosh and Andreas Schiller, CSIRO Division of Marine Research, Hobart, Australia. Peter.McIntosh@marine.csiro.au

This article describes the development of and preliminary results from a data assimilation system intended for eventual operational use within Australia. This is a joint project between CSIRO and the Bureau of Meteorology Research Centre, and is sponsored in part by the Land and Water Resources Research and Development Corporation. From an oceanographic viewpoint, the aim is to be able to predict sea-surface temperatures (SSTs) up to 12 months ahead in the regions that affect Australia's climate. Accurate SST predictions are a prerequisite for obtaining useful predictions of rainfall and other variables for the Australian agricultural community.

The need for operational predictions of climate variation requires a pragmatic approach to the intricacies of data assimilation. There are definite restrictions on the development time, and on the computer resources needed to run the system. Therefore we use a relatively simple assimilation scheme based on statistical interpolation. It is not clear that the considerable extra development and computer time required by more complicated methods will lead to a proportional increase in forecast accuracy.

Assimilation strategy

In brief, the assimilation strategy involves replacing the model temperature field every 10 days with a new field obtained by statistical interpolation of temperature data. The interpolation is performed at each depth independently. The model field is used as the first guess, so that no change occurs away from observations. A salinity change corresponding to the temperature change is calculated by interpolation along the local observed climatological T/S relationship. The temperature data is assimilated as an anomaly to reduce the impact of model bias. This means that the data is adjusted by the difference between the model and data seasonal climatologies before interpolation.

The data used consists of expendable bathythermograph (XBT) profiles from the Indian and Pacific Oceans. The statistical interpolation technique includes a data quality control phase. We are currently developing a technique for converting satellite altimeter and satellite SST data into "synthetic" XBT data to increase data coverage, particularly in the relatively poorly-sampled Indian Ocean.

Ocean model

We use a global ocean model based on the GFDL MOM2 code, with enhancements designed to represent tropical physics accurately (Schiller et al., 1998). The model is freely available as the Enhanced-Tropical ("ET") grid version of the Australian Community Ocean Model (ACOM) project (<http://www.marine.csiro.au/acom>). In the experiments described here, the model is run using monthly surface fluxes for 1990, but otherwise as described by Schiller et al. (1998).

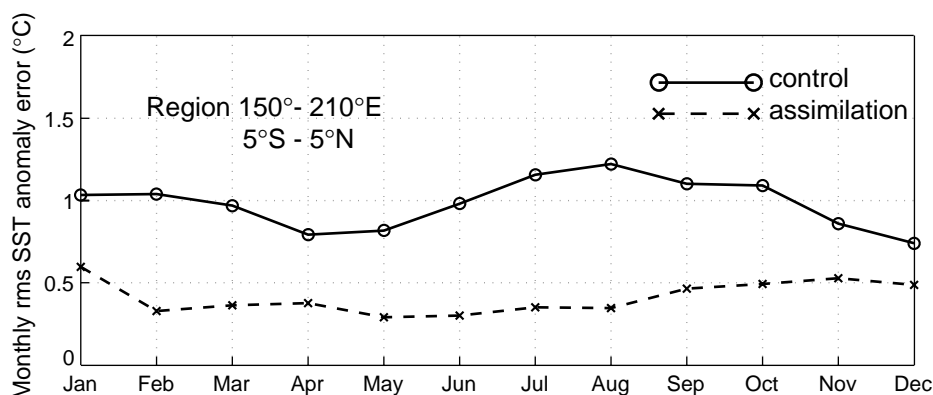


Figure 1. Monthly rms SST anomaly error in the western equatorial Pacific for control and assimilation runs. Assimilation ends in June (1990).

The model has a constant two degree zonal resolution, and a meridional grid concentrated near the equator, where the resolution is half a degree. There are 25 vertical levels which are concentrated in the thermocline. Wind forcing is by a combination of Florida State University (Legler et al., 1989; Stricherz et al., 1992) and Hellerman and Rosenstein (1983) winds, turbulent heat flux formulation is by Seager and Blumenthal (1994), short-wave radiation is from Li (1995), and surface salinity is restored to climatology. The model has a one-dimensional mixed-layer model (Chen et al., 1994), with vertical mixing below this based on observed estimates of the gradient Richardson number (Peters et al., 1988).

Statistical interpolation

The statistical interpolation is a two-dimensional univariate objective analysis in the horizontal plane (Smith, 1995). The first guess field is the model temperature field. The space and time-scales for the temperature covariance function are chosen based on the results of Meyers et al. (1991). The analysis system performs analyses in

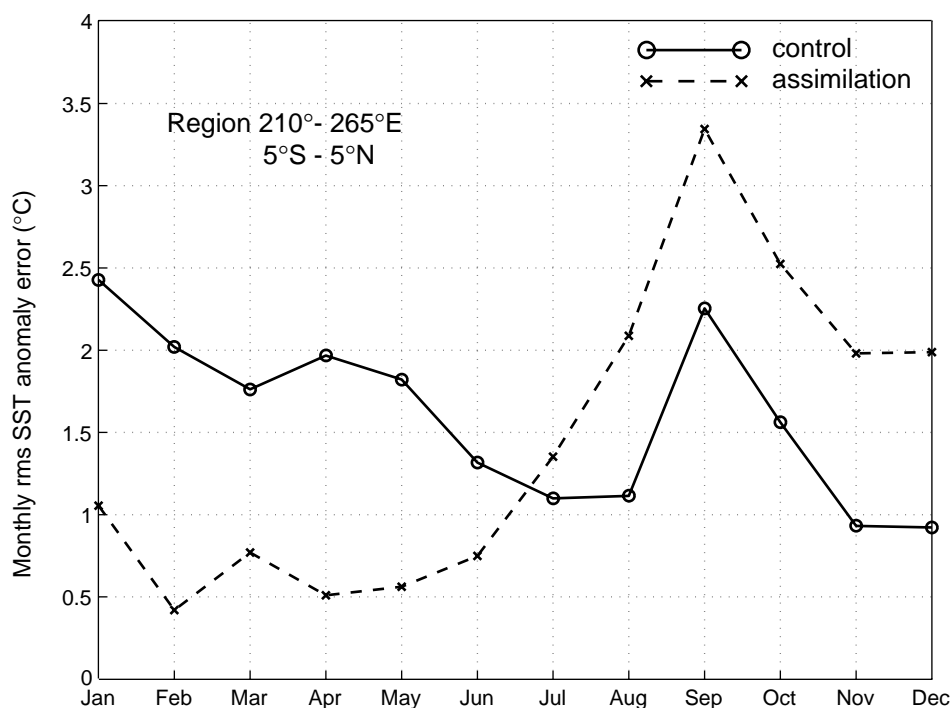


Figure 2. Same as Figure 1 but for the eastern equatorial Pacific (NINO-3 region).

overlapping subregions to avoid inverting large covariance matrices. The analyses are then joined smoothly. The space and time scales of the covariance function vary in space to account for differing scales in dynamically-different regions. However, we had to force the covariance function to have constant scales within each subregion to prevent improper covariance matrices. This is an area of ongoing research. One important disadvantage is our inability to modify covariance length-scales near narrow strips of land (such as in the Indonesian region) to prevent data influencing the analysis through land barriers.

The Smith (1995) analysis package contains objective data quality control strategies such as buddy-checking and cross-validation. It is also able to combine adjacent observations to reduce the computing time. We find a typical increase of computer time of about 10% with around 1200 temperature profiles assimilated every 10 days.

Preliminary results

The experiment described here involves assimilating data for the first 6 months of 1990, and then integrating for a further 6 months to see how long information persists in the model. We concentrate on results for the Pacific Ocean at this stage because there is so little data in the Indian Ocean. The observations come from the WOCE Data Assembly Centre (DAC) quality-controlled data set, and are predominantly XBT data. The Reynolds SST verification data depends predominantly on satellite observations (Reynolds, 1988; Reynolds and Marsico, 1993) and so can be considered an essentially independent data set. We compare anomalies from seasonal climatology to remove the bias in our model.

Fig. 1 shows the root mean-square SST anomaly error for a region in the equatorial western Pacific for both the control and assimilation runs. The assimilation run only assimilates data up to the end of June, but substantially increased accuracy is evident in the assimilation run until the end of the year.

Fig. 2 shows the same information for the NINO-3 region in the eastern Pacific. Although data assimilation improves the SST, once data assimilation is turned off the SST errors quickly become larger than the control run.

We have yet to analyse these results in any detail, but it seems likely that the assimilation is interacting in some way with systematic errors in the ocean model in the eastern Pacific. We are hopeful that the results of

this and other assimilation experiments will give us new insights into why our model (like virtually all other similar models) has the greatest difficulty in simulating the eastern equatorial Pacific.

Issues for the future

There are many questions remaining to be answered. These include:

- (i) Is the technique of assimilating anomalies a useful way to reduce the effect of model bias?
- (ii) What are the appropriate length and time scales for the covariance function?
- (iii) Is there some way of specifying the space (and time) variation of these scales without incurring improper covariance matrices?
- (iv) What is the best way to prevent the influence of data extending over narrow coastal strips?
- (v) What is the best assimilation interval?
- (vi) How important is the salinity correction?
- (vii) How important is "synthetic" XBT data?

References

- Chen, D. L. M. Rothstein, and A. J. Busalacchi, 1994. A hybrid vertical mixing scheme and its application to tropical ocean models. *J. Phys. Oceanogr.*, 24, 2156–2179.
- Hellerman, S., and M. Rosenstein, 1983: Normal monthly wind stress over the world ocean with error estimates. *J. Phys. Oceanogr.*, 13, 1093–1104.
- Legler, D. M., I. M. Navon, and J. J. O'Brien, 1989: Objective analysis of pseudostress over the Indian Ocean using a direct-minimization approach. *Mon. Weath. Rev.*, 117, 709–720.
- Li, Z., 1995: Intercomparison between two satellite-based products of net surface shortwave radiation. *J. Geophys. Res.*, 100,

3221–3232.

- Meyers, G., H. Phillips, N. R. Smith, and J. Sprintall, 1991: Space and time scales for optimal interpolation of temperature - Tropical Pacific Ocean. *Progr. Oceanogr.*, 28, 189–218.
- Peters, H., M. C. Gregg, and J. M. Toole, 1988. On the parametrization of equatorial turbulence. *J. Geophys. Res.*, 93, 1199–1218.
- Reynolds, R. W., 1988: A real-time global sea surface temperature analysis. *J. Climate*, 1, 75–86.
- Reynolds, R. W., and D. C. Marsico, 1993: An improved real-time global sea surface temperature analysis. *J. Climate*, 6, 114–119.

- Schiller, A., J. S. Godfrey, P. C. McIntosh, G. Meyers, and S. E. Wijffels, 1998: Seasonal near-surface dynamics and thermodynamics of the Indian Ocean and Indonesian throughflow in a global ocean general circulation model. *J. Phys. Oceanogr.* (in press).
- Seager, R., and M. B. Blumenthal, 1994: Modeling tropical Pacific sea surface temperature with satellite-derived solar radiative forcing. *J. Climate*, 7, 1943–1957.
- Smith, N. R., 1995: The BMRC ocean thermal analysis system. *Aust. Met. Mag.*, 44, 93–110.
- Stricherz, J. N., J. J. O'Brien, and D. M. Legler, 1992: Atlas of Florida State University tropical Pacific winds for TOGA 1966–1985. Florida State University, 256pp.

Assimilation of TOPEX Data into the OCCAM Model



A. Fox, K. Haines, B. de Cuevas, and D. Webb, Department of Meteorology, University of Edinburgh, The King's Buildings, Edinburgh EH9 3JZ, UK. A.D.Fox@ed.ac.uk

An earlier article in the UK WOCE newsletter *Sigma*, Fox and Haines (1996), reported on twin experiment results assimilating sea level data into the $\frac{1}{4}$ degree, 36 level OCCAM model (Gwilliam et al., 1997). In this article we report on progress since that time assimilating TOPEX maps for 1993 into OCCAM. Many new problems arise when assimilating real data into a model. The results we report here are preliminary but they point to two encouraging possibilities. The first is that some errors in the model mean circulation, specifically the Gulf Stream and Kuroshio separation paths, can be 'corrected' by assimilating appropriate mean sea level data. The second result points to the ability of the model to interpolate data effectively in time. This is highlighted by an ability to predict sea level anomalies more accurately than by assuming persistence.

Correcting mean sea levels

After 8 years of spin-up from Levitus, forcing with monthly mean winds, the OCCAM model was forced with 1992–1993, 6-hourly winds from ECMWF. Surface temperature and salinity are still relaxed to climatological monthly mean values on a 30 day time-scale. Figs. 1a,b show the mean sea level around the Gulf Stream and Kuroshio averaged over 1993 from the model. The common anti-cyclonic overshoot and standing Rossby wave can be seen in both regions. We attempted to reconstruct a more realistic mean sea level for both these regions using hydrographic data. The results are shown in Fig. 1c,d. The changes from 1a,b to 1c,d come from calculating the difference in dynamic height between the model and Levitus (Levitus et al., 1994; Levitus and Boyer, 1994) hydrography, in the case of the Kuroshio, and an isopycnally mapped hydrography based on the Lozier et al. (1995) technique, for the Gulf Stream. The modified mean sea levels match smoothly to the model derived mean for 1993 in all other regions.

The 1993 year model run was then repeated with data assimilation. Every 10 days during this assimilation run the model sea level was corrected towards a sea level consisting of the annual mean (with corrections according to Figs. 1c,d)

combined with a TOPEX anomaly map provided by AVISO. Fields other than sea level were updated by the Cooper and Haines (1996) vertical displacement method with a geostrophic update to velocities away from the equator. To demonstrate the effectiveness of the mean sea level correction, Figs. 1e,f shows the sea surface temperature from this run on 24 March 1993. In both regions the frontal position has separated from the coast at a lower latitude and sea surface temperatures reflect this. Correcting the path of these major current system may have important consequences if ocean models are to be used for climatic studies. There will, for example, be large changes in surface heat flux associated with the altered frontal paths shown in Fig. 1, although we have not yet diagnosed these from OCCAM.

Sea level tendency and error analysis

There is little point in using a model for data assimilation if that model is unable to interpolate data correctly in time over some period. To test this ability Fig. 2a shows the sea level change over the tropical Pacific during the 20 days from 30 January 1993 to 19 February 1993. This is simply the difference between the TOPEX maps from AVISO. Twenty days is the shortest period for which the maps contain only independent data. Fig. 2b shows a model prediction of the same quantity based on assimilating data up to 30 January and thereafter allowing the model to run free. If we compare Figs. 2a,b we find many features in common, correlating the two fields yields a correlation coefficient of 0.78 between the model and observational tendencies over the region illustrated. Similar figures could be shown from any time during the assimilation run and from most regions of the globe. It is possible to define more quantitative comparison methods. The global RMS difference between the model predicted height anomaly and the observed TOPEX map on 19 February was 7.0 cm while the difference between the 30 January and 19 February TOPEX maps was 8.1 cm. The anomaly correlations for the above comparisons give 0.54 for the model prediction

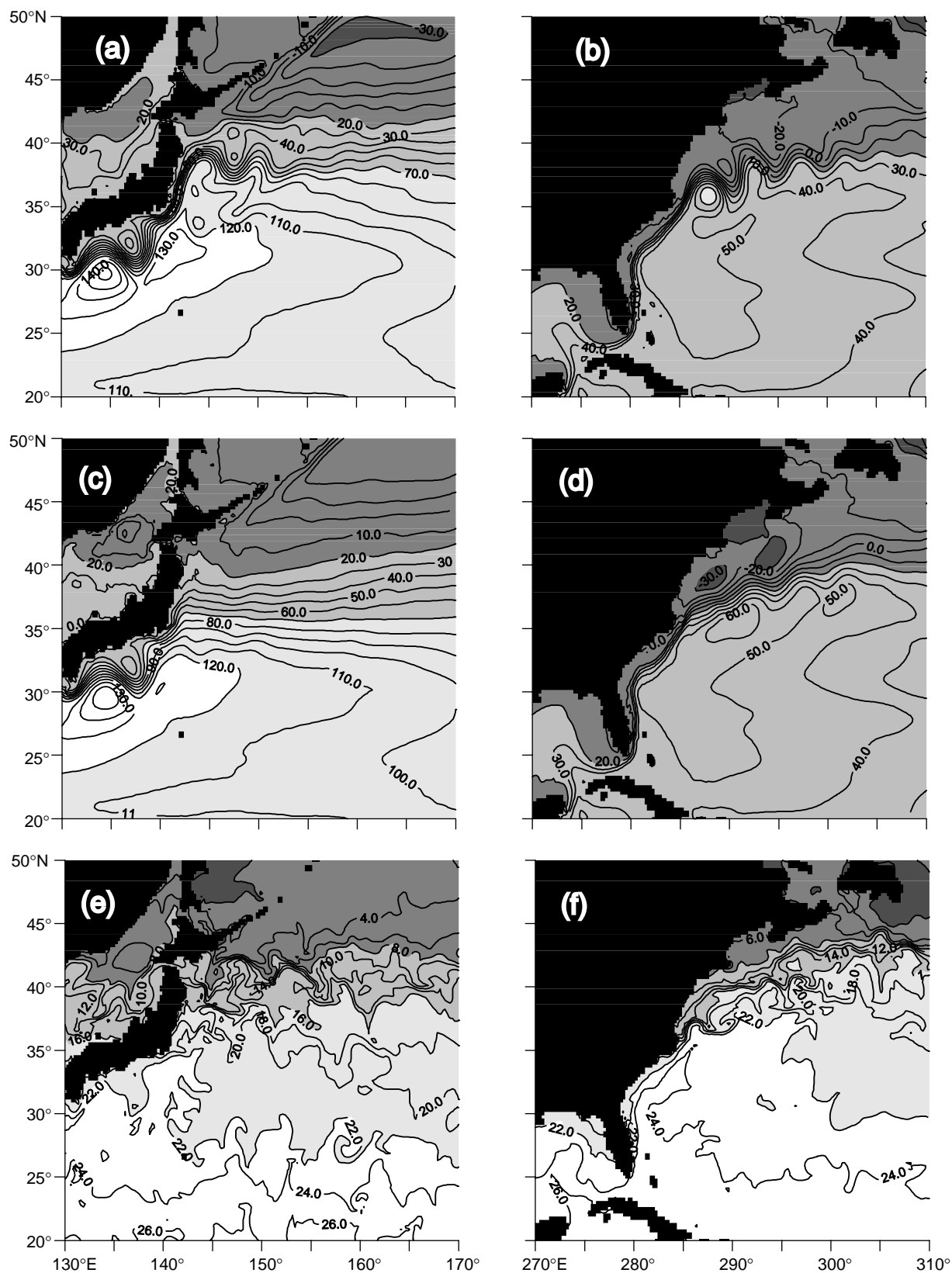


Figure 1. (a,b) Model mean sea surface height, 1993. (c,d) Mean SSH after modifications according to climatology. (e,f) Sea Surface temperature ($^{\circ}\text{C}$) from the model with assimilation, 24 March 1993.

and 0.49 for the persistence field. In the tropical Pacific region shown in Fig. 2 the improvement over persistence is greater, with RMS differences of 4.3 cm and 6.0 cm for the model prediction and persistence respectively. The corresponding correlation coefficients are 0.67 for the model and 0.43 for persistence. Thus the model forecast can beat persistence over 20 day periods.

The updating of model sea level is carried out as follows;

$$\eta_a = \eta_f + \frac{\sigma_f^2}{\sigma_f^2 + \sigma_T^2} (\eta_T - \eta_f),$$

where σ_T^2 is the current TOPEX error variance map, σ_f^2 is the model forecast error, η_T is the current TOPEX sea level anomaly, η_f is the model forecast sea level anomaly and η_a is the analysis sea level being calculated. Other fields are calculated from this update using the Cooper and Haines (1996) method. To help test for convergence of model forecast to the true sea surface height field the model-data misfit M at analysis time is calculated as:

$$M = \frac{\sum \frac{A}{e_T} (\eta_T - \eta_{f,a})^2}{\sum \frac{A}{e_T}}$$

where $\eta_{f,a}$ may be the forecast or analysed model sea level, A is the grid-square area and e_T is the TOPEX anomaly error provided with the height anomaly maps by AVISO expressed as a fraction of the variance, the sum represents an area average. Fig. 3a shows the evolution of M through the 1993 run for the global ocean and for the Gulf Stream region.

In the first few time-steps M is greatly reduced but thereafter the growth in M every 10 days is approximately equal to the reduction in M when new data is assimilated. The reduction in the highly energetic Gulf Stream region is smaller than the global average with M also more variable over time. The current σ_f is being set equal to the global mean of σ_T which is a very crude approximation and does not allow for a reduction in σ_f over time which would be necessary for convergence. An important future step will be to improve this error treatment. We hope to achieve this without resorting to a Kalman filter which would be prohibitively expensive for a model of this complexity.

Finally Fig. 3b shows the kinetic energy during the assimilation run. The assimilation is seen to increase the kinetic energy over the first 1 or 2 months but this levels off at about 80% higher than the wind forced simulation.

Much of this difference seems to involve sea level variability in the quiet regions of the ocean such as the south Pacific where the OCCAM model has too little variability. In the active regions such as the Gulf Stream, the Agulhas and the ACC the OCCAM model already simulates a realistic level of sea level variability. The reason for the discrepancy in the other regions is not known at the present time.

Conclusions and further development

Twin experiments (to be reported in Fox and Haines, 1998) demonstrate the effectiveness of the Cooper and Haines method for vertical projection of altimeter data into the model interior. With the results presented here we have applied the method to assimilation of real altimeter data into the OCCAM model, the results look promising with the assimilating model proving its ability to beat persistence over 20-day predictions of sea surface height. Together with further analysis of the 1993 TOPEX assimilation run described above, including comparisons with independent datasets, we now intend to concentrate on refining our treatment of errors in the data and model and combining assimilation of altimeter data with other datasets. In particular, the combination of altimeter and sea surface temperature assimilation needs investigation, and we will be implementing a scheme for assimilation of in-situ temperature profiles which is currently under development here at Edinburgh University, Department of Meteorology. Further details of this work can be found on our web-site: <http://www.met.ed.ac.uk/~alberto/ocgr/>

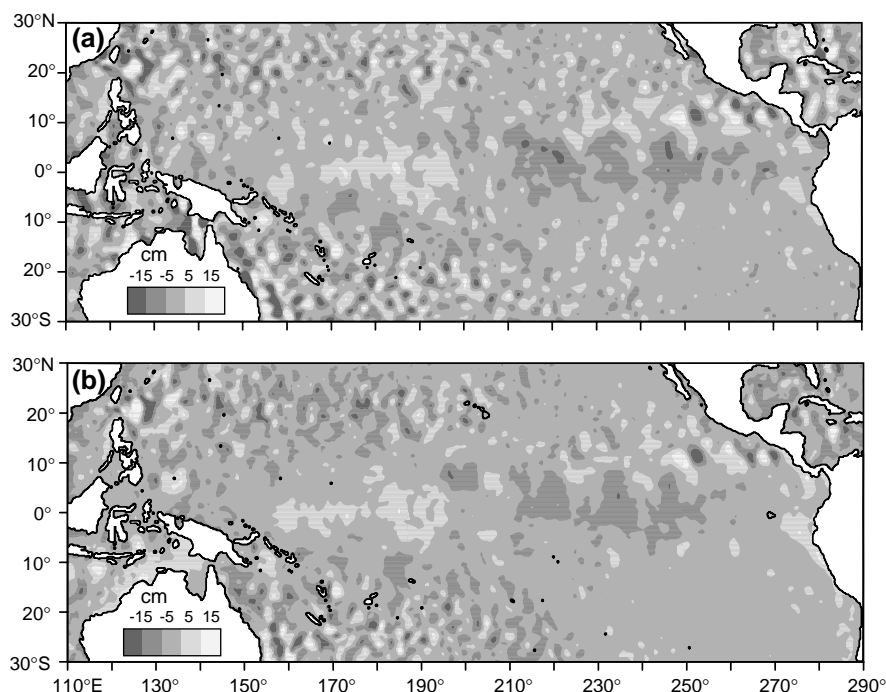


Figure 2. Sea level change (cm) during 20 days from 30 January to 19 February 1993. (a) as measured by TOPEX. (b) as predicted by OCCAM model, with assimilation up to 30 January.

Acknowledgements

The above work has been carried out as part of the EU Environment project AGORA, supported by grant number ENV4-CT95-0113. Support is now being received from NERC, grant no. GST/02/1956.

References

- Cooper, M., and K. Haines, 1996: Altimetric assimilation with water property conservation. *J. Geophys. Res.*, 101, C1, 1059–1077.
- Fox, A. D., and K. Haines, 1996: Altimeter data assimilation in the OCCAM model. *Sigma: The UK WOCE Newsletter*, Issue 21.
- Fox, A. D., and K. Haines, 1998: Altimeter assimilation in the OCCAM global model. In preparation.
- Gwilliam, C. S., A. C. Coward, B. A. de Cuevas, D. J. Webb, E. Rourke, S. R. Thompson, and K. Döös, 1997: The OCCAM Global Ocean Model pp 24–30 in: *Proceedings of the Second UNAM-Cray Supercomputing Conference: Numerical Simulations in the Environmental and Earth Sciences*, Mexico City, 1995, F. Garcia-Garcia et al., Eds., Cambridge University Press, 281pp.
- Levitus, S., R. Burgett, and T. Boyer, 1994: *World Ocean Atlas*, Vol. 3 NESDIS 3, 99pp.
- Levitus, S., and T. Boyer, 1994: *World Ocean Atlas*, Vol. 4 NESDIS 4, 117pp.
- Lozier, M. S., W. B. Owens, and R. G. Curry, 1995: The Climatology of the North Atlantic. *Progr. Oceanogr.*, 36, 1–44.

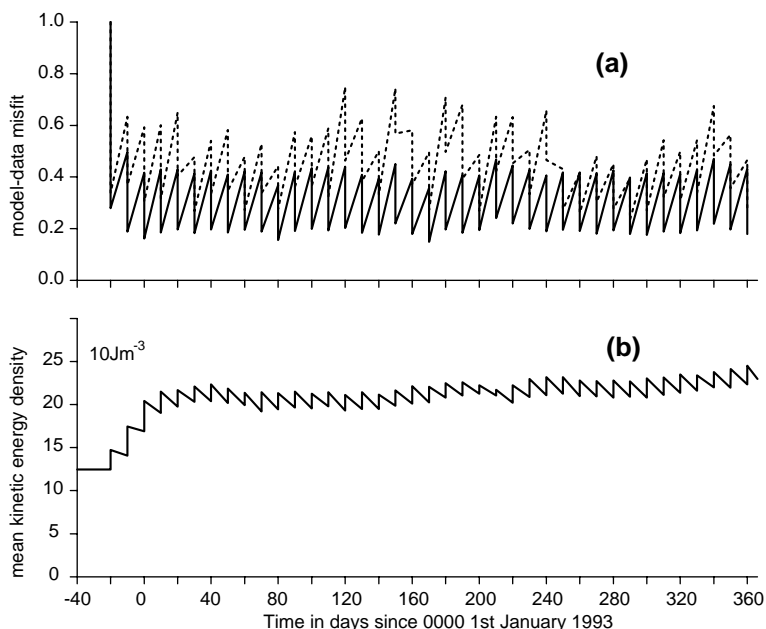


Figure 3. (a) Model-data misfit averaged globally (solid line), and for the Gulf Stream (dashed line). Values are given as fraction of the initial, pre-assimilation values: global 73.1 cm^2 , Gulf Stream 306.1 cm^2 . (b) Evolution of volume average kinetic energy in the assimilating model. Note that assimilation begins at day -20 (11 December 1992).

WOCE Indian Ocean Workshop

As reported in WOCE Notes, Vol. 10, No. 1, the WOCE workshop on the Indian Ocean will be held at the Hampton Inn in New Orleans, 22–25 September 1998. Rather than being an assembly for presenting general research reports, the meeting is intended to try to foster collaborations on some of the larger problems of Indian Ocean oceanography – problems that, because of their geographical scope, or variety and abundance of pertinent new data, or large number of interested investigators, might be difficult or intimidating for individuals to undertake separately. Some such topics are: Meridional overturning of the Indian Ocean; Ocean-wide transports of energy, fresh water, and constituents; Response of the North Indian Ocean to the monsoons in the 1990s; Non-monsoonal variability of the Indian Ocean; Collaborative development and testing of Indian Ocean models; Data products, especially general climatology.

It is intended that mornings will be devoted to discussions of the large topics, with each session having at least one lead talk. It is anticipated, however, that the main benefits of the meeting will derive from informal conversations, so most afternoons are intended to be entirely unscheduled (except as arranged by participants at the meeting), to allow people as much opportunity as feasible to get together on their own, to exchange information and ideas, and to explore collaborations as they think best.

The organising committee believes that projects easily accomplished by one or two scientists do not need organisational assistance of this sort, so they will not be emphasised at this meeting. Nevertheless, as a way of acquainting people with one another's work, participants are invited (if they choose) to display posters highlighting their particular activities, the larger efforts to which they would like to contribute, and pertinent results. It is planned that the posters will be set up the first afternoon, that the authors will be asked to stand by their posters for part of the afternoon, and that the posters will be left up for the duration of the meeting. The organising committee will try to sort the posters so that they can be grouped on the floor roughly by subject matter. It is therefore requested that, when participants register for the meeting, they state (a) whether they intend to display a poster, and, if so, (b) to which of the six topics listed above it corresponds (or, if to none, then "General").

Registration should be made with the US WOCE Office not later than 20 August. Details about registration, accommodation, and transportation are in the meeting announcement in US WOCE Notes (Vol. 10, No. 1, 1998). For further assistance please contact Maureen Reap at the US WOCE Office (mreap@tamu.edu). Limited financial support may be available through the WOCE IPO to whom applications should be forwarded.

Ocean Model Data Storage



*Peter McIntosh, CSIRO Division of Marine Research, Hobart, Australia.
Peter.McIntosh@marine.csiro.au*

Here's a challenge! Send an output file from your favourite model to a modeller at another institution. Ask them to record how long it takes them to read the file and plot, say, a meridional salinity section. Then ask them to plot the same section as an anomaly from the Levitus climatology. The whole process should take less than two minutes!

How is this possible? Here's how I do it. The data arrives in a standard format called netCDF. I start the visualisation and analysis package called Ferret, open the data set, choose the y-z section option, point and click on a map of the world to set the longitude, then press the contour button. Instant publication quality graph, fully labelled. Elapsed time is under a minute. I then open our Levitus climatology file, which is also stored in netCDF form, define a new variable within Ferret as the difference between the two salinity fields, and plot this. Elapsed time less than two minutes. At least in theory. In practice I had to call in our Ferret expert for this part to show me how to subtract variables defined on different grids.

The real message here is that using a standard data storage format saves an enormous amount of time in visualising and analysing model output. This is particularly true when sharing model output with colleagues. It is more likely that someone else will be bothered looking at output from your model if they don't have to spend a lot of effort converting your data into a format readable by their analysis package. There is, of course, a catch – there is more than one "standard" data storage format.

Which Format?

First a disclaimer; I am not an expert in data storage standards. I have only used netCDF. What information I have is mainly obtained from the WWW. There are far too

many data storage standards out there. I found a list of 19 in one place. However, a quick survey of the information available on the Web about large-scale ocean models suggests there are only a few standards being used. As you can see from the Table, the majority of the models use their own formats.

GRIB is a WMO standard for compression and electronic transmission of gridded atmospheric data. It is also used as a data storage format. GRIB has the advantage that ocean model output will be convenient for atmospheric scientists to analyse, for example in the context of a coupled atmosphere/ocean model experiment. For more information on GRIB, start with http://dao.gsfc.nasa.gov/data_stuff/formatPages/GRIB.html. I must say I was not motivated to investigate GRIB very thoroughly. It seemed complicated, I couldn't find any packages which implemented the standard in an easy-to-use interface, and it seemed generally restricted to the atmospheric community. The only software packages I could find which read GRIB files were GrADS and MAGICS.

netCDF data files store arrays of any dimension, together with essential ancillary information such as the units of the array, value used for missing data, and the coordinate axes of the array. The files are intended to be completely self-describing. Hence plotting packages such as Ferret can produce high-quality annotated plots with minimal effort. netCDF files store data in binary form, so they are as small as possible without using compression techniques. It is possible to store data in scaled integer*2 format if space is a real issue. The files are random access so that it is quick and easy to extract subsets of the data. netCDF files are machine-independent. They can be copied directly from PC to CRAY to UNIX workstation and read immediately provided that the netCDF library routines are installed. This library is freely obtainable from the Web, and can usually be installed easily and quickly.

The netCDF library provides FORTRAN and C sub-routines for reading and writing netCDF files. It is also possible to read and write netCDF files from within analysis and plotting packages such as Ferret and MATLAB. There are many more free and commercial packages which manipulate or display netCDF files. A good starting point for information on netCDF is <http://www.unidata.ucar.edu/packages/netcdf>.

netCDF is a quite general standard for storage of any type of gridded data. For specific applications it helps to have some conventions regarding attributes such as units and naming of axes. For oceanographic and atmospheric applications, a set of conventions have been defined by the Cooperative Ocean/Atmosphere Research Data Service (COARDS). These conventions assist packages such as Ferret in producing annotated plots automatically. See http://ferret.wrc.noaa.gov/noaa_coop/coop_cdf_profile.html

<i>model</i>	<i>standard used</i>
AIM	none
CME	none
FRAM	none
HOPE	GRIB
LSG	none
MICOM	none
MOM2	partial netCDF
MOM3	netCDF
OCCAM	HDF
OPYC	none (?)
POCM	none
POM	none
POP	none
SPEM	netCDF

for further details.

It is worth mentioning briefly the EPIC system for management, display and analysis of in-situ oceanographic data. Developed at the Pacific Marine Environmental Laboratory (PMEL) in Seattle, this package is related to Ferret, and is also based on netCDF and the COARDS standard. For further details see <http://www.pmel.noaa.gov/epic>.

HDF is similar in most respects to netCDF. It appears to be more flexible, in that you can define almost any data structure at all – the definition is stored along with the data. In addition, it has the ability to use several compression techniques. Recent versions of HDF include the netCDF interface, and it is now possible to write HDF files using netCDF-style syntax. There are still some restrictions on merging HDF and netCDF structures, and analysis packages are in the process of catching up with the blending of the two formats. For more information, start with <http://hdf.ncsa.uiuc.edu>. Again, there is an enormous range of analysis and visualisation packages which work with HDF files. A notable exception is Ferret, although I presume that if one uses HDF to write netCDF files (using the COARDS conventions, of course) then Ferret will work. I haven't tried it.

There are just a few issues to consider in moving towards using netCDF or HDF. First, I/O speeds can be slow if the package has not been optimised for the machine architecture. This has been a problem with vector supercomputers. I believe netCDF now runs much faster on Cray supercomputers. Second, standards such as COARDS have not considered conventions for curvilinear coordinate systems. So while netCDF and HDF can store output from non-Cartesian models, the plotting packages currently need some manual intervention to get some plots. Finally, these data storage standards are not really set up for handling real

data in an efficient way. They are much better with gridded data. Although this doesn't affect pure modellers, if you're into data assimilation this may be an issue. I store hydrographic casts and XBT data in simple 2-D arrays with the first dimension just an index and the second dimension depth, and tolerate the extra storage if casts don't extend to the bottom.

Finally, I speculate that the days of sending ocean model output to anyone at all are probably over! It is already possible to request ocean model output over the Web using tools based on Java. As an example, look at <http://www.soc.soton.ac.uk/JRD/OCCAM/JAVA/data.html>. It is also possible now to view animations of data using Java. For an example look at <http://www.pmel.noaa.gov/toga-tao/java/ani/taosst.html>. Atmospheric climate data is now available from the Web from a number of sources; see the article by Scott et al. (1997). I note that the data sets referred to in this article are stored in netCDF form.

Conclusion

For oceanographic modellers the choice of a data storage standard probably comes down to netCDF or HDF, although the issue of trying to be compatible with atmospheric modellers should be considered. Since netCDF has been incorporated into HDF, the latter seems the most logical choice. I will probably stick with netCDF for a while yet. It does the job perfectly well. Ultimately it doesn't matter whether you choose to use netCDF or HDF so much as whether you use a standard format at all.

Reference

Scott, J., M. Alexander, J. Collins and C. Smith, 1997: Interactive visualization of climate data on the World Wide Web. *Bull. Amer. Meteor. Soc.*, 78, 1985–1989.

First Announcement: WOCE-AIMS Tracer Workshop

A WOCE-AIMS Tracer Workshop will be held in Bremen, Germany, 22–26 February 1999.

WOCE has produced a large tracer dataset of unprecedented spatial density at world-wide coverage of the ocean. Tracer data constrain ocean circulation and mixing, both directly and in the framework of models. They yield information particularly on water mass formation and thermohaline circulation on annual and decadal time scales, and can be used to test and verify the related parts of ocean circulation models. Various groups have contributed to the WOCE tracer dataset. Because by now the great majority of the tracer data is available, and considering that the data by and large have to be interpreted on basin scales, a workshop to bring together the producers and users of the tracer data is timely.

The objectives of the workshop are: (1) Further the oceanographic interpretation of the WOCE tracer data sets; (2) Encourage the synthesis, compilation and dissemination

of tracer data sets; (3) Establish mechanisms for the production of data products (gridded and derived) for the use of a broader community; (4) Identify strategies to facilitate assimilation and incorporation of tracer data into models; (5) Initiate collaboration and interaction between tracer geochemists and modellers.

A planning group has been established consisting of: Wolfgang Roether, Bremen, Germany (co-chair); Scott Doney, Boulder, USA (co-chair); William J. Jenkins, SOC, UK; Yukata Watanabe, Ibaraki, Japan; William W. Smethie, Palisades, USA; Claus Böning, Bremerhaven, Germany; Mathew England, Sydney, Australia.

The detailed format of the workshop will be announced later, and suggestions are appreciated. To facilitate the organisation of the workshop, everybody interested in participating is asked to inform the co-chairs (mail to wroether@physik.uni-bremen.de, doney@ncar.ucar.edu, including full mailing address, fax and e-mail).

The Rate of Formation of the Subtropical Underwater (STUW) in the North and South Pacific from Drifter and Tracer Data



Bridgette M. O'Connor, Rana A. Fine, Kevin A. Maillet and Donald B. Olson,
University of Miami, FL, USA. occonnor@gecko.rsmas.miami.edu

The STUW is a thermocline water mass formed in the subtropical regions and is characterised by a salinity maximum in the vertical, with the core centred at 24.3 and 24.8 σ_θ in the North and South Pacific, respectively. STUW is important in terms of its contribution to the heat and salt budgets. A superposition of the Ekman and geostrophic flows cause the saline waters, formed in the poleward half of the subtropical gyres, to be advected equatorward and subducted as STUW under a layer of fresher waters (Schmitt et al., 1989; Worthington, 1976). The subducted high salinity water is carried equatorward in the Sverdrup circulation, to be upwelled near the equator (Fine et al., 1987) and subsequently freshened under the Inter-Tropical Convergence Zone (ITCZ) (Quay et al., 1983). Although the STUW is common to all oceans, there appears to be no previous formation rate estimate. The approach used here ties the formation to the subduction process, and the subduction rate is calculated using two independent methods from Marshall et al. (1993) and Jenkins (1998) using drifter and tracer data, respectively.

Data

The Reid hydrographic data were used to define the properties of the core of the STUW and its vertical and horizontal extent in the Pacific. The Levitus (1982) climatology was used to determine mixed layer depths and to compute geostrophic velocities.

The chlorofluorocarbon (CFC) data are from WOCE (Fine et al., 1998) and Pacific Marine Environmental Laboratory (PMEL) (Wisegarver et al., 1993). The WOCE data used consist of stations from: P17N (1993), P17C (1991) and P21E (1994). The PMEL data consist of stations from: CO2-87 (1987), CO2-88 (1988), CO2-89 (1989) and TEW-87 (1987). The PMEL and WOCE CFCs were analysed using procedures from Bullister and Weiss (1988). All data was converted to the SIO-1993 scale. The analytical precision for WOCE CFC-12 samples >0.1 pmol/kg were 0.8-5% (Fine et al., 1998). For low concentration PMEL CFC-12 samples, the analytical precision was 0.005–0.015 pmol/kg and for higher concentrations, it varied between 0.5% and 2%, with sampling and handling errors on the same order (Wisegarver et al., 1993).

Satellite tracked surface drifter buoy data from WOCE/TOGA (Tropical Ocean/Global Atmosphere) were used to calculate the annual mean velocity components (1988–1992) (Olson et al., 1998, in prep.). Drifters were drogued to 15 m depth and were used to obtain fifty day mean fields of u , v and SST assigned to bins.

STUW formation area

The formation area was defined by an overlap of the STUW potential temperature and salinity range at the surface. Satellite SST data for 1989 were used to determine the surface area of STUW properties. The salinity data used is from Levitus (1982) surface salinity climatology. The average area and standard deviation was calculated for each season. The difference between the spring and summer area is defined as A_{diff} , and is used to obtain a net volumetric subduction rate (formation rate). This spring-summer area difference is used because not all the water formed in the late winter and early spring is subducted, but some remains in the mixed layer after subduction has occurred in spring.

Subduction Rate from drifter data: Method 1

Marshall et al. (1993) define S_{ann} (the annual subduction rate at which fluid irreversibly transfers into the permanent thermocline) as:

$$S_{ann} = -[w_{Ek} - (\beta/f)(v)h_w + u_w \cdot \nabla h_w] \quad (1)$$

The vertical velocity at the winter mixed layer's base (w_w) is related to the Ekman pumping (w_{Ek}) using the linear vorticity balance:

$$w_w = w_{Ek} - (\beta/f)(v)h_w \quad (2)$$

where f is the planetary vorticity, β is its meridional gradient. The quantities u_w and w_w are the annual mean horizontal and vertical velocity components at the interface $z = -h_w(x, y)$ (the base of the deepest winter mixed layer).

The assumptions in the calculation of w_{Ek} are:

- (1) The Ekman depth (h_{Ek}) is equal to the annual mean mixed layer depth (h_{ann}).
- (2) The vertical velocity at the sea surface is zero.
- (3) The horizontal divergence of the flow is constant with depth in the mixed layer.

Ekman pumping is calculated by integrating the continuity equation from the surface to h_{Ek} :

$$w_{Ek} = -(\partial u / \partial x + \partial v / \partial y)h_{Ek} \quad (3)$$

The quantity h_w has been calculated from Levitus (1982) winter climatological data. The mean velocities have been calculated for 1988–1992 by Olson et al. (1998, in prep.) where they decompose the surface circulation from the WOCE/TOGA drifter dataset into geostrophic

and ageostrophic components. The averaging consists of a Lagrangian temporal average over each drifter followed by an ensemble average to provide data on a grid. The geostrophic currents and reference levels were computed by minimising the difference between drifter velocities and geostrophic ones. The residuals are in agreement with an Ekman result over the area of interest here. All the averaging is done on a grid over an area defined by an overlap of the formation and the core region. A_{diff} is multiplied by $S_{\text{ann}}(\text{m/s})$ (from eq. 1) to get an annual volumetric subduction rate, $S_{\text{ANN}}(\text{m}^3/\text{s})$ (formation rate).

Subduction Rate from CFC-12 data: Method 2

The subduction rate (w_s) for an isopycnal projected back to its outcrop given by Jenkins (1987) is:

$$w_s = f_o / [f(\delta\tau / \delta z)] \quad (4)$$

where f_o and f are the Coriolis parameters at the outcrop and at the latitude where the water is found, z is the depth, and τ is the age, where the age is zero at the sea surface, and increases with increasing distance along the outcrop surface. The annual volumetric formation rate (m^3/s) is given by equation (4) multiplied by A_{diff} .

The CFC-12 ‘apparent age’ is calculated by comparing partial pressures to the atmospheric time histories (Walker et al., personal comm.) (Fine et al., 1988; Doney and Bullister, 1992). The equilibrium partial pressure (P_{CFC}) is calculated from:

$$P_{\text{CFC}} = \frac{\text{CFC}_{\text{seawater}}}{F(\theta, S)} \quad (5)$$

where F is the CFC-12 solubility coefficient from Warner and Weiss (1985).

This approach assumes that the CFC-12 age represents the true ‘advective age’. The age is influenced by mixing which tends to decrease the apparent age and age gradient. To correct for mixing, a one-dimensional pipe model was run to 1991 (diffusivity = $1000 \text{ m}^2/\text{s}$) for various velocities (Jenkins, 1998). The pCFC-12 ages are in good agreement with the advective ages, with the CFC-12 ages younger by 0.4–0.5 year on average, for ages ranging from 1–10 years. The results of the pipe model are used to correct the age gradient.

Error analysis

A component of error in the two methods is due to the error in the formation areas calculated from satellite data, which are estimated at 7% in the North and South Pacific. The drifter method contains errors inherent in the measured velocities and the analysis, errors due to eddy noise and Levitus data. The overall errors estimated in the drifter subduction rates are about 20%. In the tracer

method, mixing effects on the CFC-12 ages were corrected to some extent. Errors due to the analytical precision, sampling and handling, equilibrium, and non-stationarity were estimated. The cumulative errors in the tracer data result in, about a 15% error in the subduction rates.

Results and discussion

The drifter and tracer methods give subduction and formation rates which agree very well (Table 1). Maps of the drifter (Fig. 1a, page 25) and tracer (Fig. 1b, page 25) calculated subduction rates show similar features with extrema located in the same regions. Maxima have values $>40 \text{ m/yr}$ in the North, and $>50 \text{ m/yr}$ in the South Pacific, located near regions of strong wind stress curl.

The formation, distribution and frequency of Pacific STUW is affected by changes in the large scale atmospheric forcing. Lukas et al. (1997) find that the magnitude of the salinity maximum near Hawaii varies markedly on short and long timescales. The trend shows relatively fresh STUW in 1989, 1992 and 1993 and salty STUW in 1990, 1991 and 1994. This suggests higher formation rates during the latter years. For the drifter and tracer data, there is an equal distribution of ‘fresh’ and ‘salty’ years so there should be little bias related to the variability observed near Hawaii.

In summary, a plausible pattern of the STUW subduction rate is obtained over the subtropical Pacific using two independent methods. The drifter and tracer STUW subduction rate maps agree very well, with high rates located near regions of strong wind stress curl. This indicates that STUW formation is driven by the local wind stress curl and suggests that buoyancy effects are small, and may be important for pre-conditioning rather than driving the formation process. However, these maps show the large scale features of the STUW subduction rate during 1987–1994. The next step is to get an understanding of the variability in the formation of STUW under different climatic conditions.

Table 1: Pacific STUW SANN from both methods. All contributions shown for Method 1.

Method	North Pacific				South Pacific			
	Drifter		Tracer		Drifter		Tracer	
	Sv	m/yr	Sv	m/yr	Sv	m/yr	Sv	m/yr
S_{ANN}	4.8	26	4.7	26	6.6	30	7.0	32
$-u_w \cdot \nabla h_w$	2.5	12			2.7	12		
$-w_w$	2.3	12			3.9	18		
$-w_{\text{EK}}$	2.8	15			7.0	32		
β term	-0.5	-3			-3.1	-14		

Acknowledgements

The authors gratefully acknowledge the analysis of CFC data under the direction of Kevin Sullivan. We also wish to acknowledge the chief scientists on the legs of the WOCE cruises including: Mizuki Tsuchiya, Jim Swift and Mike McCartney, without whom this work would not have been possible. We are also very grateful to John Bullister and D. Wisegarver for sharing their data. Additionally, this work has been funded through grants from the NSF, numbered OCE9207237, OCE9314447 and OCE9413222.

References

- Bullister, J., and R. Weiss, 1988: Determination of CCl_3F and CCl_2F_2 in seawater and air. *Deep-Sea Res.*, 35, 839–853.
- Doney, S., and J. Bullister, 1992: A chlorofluorocarbon section in the eastern North Atlantic. *Deep-Sea Res.*, 39, 1857–1883.
- Fine, R., W. Peterson, and H. Gote Ostlund, 1987: The penetration of tritium into the Tropical Pacific. *J. Phys. Oceanogr.*, 17, 553–564.
- Fine, R., M. Warner, and R. Weiss, 1988: Water mass modification at the Agulhas Retroflection: chlorofluoromethane studies. *Deep-Sea Res.*, 35, 311–332.
- Fine, R., K. Maillet, K. Sullivan and D. Willey, 1998: Circulation and ventilation flux of the Pacific Ocean. (in prep.)
- Jenkins, W., 1987: ^3H and ^3He in the Beta triangle: Observations of gyre ventilation and oxygen utilization rates. *J. Phys. Oceanogr.*, 17, 763–783.
- Jenkins, W., 1998: Studying thermocline ventilation and circulation using tritium and ^3He . *Proceedings of the Ewing Symposium*. (in press.)
- Levitus, S., 1982: *Climatological Atlas of the World Ocean*. NOAA Prof. 13, US Govt. Printing Office.
- Lukas, R., F. Santiago-Mandujano, and E. Firing, 1997: Long-term hydrographic variations observed in the Hawaii Ocean time-series. (in press)
- Marshall, J., A. Nurser, and R. Williams, 1993: Inferring the subduction rate and period over the North Atlantic. *J. Phys. Oceanogr.*, 23, 1315–1329.
- Olson, D., G. Samuels, and P. Niiler, 1998: Decomposition of surface momentum balances from WOCE/TOGA drifter arrays. (in prep.)
- Quay, P., M. Stuiver, and W. Broecker, 1983: Upwelling rates for the equatorial Pacific Ocean derived from the bomb C-14 distribution. *J. Mar. Res.*, 41, 769–792.
- Schmitt, R., P. Bogden, and C. Dorman, 1989: Evaporation minus precipitation and density fluxes for the North Atlantic. *J. Phys. Oceanogr.*, 19, 1208–1221.
- Warner, M., and R. Weiss, 1985: Solubilities of chlorofluorocarbons 11 and 12 in water and seawater. *Deep-Sea Res.*, 32, 1485–1497.
- Wisegarver, D., J. Bullister, R. Gammon, F. Menzia, and K. Kelly, 1993: NOAA Chlorofluorocarbon Tracer Program Air and Seawater Measurements: 1986–1989. NOAA Data Report ERL PMEL-43.
- Worthington, L., 1976: On the North Atlantic circulation. *Johns Hopkins Oceanogr. Stud.*, 6, 110 pp.

Erratum

Eric Firing, University of Hawaii, Honolulu, USA. efiring@iniki.soest.hawaii.edu

In the previous issue of the WOCE Newsletter (No. 30), the article by Firing (pages 10–14) contains a serious error of fact. Due to a programming error, Figure 2 on page 12 of that issue shows LADCP velocities that are systematically too small. In the corrected fig. 2, shown below, the high-frequency variations in depth-averaged LADCP velocity match the predictions of the tide model (Egbert et al., 1994; Dushaw et al., 1998) to a remarkable degree, suggesting that a large fraction of the LADCP variance due to barotropic tides can be removed simply by subtracting out the model prediction. I would like to thank Brian Dushaw for pointing out to me the high degree of consistency between other

direct velocity measurements and the tide model predictions; his persistence on this point eventually led to the discovery of the error in the original version of Figure 2.

References

- Dushaw, B. D., G. D. Egbert, P. F. Worcester, B. D. Cornuelle, B. M. Howe, and K. Metzger, 1998: A TOPEX/POSEIDON global tidal model (TPXO.2) and barotropic tidal currents determined from long-range acoustic transmissions. *Progr. Oceanogr.*, in press.
- Egbert, G. D., A. F. Bennett, and M. G. G. Foreman, 1994: TOPEX/POSEIDON tides estimated using a global inverse model. *J. Geophys. Res.*, 99, 24,821–24,852.

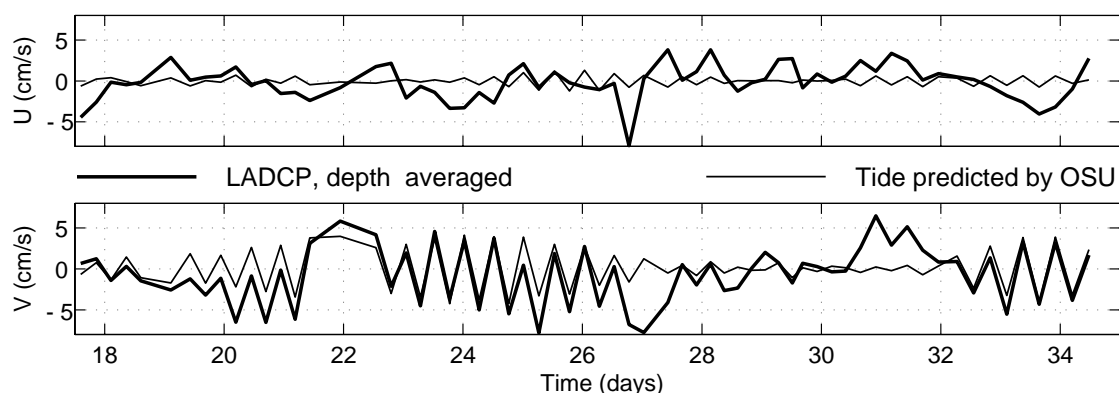


Figure 2. Depth-averaged currents (east component in the top panel, north below) from the LADCP on the second half of the WHP Indian Ocean 19 line, compared to the prediction of the OSU TOPEX/POSEIDON crossover global inverse solution version 3.0 (Egbert et al., 1994), averaged over the duration of each station. Time is in days from the first station of the cruise.

South Atlantic Chlorofluoromethane Distributions Along the WHP Lines A17, A13 and A14

Marie-José Messias, School of Environmental Sciences, University of East Anglia, UK; and
Laurent Memery, LODYC, CNRS-ORSTOM-UPMC, Paris, France. M-j.Messias@uea.ac.uk



Chlorofluoromethanes CFC-11 and CFC-12 were measured in the South Atlantic Ocean along the western boundary (WHP line A17) and in the eastern basin (WHP lines A14 and A13) during the cruises CITHER 2 and CITHER 3, as part of the French WOCE contribution (Fig. 1). The main north-south A17 section was completed by three short transverse lines across the Western Deep Boundary Current (DWBC) to the continental slope (35°S, 13°S and 10°N). All made during January–March 1994, they provide a quasi-synoptic picture of the western boundary system of the Equatorial and South Atlantic in conjunction with recirculation gyres in the ocean interior. East of the Mid-Atlantic Ridge (MAR), the A14 and A13 sections were made during the following austral summer in January–March 1995. They extend respectively along the MAR (9°W) and about 10° off the African coast. This note presents some of the main features in both CFC data sets (Figs. 2 and 3), giving a highlight of the recent ventilation of the South Atlantic in particular at abyssal, deep and intermediate levels. At the deepest levels, CFC-rich Antarctic Bottom Water (AABW) entering the South Atlantic is visible in the three main sections A17 (Fig. 2a), A14 (Fig. 3a) and A13 (Fig. 3b). In the south-eastern Atlantic, the bottom CFC maxima of the AABW was found on A14 and A13 extending northward to the Walvis Ridge. Then, both sections cross the Angola Basin and show undetectable levels of CFC-11 (as well as CFC-12) in the deep waters as observed in March 1991 on the WHP A9 line along 19°S (Wallace et al., 1994). Within the Cape Basin, the short section from 10°E to the African Coast (Fig. 3c) shows the CFC-rich bottom layer all along the section with an intensification against the continental slope of South Africa. The intrusion of CFC-rich AABW is more important in the Argentine Basin (A17, Fig. 2a) where it enters mainly through the South Sandwich Trench. The more recently ventilated Weddell Sea Deep Water (WSDW) originating from the Weddell Sea Gyre contains higher CFC concentrations (mainly >0.1 pmol/kg) when compared to the overlaying layer of the less dense Lower Circumpolar Deep Water (LCDW around 3500 db) coming from the Drake Passage. At the level of the LCDW interesting features have been observed as deep anticyclonic eddies in particular around 45°W in the short 35°S section (Fig. 2b). The most CFC rich water was found in the southern deepest part of the Argentine Basin (6 km) and also north of the Zapiola Rise (5.2 km) with values reaching 0.2 pmol/kg suggesting that they correspond to younger/less diluted water mass. The 35°S section across the Western Boundary (Fig. 2b) shows only a slight intensification of the bottom maximum (0.15 pmol/kg) against the western boundary at 46.5°W,

but the maximum depth of the section remained above 5000 db. The zonal CFC distribution across all the Argentine Basin at 45°S (WHP line A11) have been measured by Smythe-Wright and Boswell (1995) early 1993. They observed higher CFC values along the western flank of the MAR compared to the south-western basin. They suggested that abyssal water bifurcates at the northern side of the Falklands Escarpment, reducing the western boundary flow, with a dominant movement north-eastward entrained by the Antarctic Circumpolar Current (ACC) as far as 40°S (MAR) and then that it gyres anticyclonically around the Zapiola Rise. The Argentine Basin is almost fully enclosed below the 3000-m isobath. CFC-rich lighter WSDW spills mainly into the Brazil Basin across Rio Grande Rise through the Vema Channel (~32°S) where depths can be >4500 m. High CFC levels ~0.1 pmol/kg were found on A17 to around 23°S, then the bottom maximum decreases as it travels northward. The clear AABW CFC maxima follows closely the topography, extending northward along the bottom Brazil Basin as far as 1.5°S where it meets the Parnaiba Ridge. The A17 section (Fig. 2a) shows a large-scale view of southward flowing North Atlantic Deep Water (NADW) overlying northward flowing LCDW and AABW. The two familiar CFC signatures of the most recently ventilated NADW were observed on A17 as far as 25°S. They are associated with the Upper NADW

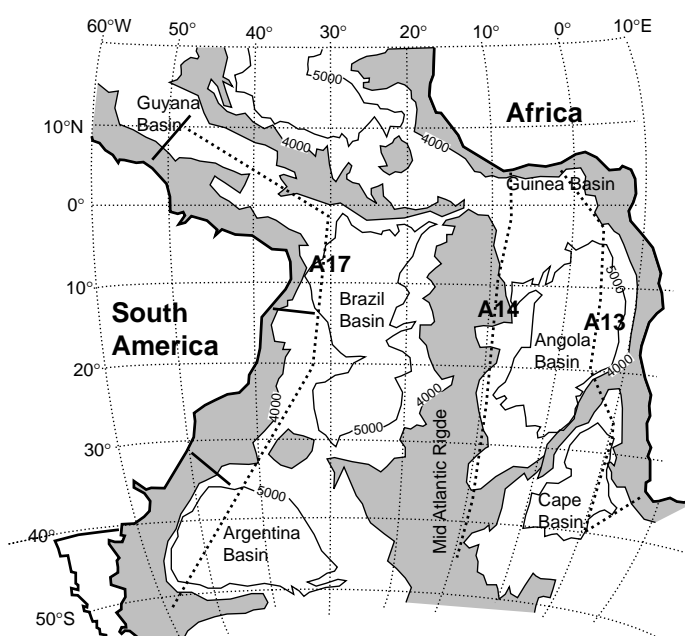


Figure 1. Locations of the stations occupied during the campaigns CITHER 2 and CITHER 3. Shading indicates depths shallower than 4000 m.

(UNADW) and with the Lower NADW (LNADW) centred in the equatorial region within the DWBC at ~1700 db depth and ~3800 db depth, respectively. Both maxima converge southward when the influence of the south originated waters increases. In particular the LNADW CFC maxima on A17 is observed at 4000 m depth at the equator, 3500 db at 10°S and then at 3200 db at 25°S. In the northern part of the A17 and on the short perpendicular section at 10°N (Fig. 2d), a third slight CFC maximum is also observed at the level of the Middle NADW (MNADW) around 2600 db. The three short sections across the DWBC (Fig. 2d, 2c, 2b) shows a CFC decrease within the NADW spreading southward along the continental slope. The section north of the equator (Fig. 2d), shows the clear NADW high CFC cores in the main southward flow within the DWBC against the Guinea slope. It is surrounded by CFC-free Circumpolar Deep Water (CDW) lying at 1000, 3000 m depth and AABW on the bottom. The UNADW presents two maxima, the first against the continental slope and a second offshore near 50°W, reflecting a north-westward recirculation in the Guyana Basin (Friedrichs and Hall, 1993). At 13°S (Fig. 2c), the CFC NADW concentration present a dramatic decrease when compared to the 10°N section. CFC LNADW cores are visible eastward as far as 32°W. At 35°S (Fig. 2b), the NADW lying between 2000 and 3000 db present now the lowest CFC values when compared to the surrounded south originated waters. The southward decrease of the NADW concentrations is due to ageing and mixing with the poor-CFC CDW but also is due to eastward bifurcations. The section A17 crosses the southward flow of the DWBC as well as complex recirculation and NADW zonal flows that contribute to the discontinuity in the observed NADW CFC signals. Three main meridian features are visible in the A17 CFC distribution within the NADW: the equatorial region with complex zonal jets and eastward flows around 10°S and between 20°S–25°S. The dramatic decrease of the NADW CFC values south of the equator on A17 is mainly due to the split of the DWBC water, with a part of it flowing eastward along the equator and another part continuing southward along the western boundary (Weiss et al., 1985). The equatorial zone of the A14 and A13 (Fig. 3a and 3b) is interesting as it intersects the equatorial spreading of the NADW CFC signals in the eastern basin. The upper UNADW maximum is observed on both sections around 1600 db indicating a spreading of recently ventilated UNADW along the equator as far as 2°W where it becomes narrower. On A13, south of the main equatorial UNADW

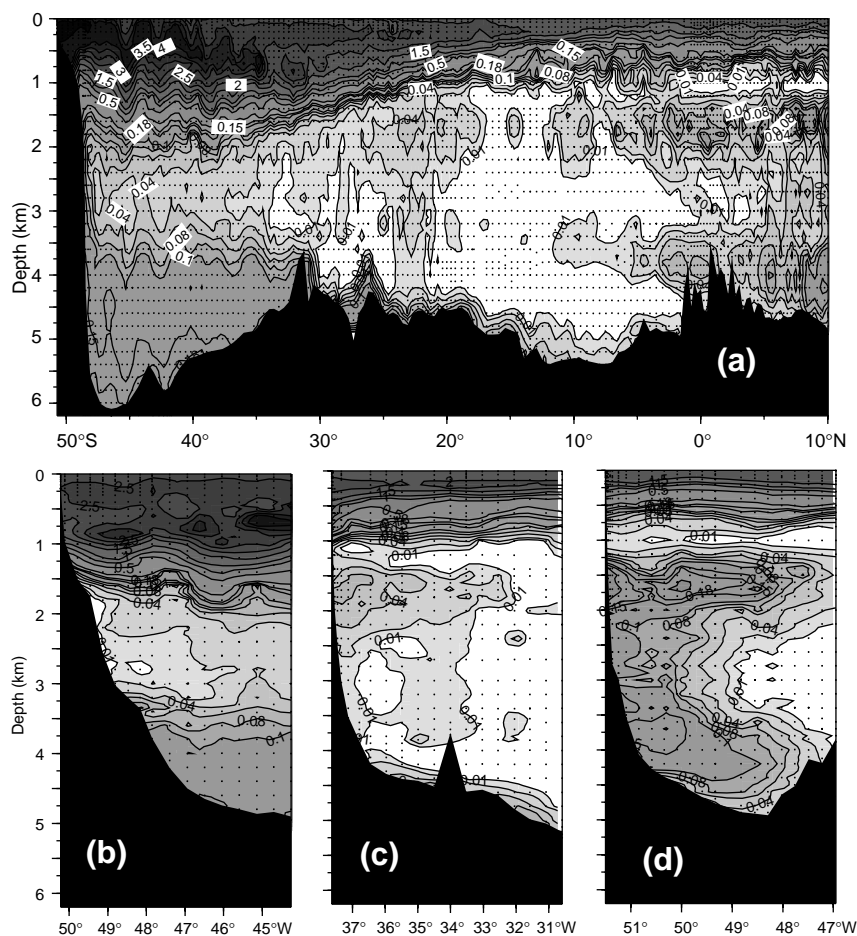
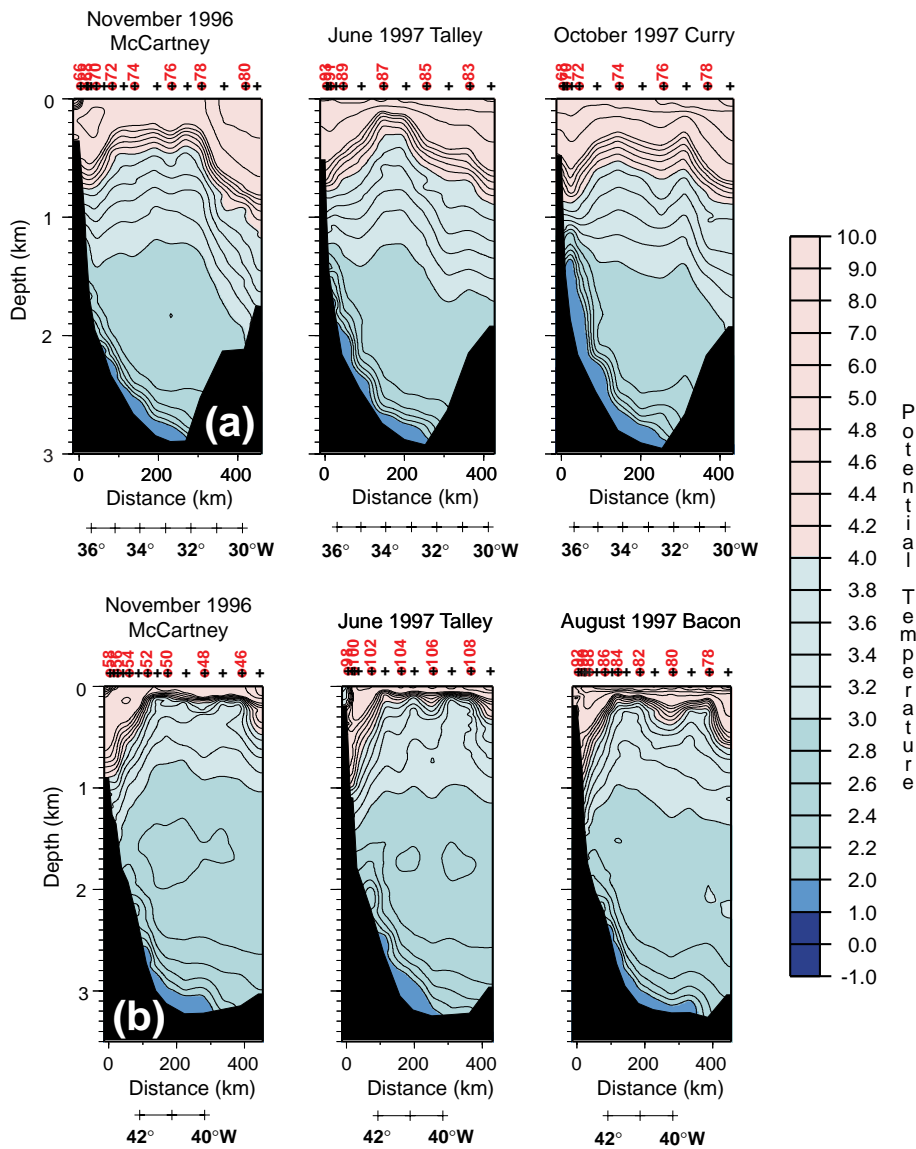
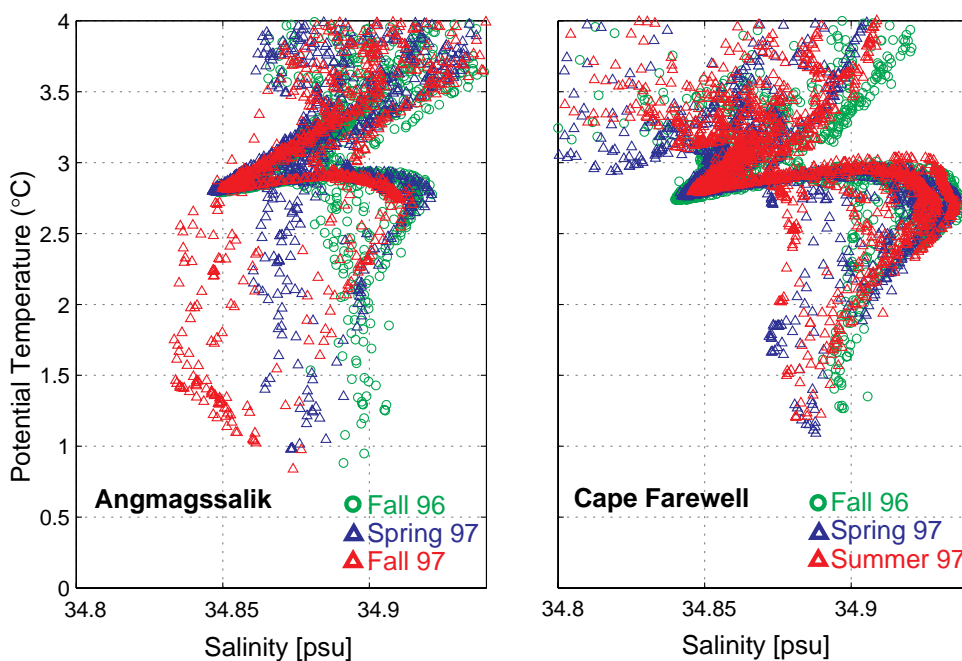


Figure 2. Vertical distribution of CFC-11 (pmol/kg) along A17 (a), and along the short transverse 35°S section (b), 13°S section (c) and 10°N section (d) across the western boundary.

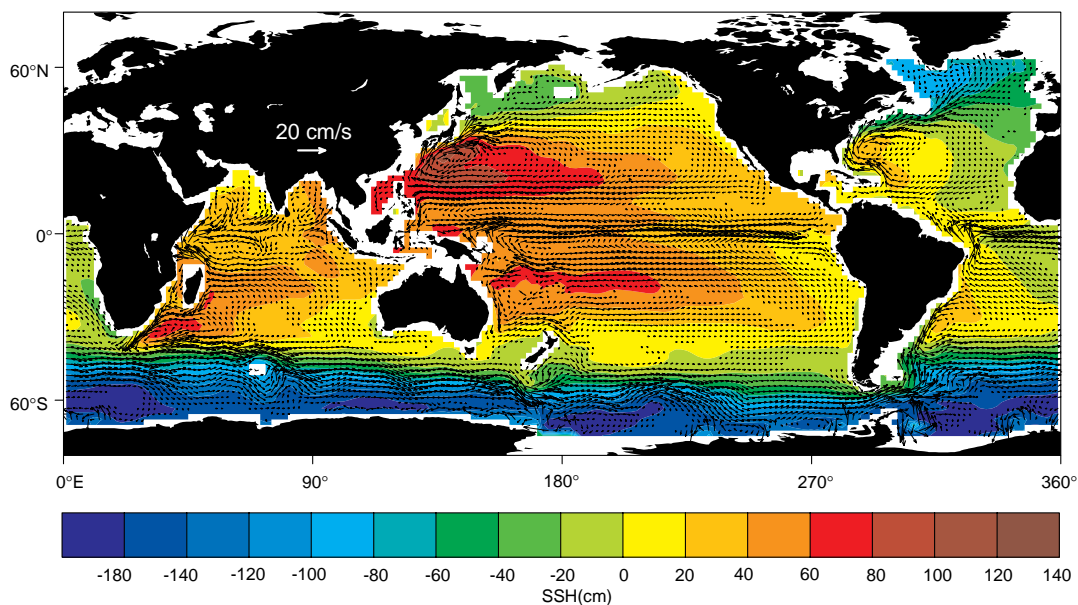
core, scattered CFC lenses are visible as far as 12°S, giving some evidence for a southward flow of the UNADW from the equatorial region along the eastern boundary (Warren and Speer, 1991). Concerning the eastward evolution of the LNADW CFC signal originally around 3800 db in the western basin, the A14 section shows a weak deep CFC maximum at greater depths around 4600 db in the Guinea Basin. This is the result of the mixing of the CFC-rich LNADW and densest CFC-free AABW formed during the eastward transit of the two water masses across the MAR through the Romanche and Chain Fracture Zone (Mercier and Morin, 1997; Messias et al., 1998). Further east, the deep CFC NADW signal was not detectable on A13. Zonal circulations of the NADW from the DWBC are also seen on the A17 section by the intersection of the UNADW and LNADW high CFC cores (surrounded by CFC-poor old NADW and intrusions of circumpolar origin water) at 10°S and 20°–25°S. Tsuchiya et al. (1994) observed eastward NADW flows around the same latitude on their 25°W hydrographic sections. However, the authors reported only the LNADW extension at 25°S, but not the UNADW one. No evidence of a continuity of these CFC signals has been observed in the eastern South Atlantic Ocean on A14. The arrival of the CFC LNADW signal so far south seems quite



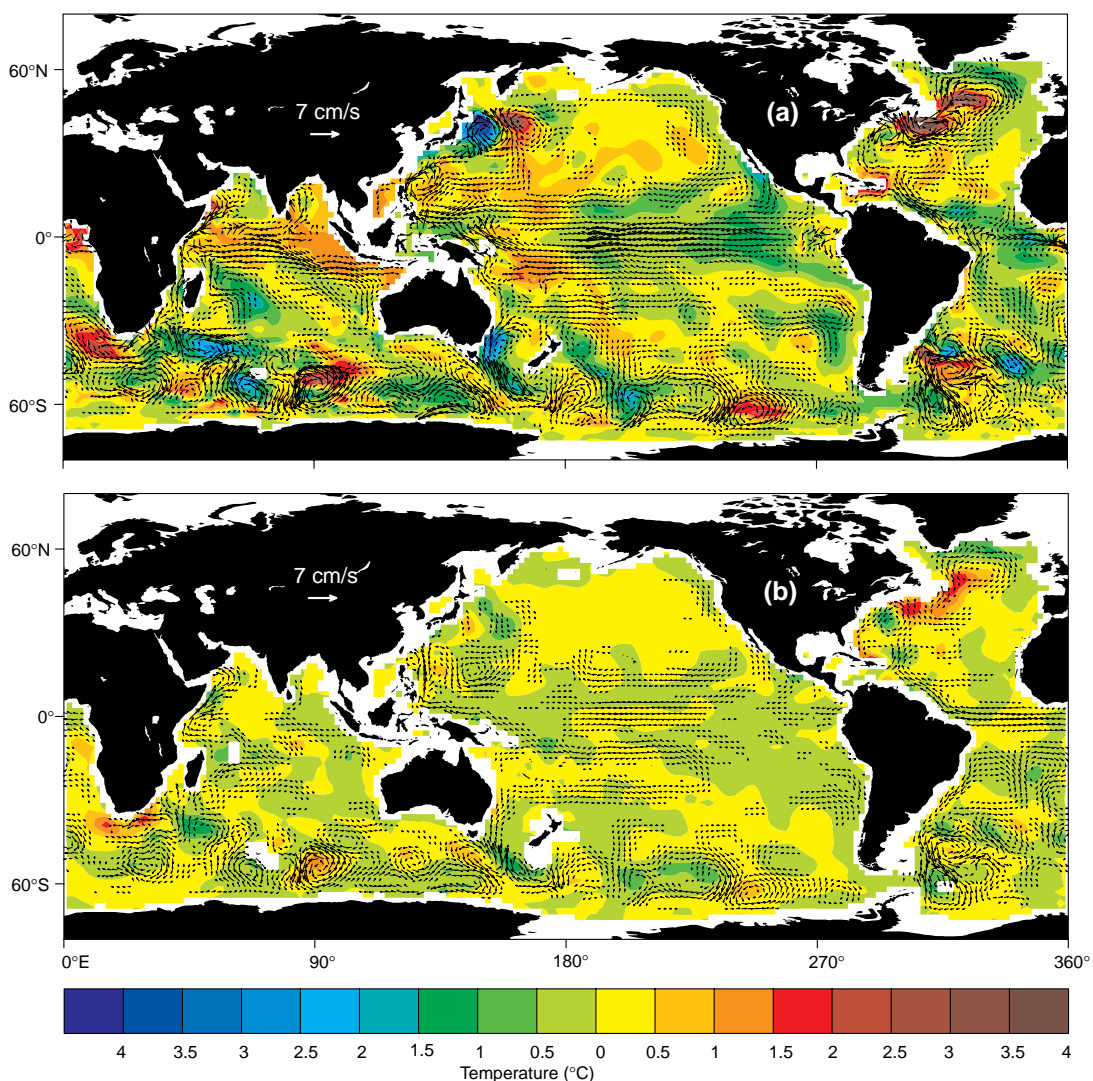
McCartney et al.,
page 3, Figure 2.
(a) Potential temperature along the three Angmagssalik sections. In these sections Greenland is on the left and you are looking northwards through the sections. (b) Potential temperature along the three Cape Farewell sections.



McCartney et al.,
page 3, Figure 3.
Potential temperature-salinity diagram for the Angmagssalik (left panel) and the Cape Farewell (right panel) sections.

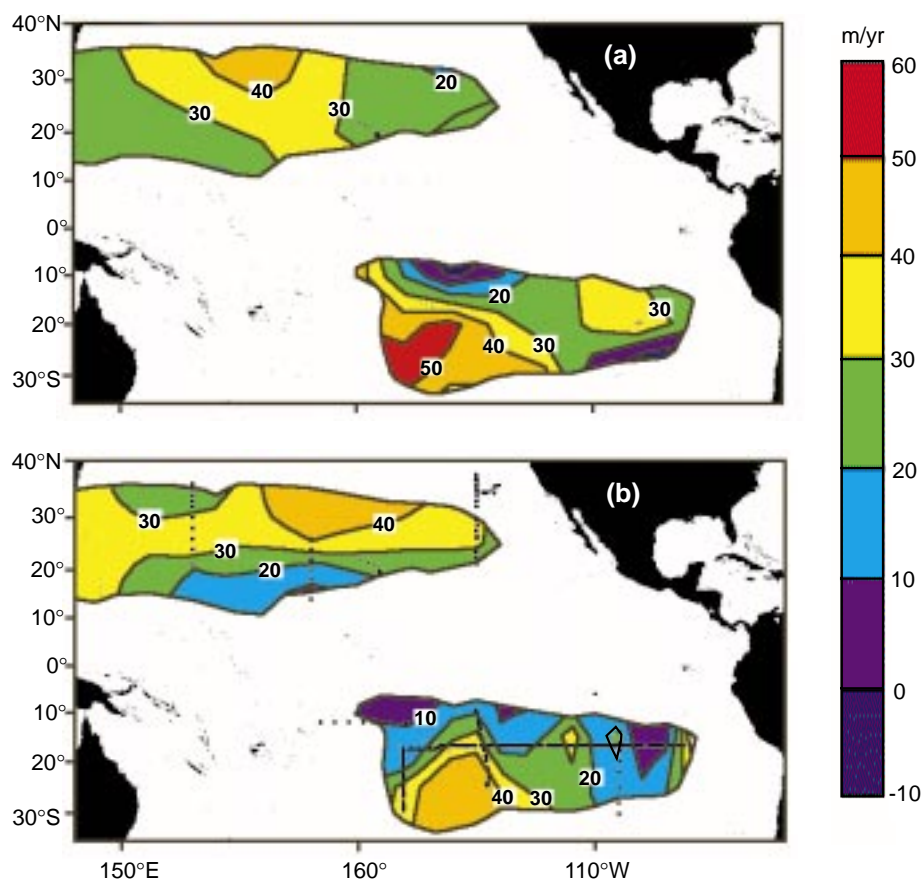


Stammer, page 8,
Figure 1. Estimates of a monthly mean sea surface height field and velocity field at 120 m depth from October 1993 as it results after optimisation. Contour interval is 20 cm for the surface elevation, and a reference velocity of 20 cm/s is shown. Velocities smaller than 1 cm/s in length were omitted from the plots.

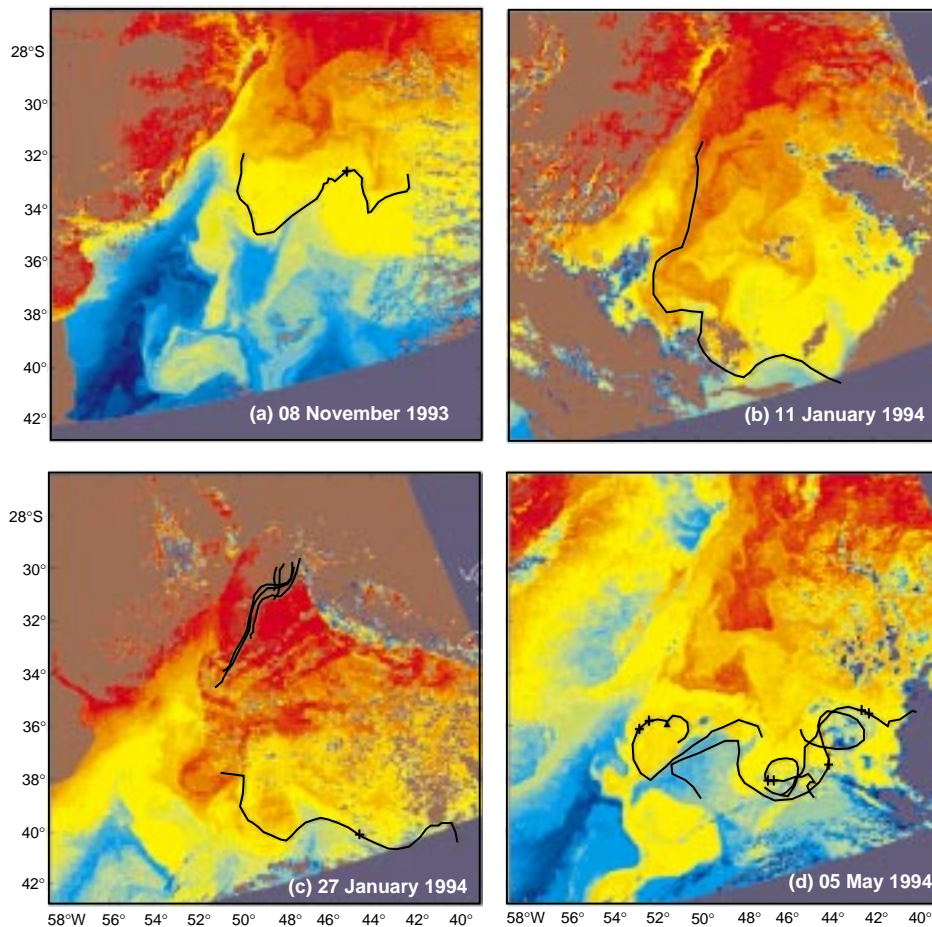


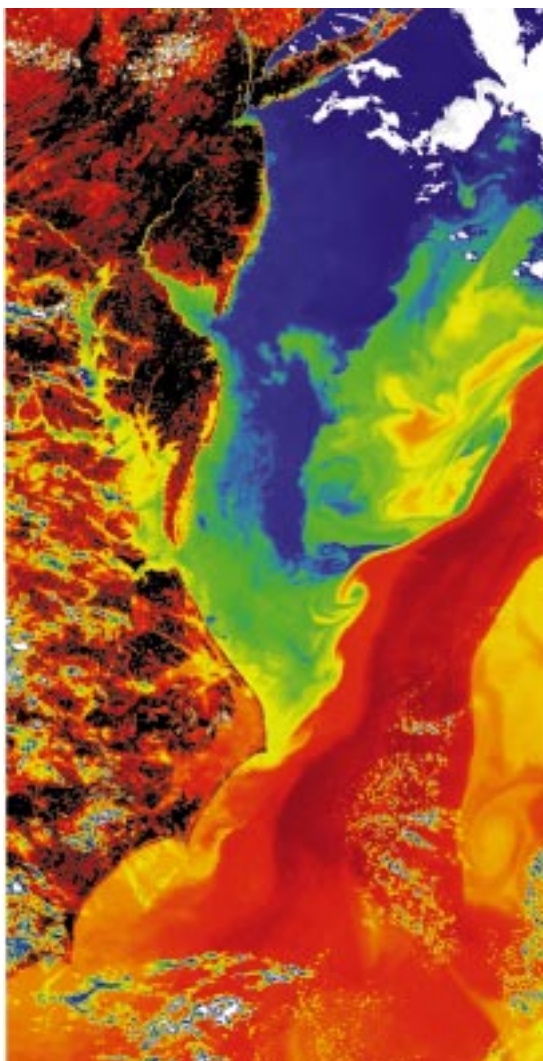
Stammer, page 8,
Figure 2. Change of monthly mean temperature and velocity fields in the estimated state relative to the unconstrained model. The difference fields are taken from October 1993 at (a) 120 m, and (b) 610 m depth, respectively. Contour intervals are 0.5°C, and a reference velocity of 7 cm/s is shown.

O'Connor et al., page 18,
Figure 1. (a) Pacific STUW Subduction Rate (m/yr) from Drifter Data. (b) Pacific STUW Subduction Rate (m/yr) from pCFC-12 Ages. Stations indicated by black circles.

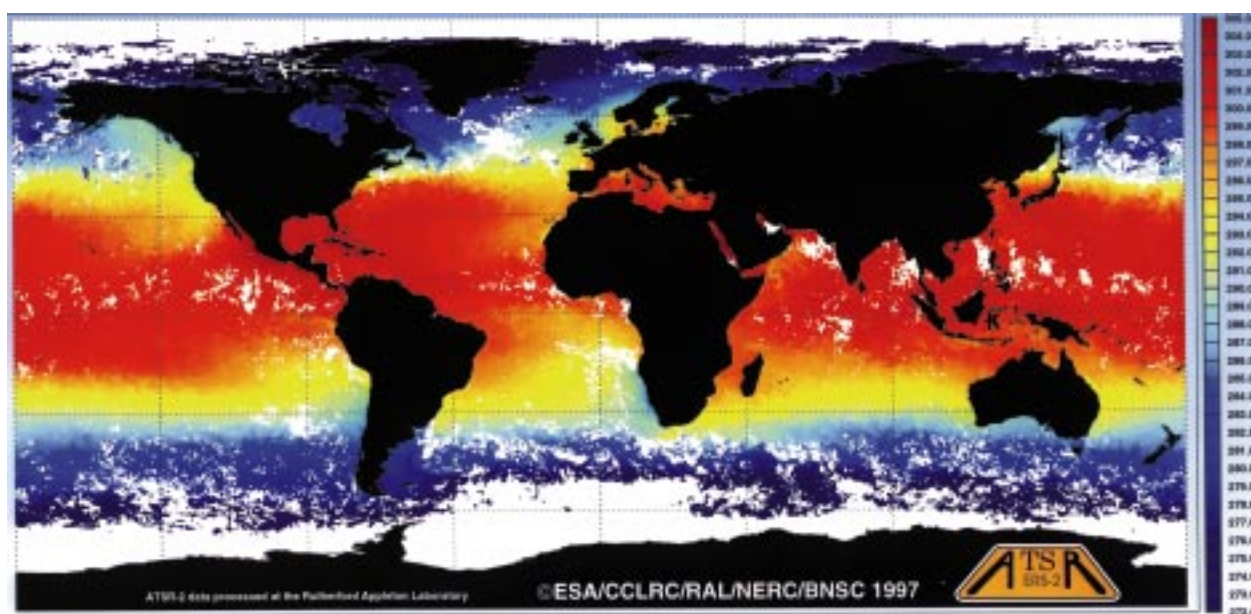


Buss de Souza and Robinson, page 32, Figure 2. Buoy tracks superimposed onto NOAA images. The trajectories represent ± 20 days from the image's acquisition time. Crosses plotted on the tracks indicate points within ± 12 hours from the image's acquisition time.





Mutlow, page 42, Figure 1. False colour image produced using brightness temperatures from the ATSR-2 instrument. The image covers a 512 by 1000 km area and was collected on 16 May 1995. The image was obtained from ATSR-2's nadir view, during a day-time pass of the United States Eastern Seaboard, from New York (at the top of the image) to Pamlico Sound, North Carolina (at the bottom of the image). The colour scheme shows hottest areas as black (mostly land) and red, and coolest areas as white (mostly cloud) and blue. Significantly warmer than the surrounding water, the Gulf Stream is clearly delineated. The range of temperatures shown in the image is approximately 280 Kelvin to 300 Kelvin.



Mutlow, page 42, Figure 2. Composite of the 10 arc minute spatially averaged SST data for August 1997 from the ATSR-2 instrument (K). The data clearly shows the warming of the Pacific due to the El Niño, and prominent Somali upwellings and the Gulf Stream.

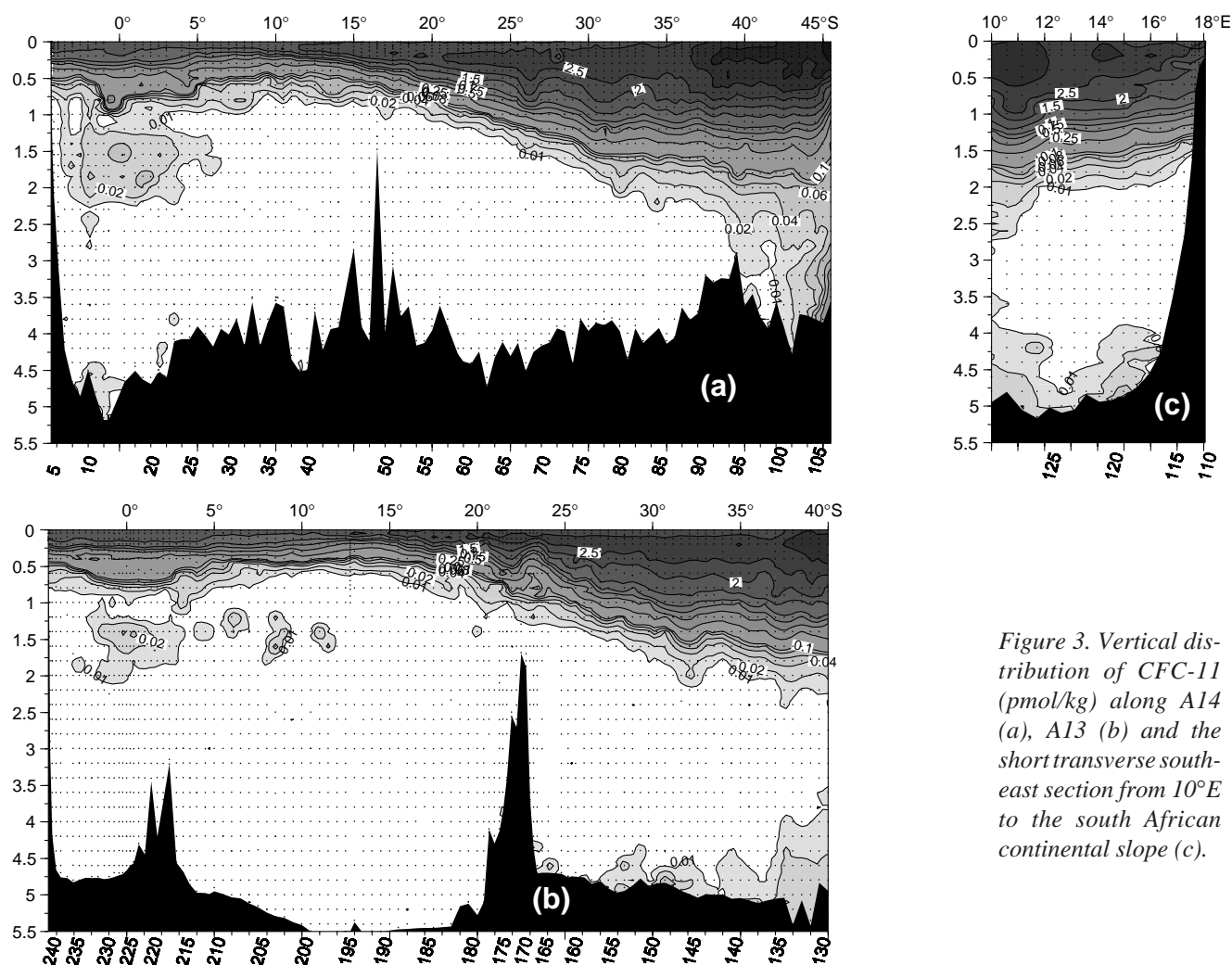


Figure 3. Vertical distribution of CFC-11 (pmol/kg) along A14 (a), A13 (b) and the short transverse south-east section from 10°E to the south African continental slope (c).

recent as it has been found almost at the detection limit (0.01 pmol/kg) in early 1991 along 19°S in the Brazil Basin (Wallace et al., 1994).

At the upper and intermediate levels, the major fronts can be identified in relation to the southern region ventilated by the Subantarctic/Subtropical Mode Waters and the Antarctic Intermediate Water (AAIW), and the low CFC equatorial and tropical domains. In particular on the southern end part of A17, new AAIW (probably deriving from SAMW) is recognised ~45°S by a CFC-high tongue spreading and deepening (800 db) northward as far as 35°–31°S where it turns eastward out of the confluence region into the Subtropical gyre. About the Warm Water Path, two Agulhas rings with different feature were seen in the subtropical region on A14. The first was found at 26°S around 600 db and the second at 32°S, wider and at slightly deeper depths.

Acknowledgements

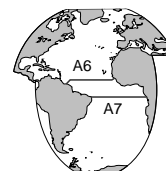
We acknowledge Eric Guilyardi for his help in processing the data and drawing the figures. This work was supported by IFREMER, CNRS and INSU.

References

- Friedrichs, M. A. M., and M. M. Hall (1993) Deep circulation in the tropical North Atlantic. *J. Mar. Res.*, 51, 697–736.
- Mercier, H. and P. Morin, 1997: Hydrography of the Romanche and the Chain Fractures Zones. *J. Geophys. Res.*, 102, 10373–10389.
- Messias, M-J, C. Andrié, L. Memery and H. Mercier, 1998: Tracing the North Atlantic Deep Water through the Romanche and Chain fracture zones using chlorofluoromethanes. Submitted to *Deep-Sea Research*.
- Smythe-Wright, D., and S. Boswell, 1995: Is the Deep Water Circulation in the Argentine Going Round the Wrong Way? *International WOCE Newsletter*, 21, 33–34.
- Tsuchiya M., L. D. Talley, and M. S. McCartney, 1994: Water-mass distributions in the western South Atlantic: A section from South Georgia Island (54°S) northward across the equator. *J. Mar. Res.*, 52, 55–81.
- Wallace, D. W. R., P. Beinig, and A. Putzka, 1994: Carbon tetrachloride and chlorofluorocarbons in the South Atlantic Ocean, 190°S. *J. Geophys. Res.*, 99, 7803–7819.
- Warren, B. A., and K. G. Speer, 1991: Deep circulation in the eastern South Atlantic Ocean. *Deep-Sea Res.*, 38, Suppl. 1, S281–S322.
- Weiss, R. F., J. L. Bullister, R. H. Gammon, and W. J. Warner, 1985: Atmospheric chlorofluoromethanes in the deep equatorial Atlantic. *Nature*, 314, 608–610.

Heat Flux Estimates Across A6 and A7 WOCE Sections

F. Marin, LPO (CNRS-IFREMER-UBO), Brest, France; Y. Gouriou and B. Bourlès, ORSTOM, Brest, France. fmarin@ifremer.fr



One of the main goals of the WOCE programme is to assess meridional heat fluxes across various hydrographic sections in the three oceans. Indeed, except in the North Atlantic Ocean, where numerous convergent estimates exist, the magnitude and sometimes even the sign of oceanic heat fluxes may appear questionable, and the seasonal variability of this heat transport has yet to be documented. Table 1 yields some estimates of meridional heat transports, based on hydrological transects, for the Atlantic Ocean between 30°S and 30°N: heat transport is northward at all latitudes, and seems to increase from 30°S to 11°N, particularly in the tropical region, where the heat gain by the ocean is the strongest.

To study the contribution of the equatorial area in this heat gain by the ocean, the A7 and A6 WOCE sections were carried out aboard N/O l'Atalante as part of the CITHER project: A7 took place in January 1993 along 4.5°S, A6 in February–March 1993 along 7.5°N. Fig. 1 shows the location of the 175 considered hydrographic stations; station spacing is about 70 km in the midocean, but shorter near the coasts to follow the bathymetric features. A RDI 75 kHz ship-mounted ADCP provided absolute velocities from 28 metres to about 700 metres depth. Heat flux estimates are first presented for both A6 and A7 sections. Then, a study of the heat flux variability across the 7.5°N section is presented, based on data collected during the two ETAMBOT (Etude du Transport Atlantique Meridien de Bord Ouestequatorial) cruises; the latter have repeated the WOCE A6 section west of 35°W, in September 1995 and April 1996.

Method and results

Following Hall and Bryden (1982), the meridional heat flux is split into four components:

$$H = H_{WBC} + H_{Ek} + H_B + H_b$$

H_{WBC} is the contribution of the shallow-western boundary current on the continental shelf, down to 200 metres; H_{Ek} is the wind-generated Ekman transport across the section; H_B is the vertically-averaged barotropic component and H_b the baroclinic geostrophic part:

$$H_b = \rho \cdot C_p \cdot \int \theta'(x) \cdot v'(x) dx$$

where ρ is the density of water, C_p the specific heat at constant pressure, θ the potential temperature, v the geostrophic velocity, and where primes refer to baroclinic

quantities, i.e. the difference between in-situ values and their vertical average. This method assumes that there is no volume transport across the whole section, that the vertically-averaged (or barotropic) temperature $\bar{\theta}$ is constant along the section (equal to 4.54°C and 4.23°C respectively for 7.5°N and 4.5°S sections) and that absolute currents are only composed of geostrophic and Ekman currents. Under these conditions, we do not need to determine a reference velocity for geostrophic currents, and the barotropic heat transport becomes:

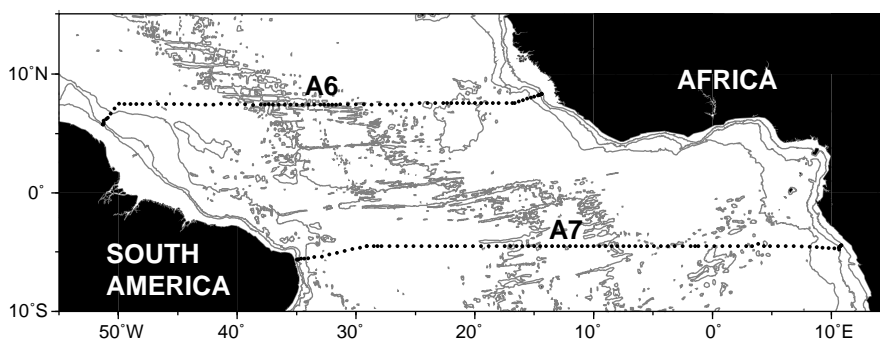


Figure 1. Location of the 175 hydrographic stations of interest along 7.5°N and 4.5°S in the Atlantic. Isobaths of 200, 2000 and 4000 metres are shown.

$$H_B = -\rho \cdot C_p \cdot \bar{\theta} \left(\int T_{Ek}(x) dx + T_{WBC} \right)$$

Unlike the 4.5°S section where the 200 m isobath is near the coast, H_{WBC} can not be neglected for the 7.5°N section: there, the continental shelf extends 170 km off French Guiana. No estimate of this transport is available for the period of the cruise. Bourlès et al. (1998) collected various estimates of this transport between 1989 and 1996, and found a mean volume transport of 3.8 ± 1.2 Sv, with no clear seasonal cycle. Such an estimate leads, for a mean temperature of 26.8°C, to a heat transport of 0.42 ± 0.13 PW. These values are retained in this paper.

Two methods for the computation of Ekman heat transports are compared in this note:

- first, the traditional approach based on climatological wind stresses is used; because ship measured winds are not available for the cruise, we have used Servain et al. (1996)'s monthly pseudo-windstresses linearly interpolated at the date and the location of the stations. Wind stresses τ are computed using the bulk formula:

$$\tau = \rho_a \cdot C_D \cdot |u| \cdot u$$

where $\rho_a = 1.25 \text{ kg} \cdot \text{m}^{-3}$ is the air density and $C_D = 1.15 \cdot 10^{-4}$ the drag coefficient. Following the Ekman theory, the mass transport T_{Ek} and the heat transport H_{Ek} will then be expressed as:

$$T_{Ek} = \int v_{Ek} \cdot dx; H_{Ek} = \rho C_p \int (\bar{\theta}_{Ek}(x) \cdot v_{Ek}(x) dx);$$

$$v_{Ek}(x) = \tau_y(x) / (\rho \cdot f)$$

where f is the Coriolis parameter, the cross-section component of wind and the Ekman layer temperature that will be replaced in our computation by the sea-surface temperature. The following Ekman volume and heat transports are obtained: 11.5 Sv and 1.23 PW across 7.5°N, -9.3 Sv and -1.01 PW across 4.5°S. The western parts of each section are the major contributors for both estimates. To evaluate the error bars on these estimates, Ekman transports are computed for December, January and February; we get the following average estimates: 11.7±1.0 Sv and 1.28±0.08 PW for 7.5°N, -13.7±3.2 Sv and -1.37±0.20 PW for 4.5°S. Thus, whereas estimates for the northern section prove to be constant for the period of the cruise, Ekman transports across 4.5°S change significantly when considering the average for the three months, because the Ekman transports are particularly weak in January. The problem of knowing whether the two sections may be considered as synoptic is already raised.

- secondly, following Chereskin and Roemmich (1991) and Wijffels et al. (1992), we assume that the Shipborne ADCP (S-ADCP) absolute velocities are only composed of the geostrophic and Ekman currents; ageostrophic components, but the Ekman velocity, are then neglected. The problem is then to choose a reference level where ageostrophic velocities cancel, i.e. where S-ADCP and geostrophic velocities merge. For 7.5°N, this level is chosen at 600 metres, and Fig. 2 presents the profiles of ageostrophic, geostrophic and ADCP transports versus depth; a slab layer extrapolation is applied for S-ADCP currents at the surface. The ageostrophic transport appears

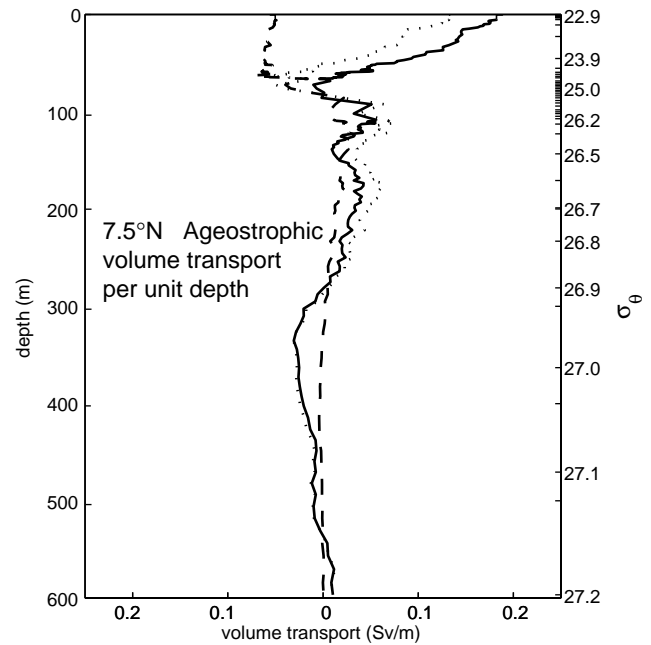


Figure 2. S-ADCP (dotted), geostrophic (dashed) and ageostrophic (solid line) transport per unit depth across 7.5°N (in Sv/m). Geostrophic currents are chosen to merge with S-ADCP currents on average on the depth range 500–600 metres.

to vanish at 65–80 m, for potential density between 24.5 and 25.3, precisely in the core of the thermocline, even though a weaker ageostrophic signal persists deeper; Ekman dynamics is likely to govern this surface-trapped transport of 7.7 Sv and 0.68 PW. If we choose a linear extrapolation at the surface instead of a slab layer, these estimates

become 8.7 Sv and 0.77 PW. We will arbitrarily synthesise these results and give the following estimates of Ekman transports across 7.5°N: 8.2±0.5 Sv and 0.72±0.05 PW. The case of the 4.5°S section is more complex: the ageostrophic velocities no longer vanish at the core of the thermocline. The 4.5°S section is indeed at the location of the South Equatorial UnderCurrent (SEUC), with speeds greater than 40 cm/s in its core at a depth of about 180 m: the assumption that ageostrophic velocities other than Ekman ones are negligible is all the more questionable here, as Coriolis terms are of less importance at 4.5°S. Particularly, the thermocline does no longer play the role of a barrier between the strong wind-generated signal above and the weaker ageostrophic one beneath. Consequently, besides the level of cancellation of ageostrophic velocities, the depth of the Ekman layer must be specified arbitrarily; we choose it at the core of the thermocline, as for 7.5°N, and find Ekman transports equal to -4.0±1.7 Sv and -0.53±0.20 PW, with error bars representing the difference between a slab layer and a linear extrapolation at the surface.

The two methods used to compute the Ekman transports give divergent results: S-ADCP deduced wind-generated velocities lead to weaker estimates

Table 1. Estimates of meridional heat fluxes across various transatlantic sections between 30°S and 30°N. Positive values represent northward heat transports. Error bars account for uncertainties on the method of computation and/or on seasonal variabilities.

References	Latitude	Heat Flux (PW)
Molinari et al. (1990)	26.5°N	1.21±0.34
Johns et al. (1997)	26.5°N	1.44±0.33
Hall and Bryden (1982)	25°N	1.2±0.3
Roemmich et al. (1984)	24.5°N	1.2±0.2
Klein et al. (1995)	14.5°N	1.22 (annual) 1.37±0.42 (February)
Friedrichs and Hall (1995)	11°N	1.1 (annual) 0.30±0.18 (May)
Klein et al. (1995)	8°N	1.18 (annual) 1.69±0.52 (May)
Speer et al. (1994)	11°S	0.6±0.17
Holfort (1994)	11°S	0.7±0.25
Holfort (1994)	19°S	0.69±0.25
Holfort (1994)	23°S	0.36±0.25
Holfort (1994)	30°S	0.40±0.25

Table 2. Volume and heat fluxes across A6 and A7 sections for various Ekman transport computations: a - with Servain et al. (1996)'s pseudo-windstresses interpolated at the location and the date of CTD stations. b - with wind-generated velocities deduced from the comparison of geostrophic and S-ADCP currents. c - with Servain et al. (1996)'s pseudo-windstresses interpolated at the location of CTD stations, averaged for January-February-March.

Section	H_{WBC}	H_{Ek}	H_b	H_B	H
A6 a (Sv)	3.8 ± 1.2	11.5 ± 0.5	-	-15.3 ± 1.7	-
(PW)	0.42 ± 0.13	1.23 ± 0.05	-0.13	-0.29 ± 0.04	1.23 ± 0.14
A6 b (Sv)	3.8 ± 1.2	8.2 ± 0.5	-	-12.0 ± 1.7	-
(PW)	0.42 ± 0.13	0.86 ± 0.05	-0.13	-0.21 ± 0.03	0.94 ± 0.16
A6 c (Sv)	3.8 ± 1.2	11.7 ± 1.0	-	-15.5 ± 2.2	-
(PW)	0.42 ± 0.13	1.28 ± 0.08	-0.13	-0.29 ± 0.04	1.28 ± 0.17
A7 a (Sv)	-	-9.3 ± 1.2	-	9.3 ± 1.2	-
(PW)	-	-1.01 ± 0.14	2.13	0.16 ± 0.02	1.28 ± 0.12
A7 b (Sv)	-	-4.0 ± 1.7	-	4.0 ± 1.7	-
(PW)	-	-0.53 ± 0.20	2.13	0.07 ± 0.03	1.67 ± 0.14
A7 c (Sv)	-	-13.7 ± 3.2	-	13.7 ± 3.2	-
(PW)	-	-1.37 ± 0.20	2.13	0.24 ± 0.06	1.00 ± 0.04

for both 7.5°N and 4.5°S. For 7.5°N, the underestimation may be the consequence of the large mesoscale variability in this region (Richardson et al., 1994). The problem seems greater for the 4.5°S section, because, besides the large monthly variability in climatological data, the assumption that ageostrophic velocities, except Ekman ones, are negligible seems no longer valid there.

The baroclinic heat fluxes are easier to estimate, because they are directly computed from hydrological data. These fluxes occur essentially in the upper ocean, where both temperatures and velocities take their greater values. We find the following estimates: -0.13PW for the 7.5°N section, and 2.13 PW across 4.5°S. It must be noted that the estimate for 7.5°N is subject to an important error bar, given the strikingly variable character of this flux near the western boundary of the basin (Fig. 3).

The last component to evaluate is the barotropic contribution, whose computation is based on the assumption of no volume flux across a zonal transect. For each section, the estimates are computed separately from the two different values obtained for the Ekman volume transport. The results are reported on Table 2. Heat flux estimates are very sensitive to the computation method of Ekman transports: the S-ADCP method gives an amazing heat loss from South to North, which can not be explained with traditional estimates for air-sea fluxes. Results with Servain et al. (1996)'s pseudo-windstresses lead to a net heat gain of approximately 0.3 PW within error bars if we consider the winds averaged on the trimester of the cruise. We prefer to retain these values (1.28 ± 0.17 PW across 7.5°N and 1.00 ± 0.14 PW across 4.5°S) as seasonally significant, even though we have in mind that a huge month-to-month variability exists across the southern transect.

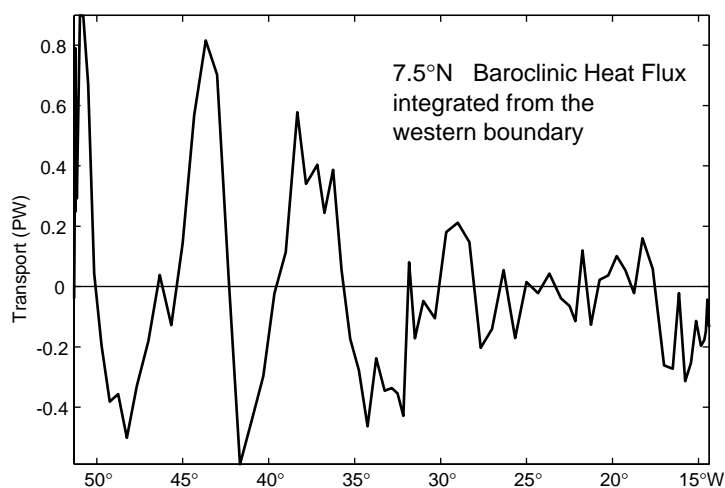


Figure 3. Baroclinic heat flux, integrated from the western boundary, across 7.5°N. The unit is PW.

Seasonal variability across 7.5°N

ETAMBOT 1 and 2 cruises repeat the 7.5°N section west of 35°W, in a region that largely contributes to the heat fluxes across 7.5°N; if we complete the 7.5°N section east of 35°W with Levitus (1982) climatological data, we can estimate heat flux variability across 7.5°N and compare them with the numerical model results – Sarmiento (1986), Philander and Pacanowski (1986), Böning and Hermann (1994). The estimates for each component of the heat fluxes are summarised in Table 3; Ekman transports are computed here from Servain et al. (1996)'s climatological pseudo-windstresses, for the month of the campaign. Of particular interest are the important weakening of Ekman transports in April, that causes a sensitive decreasing of total heat flux across the section, and the non-negligible seasonal variability on baroclinic heat fluxes: in September, we

must estimate the latter flux halfway between 0.30 PW for July–August–September and -0.41 PW for October–November–December. Fig. 4 reproduces the seasonal variability seen by different models; our estimates, with their error bars, are also represented. Within error bars, the agreement between our direct computations and the results of numerical models is striking: the seasonal cycle is reproduced, but our data do not allow to conclude whether the heat flux across 7.5°N can take negative values or not.

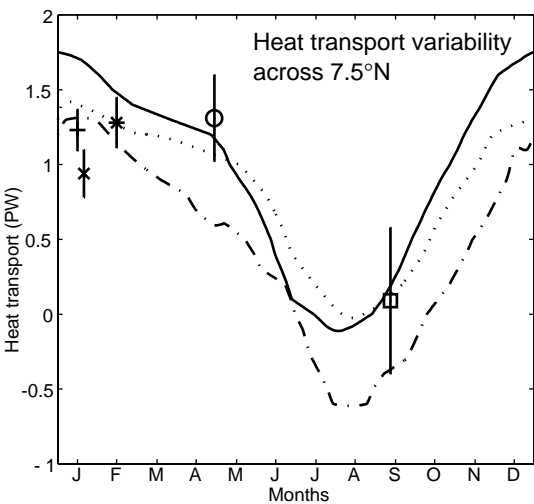


Figure 4. The seasonal variability of the meridional heat flux across 7.5°N, as seen by numerical models [Sarmiento, 1986 (solid line); Philander and Pacanowski, 1986 (dotted-dashed); Böning and Herrmann, 1994 (dotted line)] and our estimates - where vertical bars refer to error bars - from CITHER 1 [windstress for the campaign (cross), ageostrophic method (x) and trimestrially-averaged windstress (star)], ETAMBOT 1 (square) and ETAMBOT 2 (circle) data. The unit is PW.

Acknowledgements

This investigation was supported by the Programme National d'Etude de la Dynamique du Climat (PNEDC) and its WOCE/France subprogramme.

References

Böning, C. W., and P. Hermann, 1994: Annual cycle of poleward heat transport in the ocean: results from High-Resolution modeling of the North Equatorial Atlantic. *J. Phys. Oceanogr.*, 24, 91–107.

Bourlès, B., Y. Gouriou, R. Chuchla, and C. Colin, 1998: On the northward warm water flow over the continental shelf of French Guiana. Submitted to *J. Geophys. Res.*

Chereskin, T. K., and D. Roemmich, 1991: A comparison of measured and wind-driven Ekman transport at 11°N in the Atlantic Ocean. *J. Phys. Oceanogr.*, 21, 869–878.

Table 3. Heat flux components across 7.5°N from ETAMBOT campaigns. Sections are completed east of 35°W with Levitus (1994)'s data. Error bars refer to the seasonal variability.

	ETAMBOT 1 (September 1995)		ETAMBOT 2 (April 1996)	
	Western half	Eastern half	Western half	Eastern half
H_{WBC}	0.45		0.42±0.13	
H_{Ek}	0.10±0.07	-0.10±0.07	0.97±0.15	0.28±0.05
H_b	-0.23	-0.05±0.35	0.06	-0.13
H_B	-0.08±0.08		-0.29±0.21	
H	0.09±0.49		1.31±0.29	

Hall, M. M., and H. L. Bryden, 1982: Direct estimate and mechanism of ocean heat transport. *Deep-Sea Res.*, 29, 3A, 339–359.

Holfort, J., 1994: Grossräumige Zirkulation und meridionale Transporte im Südatlantik. Ph.D. thesis, 118 pp., Ber. Inst. Meeresk. Kiel.

Klein, B., R. L. Molinari, T. J. Müller, and G. Siedler, 1995. A transatlantic section at 14.5°N: meridional volume and heat fluxes. *J. Marine Res.*, 53, 929–957.

Levitus, S., 1982: Climatological atlas of the world ocean, NOAA Prof. Paper 13, U.S. Govt. Printing Office, 173 pp.

Philander, S. G. H., and R. C. Pacanowski, 1986. The mass and heat budget in a model of the tropical Atlantic Ocean. *J. Geophys. Res.*, 12, 14212–14220.

Richardson, P. L., G. E. Hufford, R. Limeburner, and W. S. Brown, 1994: N.B.C retroflection eddies. *J. Geophys. Res.*, 99, 5081–5093.

Sarmiento, J. L., 1986. On the North and Tropical Atlantic heat balance. *J. Geophys. Res.*, 11, 677–689.

Servain, J., J. N. Stricherz, and D. M. Legler, 1996: TOGA Pseudo-wind stress Atlas 1985–1994 - volume 1: Tropical Atlantic.

Wijffels, S. E., E. Firing, and H. L. Bryden, 1992: Direct observations of the Ekman balance at 10°N in the Pacific. *J. Phys. Oceanogr.*, 24, 1666–1679.

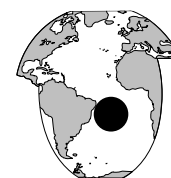
WOCE/CLIVAR Workshop on Ocean Modelling for Climate Studies, NCAR, Boulder, CO, USA, 10–13 August 1998

The workshop aims to bring together ocean and climate modellers and observationalists, in order to understand how current and future observational datasets can be used to guide the development of ocean models, particularly those used to study climate. The goals are: (1) to develop an understanding and consensus in the modelling community of how well different aspects of ocean dynamics need to be represented in order to achieve realistic simulations of the ocean's role in climate variability on decadal time scales, and (2) to develop a consensus of benchmark data sets for quantitative model tests that could lead to more co-ordination, transparency and feedback between individual model development efforts.

The group of invited participants is expected to produce a research plan directed towards clarifying the role of certain small-scale ocean processes and their numerical representation in simulations of climate variability.

Scientific Committee: C. Böning (chair), M. England, P. Gent, D. Haidvogel, W. Large, L. Talley, E. Tziperman, D. Webb, J. Willebrand, R. Wood, C. Wunsch.

Lagrangian and Infrared Observations of Surface Currents in the Brazil-Malvinas Confluence Zone, 1993–1994



Ronald Buss de Souza and Ian S. Robinson, Department of Oceanography, Southampton Oceanography Centre, Southampton, UK. rbds@soton.ac.uk

The seasonal variability and characteristics of the Brazil-Malvinas Confluence zone (BMC), in the Southwestern Atlantic Ocean, have been studied since Deacon (1933). More recent publications include Goni et al. (1996) and Seeliger et al. (1997). One of the more remarkable features of the BMC region evident from these works is that the position of the confluence oscillates seasonally, with the Brazil Current (BC) reaching the southernmost limits in the Austral Summer, and the Malvinas/Falkland Current (MC) achieving its northernmost limits in the wintertime.

Reasons for the oscillation of the BMC front through the year are still unknown (Peterson and Stramma, 1991). Speculations include relations with the subtropical atmospheric pressure system, the South Equatorial Current (SEC), and the wind stress curl. Garzoli and Garraffo (1989) also attributed the spatial variation of the BMC to the variability of the winds and of the SEC which feeds the BC. According to Olson et al. (1988), the local wind may also play a role in the location where BC separates from the coast, but it is unlikely that it can be uniquely responsible for such a process. Another alternative proposed by these authors is that variation in the MC is forced by variations in the Antarctic Circumpolar Current (ACC) system. Pressure changes in the Subantarctic Front, where MC is fed by a branch of the ACC, could reach the BMC region by topographic Kelvin waves. Wind induced advective changes in the MC could also link the Antarctic sector with the BMC region.

The position of the BMC is believed to range from 36°S to 39°S in mean (Reid et al., 1977). The position in which the BC reverses its direction, however, is further South between 40°S and 46°S. After meeting the MC in the BMC region, the BC separates from the shelf break and penetrates the Atlantic Ocean interior, forming the South Atlantic Current or Brazil Current Extension (SAC), in a series of large amplitude meanders. Legeckis and Gordon (1982) found the variable limit of 38°S to 46°S as the maximum latitude of warm water related to the BC. The variability of this limit is also accompanied by intermittent formation of warm-core anticyclonic eddies.

Working with AVHRR data collected between July 1984 and June 1987, Olson et al. (1988) established the statistical characteristics of the region of separation from the continental shelf for both the BC and MC. They also drew attention to the fact that the BMC region is particularly suited for study by remote sensing techniques, pointing out two

major reasons to support this: first, the complex mesoscale variability of the region needs synoptic monitoring provided by satellite imagery; and second, the processes occurring in the sea surface present strong thermal gradients.

Lack of in situ surveys and long-term data collection programmes are generally accepted as causes of the poor understanding of oceanographic processes occurring in the Southwestern Atlantic Ocean in comparison to other parts of the World Ocean. Remaining questions concerning the physical oceanography of the Southwestern Atlantic Ocean include the driving mechanisms of a possible increase of the BC transport southwards (Garfield, 1990), the characteristics of the SAC during its formation, the influence of the topography on the BC, MC and SAC, and even the rate of formation and configuration of meso-scale eddies formed in the BMC region.

During the experimental phase of the COROAS (Oceanic Circulation in the Western Region of the South Atlantic) project (1993–1995), the Brazilian contribution to WOCE, a temporal series of full-resolution AVHRR imagery was collected at the same time as 15 WOCE standard, Low Cost Drifters (LCDs) were deployed at the BC, in a region next to São Paulo State, inshore Brazilian Continental Waters (Campos et al., 1996a). As 9 drifters quit the COROAS area of study and entered the BMC, their tracks and sea surface temperature (SST) time series will be used here to describe the velocities, kinetic energies, temperature statistics and oscillations for two of the currents occurring in the BMC region: BC and SAC. A tenth LCD deployed at the BC returned northwards when reaching the BMC, in a coastal branch of MC called here Brazilian Coastal Current (BCC). This current will be described as well. A combination of buoy trajectories and satellite imagery will be used to describe eddy characteristics in the study area, topographic effects in the BC at about 31°S and the penetration of BCC as far north as 23°S. Spectral analysis of the buoy instantaneous velocities and SST for

Table 1. Lifetime and number of observations (N) for the LCDs

buoy	start	finish	lifetime (days)	N
a	24 March 1993	15 October 1993	204.29	298
b	12 March 1993	26 March 1993	14.27	21
c	23 March 1993	11 February 1994	324.23	1350
d	1 September 1993	15 April 1994	226.03	747
e	13 December 1993	16 April 1994	123.11	371
f	12 February 1994	1 March 1994	17.03	65
g	13 February 1994	5 July 1994	141.96	513
h	5 February 1994	5 July 1994	150.05	474
i	1 February 1994	5 July 1994	153.99	576
j	4 February 1994	5 July 1994	151.03	585

BC, BCC and SAC will be utilised to estimate the oscillations present in these currents between 1993–94.

Instruments and methods

The drifters used here were built at INPE (National Institute for Space Research, Brazil) for the COROAS project, following the design proposed by Sybrandy and Niiler (1991). The LCDs are designed to follow the surface waters, having a holey-sock drogue centred at 15 m of water. Positions and SST (12 cm beneath the water line, 0.12°C of accuracy) measured by the buoys were transmitted to INPE through the ARGOS system. Consistency analysis and filtering were applied to the series in order to remove high frequency spikes. None of the LCDs used here lost the drogue during its transmission time. Overall lifetimes for the LCDs varied from 2 months to 11 months. LCD deployments in the Brazilian Continental waters are described by Stevenson (1996). Lifetimes for the buoys after reaching the BMC region and the number of observations made by each individual buoy are listed in Table 1. The drifters were at the BMC region from March 1993 to July 1994. Processing of the time series was conducted independently for each buoy and for each of BC, SAC and BCC currents. Establishment of the exact location where a buoy exited BC to enter SAC or BCC was based upon the location where the buoy described a major change in the displacement direction, e.g. from SW to SE in the case of SAC and from SW to NW in the case of BCC. Displacement time series were used to compute the mean current (speed and direction). Instantaneous velocities for each buoy and current were used to compute the Mean, Eddy and Total kinetic energies (MKE, EKE and TKE, respectively), and to generate the FFT spectra of the series. Temperature time series were used to produce the basic

statistics and FFT spectra for each of the currents studied here.

Full-resolution (1.1 × 1.1 km) AVHRR images were collected for COROAS at INPE once a day since late 1992. The project was conducted in order to provide for the first time a consistent time series of full-resolution imagery over the Brazilian Continental waters, supporting COROAS objectives off São Paulo coast. As the location of INPE's reception antenna permits the coverage of areas as far south as 42°S, the BMC region is included in the majority of COROAS AVHRR scenes. During the time when the LCDs were in the sea, 82 images were recorded covering the BMC region. Intense cloud coverage in the area, specially during the Winter, made the recording of more images impossible. In this work, AVHRR images (5 channels) were processed at INPE and Southampton Oceanography Centre (SOC) to generate geolocated SST charts.

Results

Overall trajectories described by the LCDs can be seen in Fig. 1. BC is seen meandering parallel to the South American coast. Meanders have typical length of about 200 km. Visual comparison with the topography (not shown) suggests the tendency of the surface waters of BC to follow the isobaths. In the vicinity of 31°S this tendency is very well defined, where surface tracks show a major change in the direction of the BC flow from SW to W, responding to the distribution of the isobaths of 200 m to 3000 m. BCC was sampled by just one LCD, but can be noted flowing north-eastward from 31°S to 24°S. Inshore eddy activity is noted in the vicinity of 25°S. SAC is seen as a meandering zonal current flowing eastward in a band of latitudes which varied on average from 29°S to 40°S. The size of meanders and eddies in this current varied from about 200 km to 500 km, both cyclonical and anticyclonically. Great eddy activity occurs at 37.5°S, 52°W. A similar pattern of eddy activity can be observed in ALACE (1000 m) float tracks in the South Atlantic from 1990 to 1996, presented in the WOCE Subsurface Float Data Assembly Centre WWW site (<http://wfdac.whoi.edu>; R. Davis, SIO). Although this ALACE sampled feature is centred at about 45°S, 43°W, there is a possibility that these features are the same, in this case being homogeneous from surface to 1000 m and oscillating seasonally together with the convergence zone.

Table 2 shows the statistics obtained for BCC, BC and SAC in terms of its velocities, kinetic energies and temperatures during the time of this study. Surface (15 m) speeds in the BC were found to range between 12.2 cm/s to 53.6 cm/s in the SW direction (37.4 on average towards 215.7°), while SAC exhibits velocities from 4.2 cm/s to 16.6 cm/s to the east (9.7 cm/s on average towards 94.7°). Velocity in the BCC was 5.8 cm/s, directed to 14.6°. Eddy kinetic energies were equal to 771 cm² / s² in the BCC, 1294 cm² / s² in the BC and 3268 cm² / s² in the SAC. The temperature averages for both BCC and SAC were more than 4°C cooler than that for BC, showing the influence of subantarctic waters (SAW) in these currents.

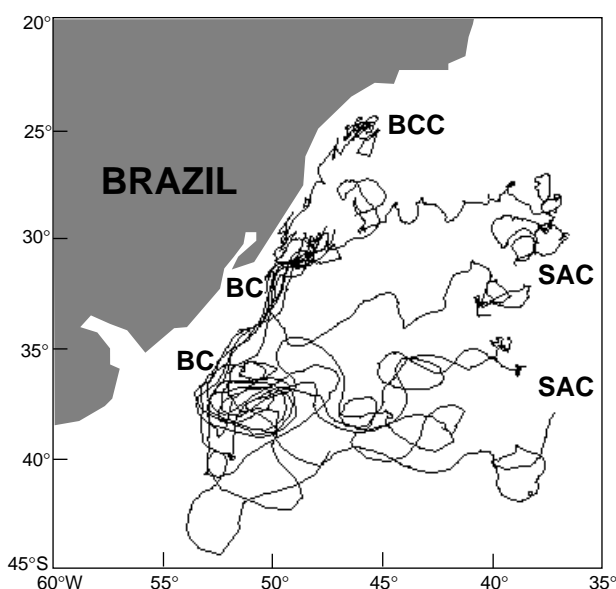


Figure 1. Overall trajectories of the LCDs in the BMC region.

Using tracks of 3 LCDs including the one used here to characterise the BCC, Stevenson and Souza (1994) and Stevenson (1996) described a cyclonic, inshore recirculation scheme of the BC south of 20°S. Velocities for the BC return flow (called here BCC) ranged from 5 cm/s to 17 cm/s. The recirculation periods measured for the BC varied from 115 to 161 days. Those authors also noted that this recirculation mode of the BC can transport coastal waters (CW) mixed with SAW northwards up to the latitudes of the tropical Rio de Janeiro city, near 23°S. Campos et al. (1996a,b) and Silva, Jr., et al. (1996) pointed out the necessity for further work to establish the long-term variability of the presence of this intrusion of CW/SAW over the Brazilian continental shelf. Taking into account that the SAW and CW are much more productive than the oligotrophic TW transported by the BC (Seeliger and Odebrecht, 1997), the environmental and economical

aspects of the domination of the inner Brazilian shelf by waters with subantarctic and coastal origin needs urgently to be determined.

Schafer and Krauss (1995) presented statistics for the major ocean currents in the Southwestern Atlantic and in the ACC. They deployed more than 130 satellite-tracked drifting buoys in the South Atlantic between 1990 and 1993, the majority of them drogued at 100 m depth. The BC mean velocity was found to be weak between 7°S and 20°S (4 cm/s), increasing to 40 cm/s in the vicinity of the BMC region. The BMC region presented large variability, with zonal and meridional r.m.s. currents of about 40 cm/s. In agreement with this work, SAC was found to be almost zonal, presenting a mean velocity of 12 cm/s. BC shows typical Eddy Kinetic Energy (EKE) varying between $200 - 400 \text{ cm}^2 / \text{s}^2$. EKE values in the BMC region reach $1600 \text{ cm}^2 / \text{s}^2$ decreasing again in the SAC further east.

Piola et al. (1987), Stevenson and Souza (1994) and Stevenson (1996) also presented EKE values for the BC derived from drifting buoy data. While Piola et al. (1987) worked with FGGE buoys, the last authors used the COROAS drifters. As in this paper, EKE dominated the BC flow in both cases, but Stevenson (1996) found these values to range between $1332 \text{ cm}^2 / \text{s}^2$ and $4207 \text{ cm}^2 / \text{s}^2$, while Piola et al. (1987) found $500 \text{ cm}^2 / \text{s}^2$ MKE in the BC was estimated to vary between $114 - 171 \text{ cm}^2 / \text{s}^2$ by Stevenson and Souza (1994), values in good agreement with $200 \text{ cm}^2 / \text{s}^2$ found earlier by Piola et al. (1987), but about 4 times lower than the average BC MKE presented here. Differences between BC speeds measured by all these authors lead to differences in MKE estimates. The data used here represent the southernmost part of the BC flow, which is believed to have its transport increased southwards (Garfield, 1990). Following the results obtained

Table 2. Velocity, Kinetic Energy and Temperature Statistics

<i>(a) Brazilian Coastal Current</i>								
buoy	velocity		kinetic energy				temperature	
	speed (cm/s)	direction (degrees)	MKE (cm^2/s^2)	EKE (cm^2/s^2)	TKE (cm^2/s^2)	%EKE/ TKE	average (°C)	std.dev. (°C)
a	5.8	14.6	17	771	788	97.9	19.82	1.43
<i>(b) Brazil Current</i>								
buoy	velocity		kinetic energy				temperature	
	speed (cm/s)	direction (degrees)	MKE (cm^2/s^2)	EKE (cm^2/s^2)	TKE (cm^2/s^2)	%EKE/ TKE	average (°C)	std.dev. (°C)
a	12.2	252.0	75	1080	1155	93.5	24.17	0.96
b	53.6	212.1	1436	3576	5012	71.3	24.99	0.73
c	34.0	181.7	577	371	948	39.1	26.27	0.13
d	12.8	237.1	82	901	983	91.6	19.17	0.82
e	47.4	214.4	1121	899	2021	44.5	23.52	0.76
f	36.7	212.1	674	705	1379	51.1	24.52	0.43
g	31.6	205.3	499	1009	1508	66.9	23.85	0.72
h	49.2	212.7	1209	1530	2739	55.8	23.97	0.86
i	46.3	214.4	1072	2132	3204	66.5	24.56	0.66
j	50.3	215.3	1265	743	2008	37.0	24.00	0.99
average	37.4	215.7	801	1294	2097	61.7	23.90	0.71
std.dev.	15.0	18.5	490	937	1266	20.0	1.83	0.26
<i>(c) South Atlantic Current</i>								
buoy	velocity		kinetic energy				temperature	
	speed (cm/s)	direction (degrees)	MKE (cm^2/s^2)	EKE (cm^2/s^2)	TKE (cm^2/s^2)	%EKE/ TKE	average (°C)	std.dev. (°C)
c	4.2	123.0	9	1769	1778	99.5	22.56	1.61
d	6.7	112.6	23	2509	2532	99.1	21.69	1.21
e	16.6	74.6	138	3413	3551	96.1	17.66	1.32
g	16.3	69.6	132	5769	5901	97.8	18.61	1.60
h	4.2	111.2	9	2312	2321	99.6	19.08	3.19
i	7.1	88.1	25	3876	3901	99.3	18.75	2.51
j	12.5	83.5	78	3225	3304	97.6	18.61	2.13
average	9.7	94.7	59	3268	3327	98.4	19.57	1.94
std.dev.	5.4	20.8	57	1315	1357	1.3	1.82	0.71

by Schafer and Krauss (1995), BC velocity can also increase southwards, which explains why MKE values estimated here are higher than previous estimates.

FFT spectra of LCDs instantaneous (zonal and meridional) velocities and temperature time series for the BC, SAC and BCC present a consistent peak at around 25 days. Other peaks were found around 10–12 days, 6 days and 4.5 to 5 days. Stech and Lorenzzetti (1992), working with atmospheric pressure data collected between 1980 and 1985, found dominant peaks of 11 days and 6.5 days in wind spectra. By analysing also GEOS infrared imagery, those authors remark that the period of 6.5 days is caused by the passage of frontal atmospheric systems in the South Brazilian Bight (SBB), North of the BMC region. Tide gauge sea level data collected at Paranaguá (~25.8°S, 48.5°W) presented a strong oscillation at 7 days, the same frequency band observed for the wind data. Stech and Lorenzzetti (1992) concluded that the passage of frontal atmospheric systems is one of the major low-frequency forcing mechanisms of the SBB during the wintertime.

Analysis of the full-resolution AVHRR imagery shows the seasonal oscillation of the Subtropical Front and intense eddy generation on the SAC. In addition, the coastal branch of MC (BCC) is seen to be present in inshore Brazilian waters during June to October 1993, and in June–July 1994. Temperatures in BCC (as retrieved from NOAA algorithms) varied between 15–17°C. The MC core during the winter was found to be as cool as 7°C, whereas BC core during the summertime can be warmer than 27°C. Superimposition of buoy tracks onto AVHRR images (trajectories of 40 days centred at the image's acquisition time) show that LCD tracks generally followed regions of current shear between BC and BCC, and between BC and MC (in the SAC). Examples of this superimposition (Fig. 2, page 25) suggest also that major thermal signatures in the BMC region persist in the area for time periods longer than a month.

Conclusions

The COROAS drifting programme has provided the first opportunity for a Lagrangian description of the Brazilian Continental waters. In this paper we characterise three of the major currents occurring at the BMC region, two of them occupying the Brazilian waters. SAC is characterised as a system of currents moving eastward. FFT energy peaks retrieved from buoy data show correspondence with sea level and wind data peaks obtained by Stech and Lorenzzetti (1992). Temperatures in both SAC and BCC indicate the presence of SAW in these currents. Satellite images taken for 1993 and 1994 show that the presence of SAW carried by BCC over the Brazilian Continental Shelf is found during the winter. Thermal signatures at the surface seen by both imagery and buoys have apparently time scales bigger than a month.

Further work will include the statistical analysis of low-resolution AVHRR and ATSR images for periods near a decade, and the comparison of SST and buoy tracks with TOPEX/POSEIDON Sea Surface Height data.

Acknowledgements

The authors acknowledge M. R. Stevenson, J. A. Lorenzzetti and M. L. Vianna for providing the data and INPE facilities used in the early stages of this work. E. J. D. Campos is acknowledged also for his contribution to Brazilian oceanography through the COROAS project. D. Cromwell and K. Richards made substantial comments which originated this paper. Funding for COROAS was provided by CNPq (91/0542-7), FAPESP (40.3007/91.7) and SeCIRM. The first author is funded by CNPq (201146-95.9).

References

- Campos, E. J. D., Y. Ikeda, B. M. Castro, S. A. Gaeta, J. A. Lorenzzetti, and M. Stevenson, 1996a: Experiment studies circulation in the Western South Atlantic. *EOS Transactions Am. Geophys. Union*, 77(27):253,259.
- Campos, E. J. D., J. A. Lorenzzetti, M. R. Stevenson, J. L. Stech, and R. B. Souza, 1996b: Penetration of waters from the Brazil-Malvinas Confluence region along the South American Continental Shelf up to 23°S. *Anais da Academia Brasileira de Ciências*, 68(Supl. 1): 49–58.
- Deacon, G. E. R., 1933: A general account of the hydrology of the South Atlantic Ocean. *Discovery Reports*, 7:171–238.
- Garfield, N., III, 1990: The Brazil Current at subtropical latitudes. Ph.D. Thesis, University of Rhode Island, USA, 122pp.
- Garzoli, S., and Z. Garrafo, 1989: Transports, frontal motions and eddies at the Brazil-Malvinas Currents Confluence. *Deep-Sea Res.*, 36(5):681–703.
- Goni, G., S. Kamholz, S. Garzoli, and D. Olson, 1996: Dynamics of the Brazil-Malvinas Confluence based on inverted echo sounders and altimetry. *J. Geophys. Res.*, 101(C7):16273–16289.
- Legeckis, R., and A. L. Gordon, 1982: Satellite observations of the Brazil and Falkland Currents - 1975 to 1976 and 1978. *Deep-Sea Res.*, 29:375–401.
- Olson, D. B., G. P. Podesta, R. H. Evans, and O. B. Brown, 1988: Temporal variations in the separation of Brazil and Malvinas currents. *Deep-Sea Res.*, 35(12):1971–1990.
- Peterson, R. G., and L. Stramma, 1991: Upper-level circulation in the South Atlantic Ocean. *Progr. in Oceanogr.*, 26:1–73.
- Piola, A. R., A. F. Horacio, and A. A. Bianchi, 1987: Some aspects of the surface circulation south of 20°S revealed by first GARP Global Experiment drifters. *J. Geophys. Res.*, 92(C5):5101–5114.
- Reid, J. L., W. D. Nowlin, Jr., and W. C. Patzert, 1977: On the characteristics and circulation of the Southwestern Atlantic Ocean. *J. Phys. Oceanogr.*, 7:62–91.
- Schafer, H., and W. Krauss, 1995: Eddy statistics in the South Atlantic as derived from drifters drogued at 100 m. *J. Mar. Res.*, 53:403–431.
- Seeliger, U., C. Odebrecht, and J. P. Castello (Eds.), 1997: Subtropical Convergence Environments: The coast and sea in the Southwestern Atlantic. Springer-Verlag, Berlin Heidelberg. 308pp.
- Silva, Jr., C. L., M. Kampel, C. E. S. Araujo, and J. L. Stech, 1996: Observação da penetração do ramo costeiro da Corrente das Malvinas na costa sul-sudeste do Brasil a partir de imagens AVHRR. In: *Proceedings of the 8th Brazilian Symposium on Remote Sensing*. Salvador, Brazil, 14–19 April 1996.
- Stech, J. L., and J. A. Lorenzzetti, 1992: The response of the South Brazil Bight to the passage of wintertime cold fronts. *J. Geophys. Res.*, 97(C6):9507–9520.
- Stevenson, M. R., 1996: Recirculation of the Brazil Current South of 23°S. *WOCE Newsletter* 22: 30–32.
- Stevenson, M. R., and R. B. Souza, 1994: Recirculation of the Brazil Current South of 20°S. In: *Abstracts from the Symposium: The South Atlantic - present and past circulation*. Bremen, Germany, 15–19 August 1994. *Berichte, Fachbereich Geowissenschaften, Universität Bremen*, No. 52, p. 149.
- Sybrandy, A. L., and P. P. Niiler, 1991: The WOCE/TOGA Lagrangian drifter construction manual. *SOI Ref. 91/6*, WOCE Report 63. 58pp.

Water Mass Transformation Theory and the Meridional Overturning Streamfunction

A. J. G. Nurser and R. Marsh, James Rennell Division, Southampton Oceanography Centre, Empress Dock, Southampton SO14 3ZH, UK. g.nurser@soc.soton.ac.uk



The meridional overturning streamfunction zonally integrated along surfaces of constant density has become a standard tool for diagnosing ocean general circulation models (e.g. Döös and Webb, 1994). Current models, however, do not include all the physics correctly (surface fluxes, eddy activity, flow through sills etc.). They therefore tend to drift away from their initial state. Given the finite computer resources available, and indeed the unrealistic nature of the steady state that they would eventually attain, it is often necessary to diagnose these models while they are still evolving.

Here we describe how the link between the meridional overturning streamfunction and watermass transformation breaks down in such evolving models. We then define the ‘watermass transformation streamfunction’ which *does* give the correct transformation.

Partitioning the meridional streamfunction into “transformation” and “unsteady” components

We now relate the meridional streamfunction zonally integrated on density surfaces to the diapycnal flux across a density surface, making plain the intimate link between the two.

Define the meridional streamfunction

$$\begin{aligned}\psi(\Theta, \rho) &= - \int_{\{x: \theta(x) = \Theta\}} \int_{z=z_b}^{z(\rho)} v \, dz \, dl \\ &= - \int_{\{x: \theta(x) = \Theta\}} \int_{\rho}^{\rho_{\max}} h v \cdot d\rho \, dl\end{aligned}\quad (1)$$

to be the total southward transport of waters heavier than ρ across the line of latitude $\theta = \Theta$. Here z_b is the bottom, ρ_{\max} the heaviest (bottom) density at that latitude and $h = -\partial z / \partial \rho$, so $h \delta \rho$ is the thickness of the layer sandwiched between the $\rho + \delta \rho$ and ρ isopycnals. We further write

$$\begin{aligned}V(\Theta, \rho) &= \int_{\{x: \theta(x) > \Theta\}} \int_{z=z_b}^{z(\rho)} dz \, dA \\ &= \int_{\{x: \theta(x) > \Theta\}} \int_{\rho}^{\rho_{\max}} h \, d\rho \, dA\end{aligned}\quad (2)$$

to be the total volume of fluid with density greater than ρ lying north of $\theta = \Theta$. Note that $\psi(\Theta, \rho)$, $V(\Theta, \rho)$ and the other fields defined below *do* depend on time, despite not being written with explicit time dependence.

If we then assume incompressibility it follows that the total diapycnal flow ‘down’ across the ρ isopycnal (from light to heavy) south of $\theta = \Theta$, $G(\Theta, \rho)$, must appear partly as volume inflation, partly as export, according to Speer (1998) (see Fig. 1a)

$$G(\Theta, \rho) = \psi(\Theta, \rho) + \partial V(\Theta, \rho) / \partial t. \quad (3)$$

In the steady state, all of the flow down across the ρ isopycnal must be exported, with $G(\Theta, \rho) = \psi(\Theta, \rho)$, as noted by Speer (1998). However, the point is that when the inflation rate $\partial V(\Theta, \rho) / \partial t \neq 0$, part of the diapycnal flow may be used to inflate the volume under the ρ isopycnal, and the streamfunction does *not* correspond exactly to the

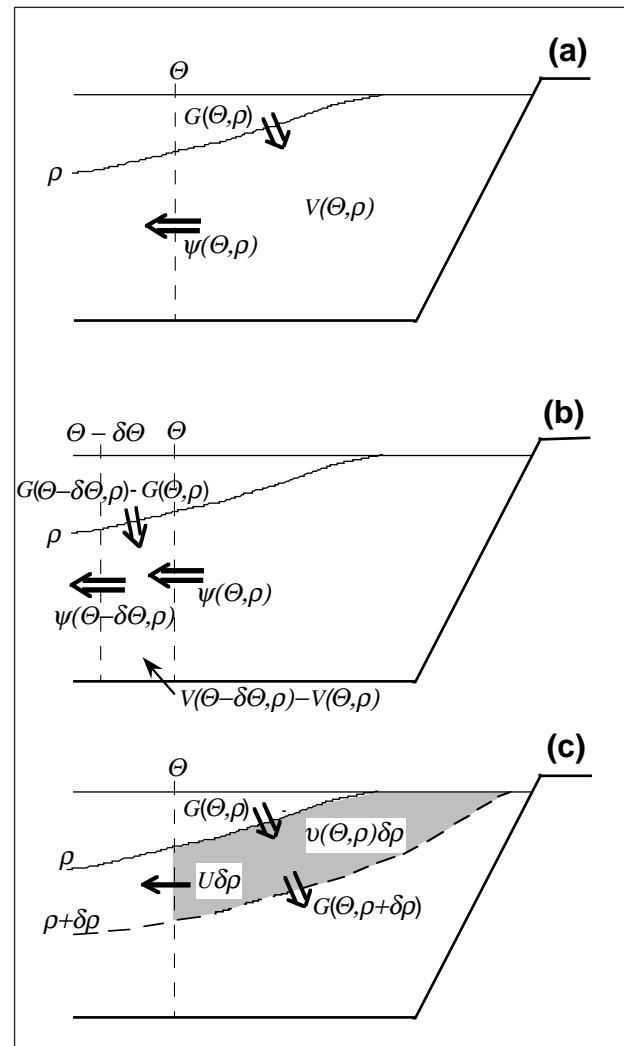


Figure 1. Schematic meridional sections across the Atlantic Ocean: (a) showing the diapycnal flux ‘down’ across the ρ isopycnal north of Θ , $G(\Theta, \rho)$, the volume below the ρ isopycnal, $V(\Theta, \rho)$, and the southwards flow of waters denser than ρ , $\psi(\Theta, \rho)$; (b) showing the relationship between meridional convergences of ψ and G and (c) showing how the convergence of the diapycnal flux is related to the ‘watermass formation’ made up of export ($U \delta \rho$) and changes in the volume $v(\Theta, \rho) \delta \rho$ of the isopycnal layer between the isopycnals ρ and $\rho + \delta \rho$.

diapycnic flow, $G(\Theta, \rho) \neq \psi(\Theta, \rho)$. In particular

$$\frac{\partial G}{\partial \Theta} = \frac{\partial \psi}{\partial \Theta} + \frac{\partial^2 V}{\partial t \partial \Theta} \quad (4)$$

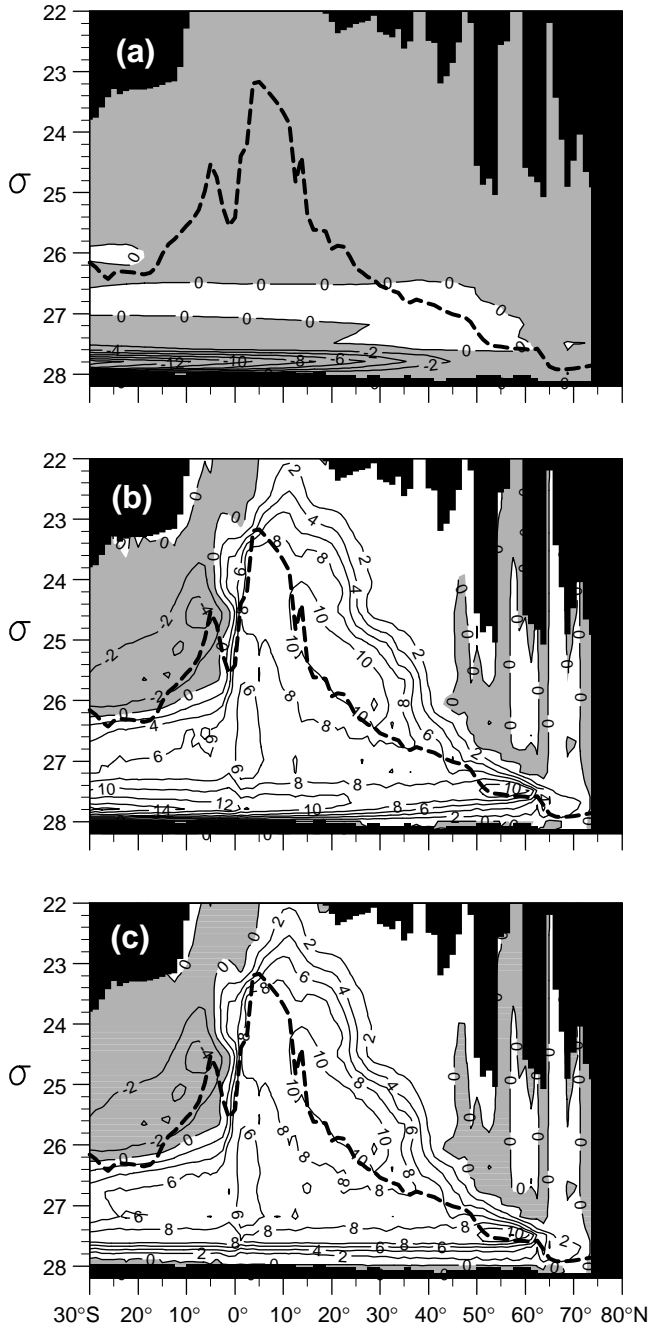


Figure 2. (a) Rate of change of volume of waters below the ρ isopycnal, north of a given latitude $\partial V(\Theta, \rho)/\partial t$ (b) Meridional overturning streamfunction averaged on isopycnals, $\psi(\Theta, \rho)$, and (c) transformation streamfunction, $G(\Theta, \rho)$. All are annual-mean fields from year 30 of a 1.25° by 1.25° global isopycnal model (Marsh et al., 1998). Densities which are never attained at that latitude are masked out in black. The dashed line denotes the greatest density of the mixed-layer at that latitude. Hence waters 'below' the dashed line can only be transformed by diapycnal mixing, not surface fluxes.

Hence (see Fig. 1b) a divergence of fluid denser than ρ ($\partial \psi / \partial \Theta < 0$) need not imply a light-to-heavy transformation at Θ ($\partial G(\Theta, \rho) / \partial \Theta > 0$). Instead, it could simply imply a decrease in the volume of water with density greater than ρ "at" Θ , $\partial^2 V / \partial \Theta \partial t > 0$.

On the other hand, the streamfunction $\psi(\Theta, \rho)$ as defined above has the useful property that it satisfies

$$-(\partial \psi / \partial \rho) = U, \quad (5)$$

where

$$U(\Theta, \rho) \delta \rho = - \int_{\{x: \theta(x) = \Theta\}} h \delta \rho \cdot v \, dl \quad (6)$$

is the southward transport of waters with densities between ρ and $\rho + \delta \rho$. Moreover, $\psi = 0$ at boundaries (ocean surface, coasts) and is only non-zero at the ocean surface if there is depth-integrated flow – i.e., it looks like a streamfunction!

The transformation 'streamfunction' $G(\Theta, \rho)$ of course indeed gives the correct diapycnal flux $\partial G / \partial \Theta$ of waters at latitude Θ . However now (Fig. 1c)

$$-\frac{\partial G}{\partial \rho} = U - \frac{\partial^2 V}{\partial t \partial \rho} = U + \frac{\partial v}{\partial t} \quad (7)$$

(writing $v = -\partial V / \partial \rho$, so that $v(\Theta, \rho) \cdot \delta \rho$ is the volume of water with density between ρ and $\rho + \delta \rho$ north of Θ). Thus $-\partial G / \partial \rho$ now includes the rate of inflation of the layer with density between ρ and $\rho + \delta \rho$ north of Θ , together with the southward export across the latitude Θ . Walin (1982) termed this sum the water mass formation rate M . Furthermore, of course, $G(\Theta, \rho)$ will not in general be zero at the southern boundary of a closed basin, if the volume below the ρ isopycnal is inflating or deflating – i.e. $G(\Theta, \rho)$ does not look like a streamfunction.

So there are two candidate streamfunctions, $\psi(\Theta, \rho)$ and $G(\Theta, \rho)$ in terms of which we might wish to consider zonally-integrated flow along surfaces of constant density. Both have deficiencies when the density structure is evolving: $\psi(\Theta, \rho)$ gives the incorrect diapycnal flow and $G(\Theta, \rho)$ the wrong isopycnal flow. However, the important thing is that $G(\Theta, \rho)$ has a clear physical interpretation, being the total flux of waters 'down' across the ρ isopycnal, north of Θ , and the deviation of $G(\Theta, \rho)$ from $\psi(\Theta, \rho)$ gives a simple and direct measure of the importance of unsteadiness.

Application to the Atlantic sector of a global model

We apply these ideas to the Atlantic sector of the Global Isopycnal Model, a 1.25° by 1.25° implementation (Marsh et al., 1998) of the Miami Isopycnal code (Bleck et al., 1992). After 30 years of spin-up, the lighter waters $\sigma \equiv \rho - 1000 < 27.5$ are almost in steady state, as can be seen from Fig. 2a, a contour plot of $\partial V(\Theta, \rho) / \partial t$. However, the densest layers, $\sigma > 27.75$, are losing mass at the expense of the intermediate waters $27.5 < \sigma < 27.75$, so $\partial V(\Theta, \rho) / \partial t$ is negative, reaching ~ -8 Sv for $\sigma \approx 27.75$ at

the southern boundary.

Let us now compare the overturning streamfunction, $\psi(\Theta, \rho)$, (Fig. 2b) with the transformation streamfunction $G(\Theta, \rho)$ (Fig. 2c). They are almost identical for the light waters $\sigma < 27.5$ which are in steady state. However, they differ for the deep waters. In fact there is negligible transformation of the dense waters south of 50°N , as is well shown (Fig. 2c) in the transformation streamfunction field, $G(\Theta, \rho)$, however, the mass released as the densest layers deflate is exported out through the southern boundary and is evident (Fig. 2b) in the overturning streamfunction, $\psi(\Theta, \rho)$. The overturning streamfunction $\psi(\Theta, \rho)$ thus gives a thermohaline cell of about 15 Sv – almost double the 8 Sv actually being transformed and which is evident in the transformation streamfunction, $G(\Theta, \rho)$.

Conclusion

The meridional overturning streamfunction integrated zonally on density surfaces gives a misleading picture of the watermass formation (particularly for the denser layers) in models that are drifting. We have shown here, however, that it is relatively simple to plot the ‘watermass transformation streamfunction’ which *does* give an accurate

picture of the watermass transformation. We believe that this watermass transformation streamfunction is a useful diagnostic for the many models which need to be studied while not in steady state.

Acknowledgements

Thanks to Alex Megann and Adrian New for allowing us to use data from the Global Isopycnal Model (GIM).

References

- Bleck, R., Rooth, C., Hu, D., and L. T. Smith, 1992: Salinity-driven thermocline transients in a wind- and thermohaline-forced isopycnal coordinate model of the North Atlantic. *J. Phys. Oceanogr.*, 22, 1486–1505.
- Döös, K., and D. J. Webb, 1994: The Deacon Cell and the other meridional cells of the Southern Ocean. *J. Phys. Oceanogr.* 24, 429–442.
- Marsh, R., A. J. G. Nurser, A. P. Megann, and A. L. New, 1998: Water mass transformation in the Southern Ocean of a Global Isopycnal Coordinate GCM. Submitted to *J. Phys. Oceanogr.*
- Speer, K. G., 1998: A note on average cross-isopycnal mixing in the North Atlantic Ocean. *Deep-Sea Res.*, 44, 1981–1990.
- Walín, G., 1982: On the relation between sea-surface heat flow and thermal circulation in the ocean. *Tellus*, 34, 187–195.

Summary of a GODAE/WOCE Meeting on Large-Scale Ocean State Estimation

D. Stammer, I. Fukumori, and C. Wunsch, Massachusetts Institute of Technology, Cambridge, MA, USA. detlef@lagoon.mit.edu

A workshop on large-scale ocean state estimation was held at the Johns Hopkins University in Baltimore, MD, 9–11 March 1998. The meeting was sponsored by WOCE and GODAE and was attended by over 30 participants from Europe, Australia, Japan and the US. The overall goal of the meeting was to identify critical issues hindering advances in large-scale ocean state estimation and to discuss approaches to resolving them, thereby stimulating progress from the present experimental stage to practical applications.

During the meeting groups and individuals shared experiences and problems in assimilation. General interests ranged from regional to global process studies, climate analyses, as well as operational product generation and forecasting for naval, commercial, and research purposes. The most common data type now being analysed is satellite altimetry, followed by temperature profiles and sea surface temperature fields. However, a full WOCE-type data synthesis is anticipated by several groups. In terms of numerical models, uncoupled z-level primitive equation ocean models are employed most, with limited emphasis on fully coupled climate models at present. The methods used to combine models with data are nearly equally divided among Kalman filters-smoothers, optimal interpolation, and adjoint methods.

Assimilation issues discussed at the meeting included:

- Uncertainties in meteorological forcing fields

- Prior model and data uncertainties
- Posterior estimation errors
- Measures of reliability
- Ocean model improvements
- Data streams
- Assimilation of uncommon data types
- Intercomparison of methodologies
- Predictability

Each topic was addressed by invited presentations followed by a discussion. The most urgent issue identified by many groups concerns modelling of prior model uncertainties. These are weights used in assimilation that in effect define the estimation problem and control its solution, and is related to several of the topics discussed above. In addition to the technical issues, an overview was given of recent major ocean state estimation programs. A summary report of the discussions is being prepared and will be published by the WOCE International Project Office.

Proposed steps following the meeting are

- (1) the establishment of a working group on data assimilation and
- (2) the initiation of a North Atlantic Pilot Assimilation Project.

Among the immediate activities of the working group would be to foster progress in the establishment of meteorological error estimates required for ocean modelling and

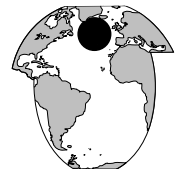
assimilation activities; to produce recommendations to the DACs regarding data products and their uncertainties useful for a data synthesis with specific focus on ocean state estimation; and to provide recommendations for model improvements most important in the context of large-scale ocean state estimation.

The purpose of the North Atlantic Pilot Project initiative is to contribute to a concerted WOCE AIMS

activity and to realise a GODAE pilot study with the goal to set up and test a real-time data system. Intercomparisons of assimilation results can help better understand results and to better identify effective observation, modelling and assimilation strategies. However, there is first a need in the assimilation community to understand and assess what can be learned from existing observations.

Cruise 36 of RV Professor Shtokman to the North Atlantic

A. V. Sokov and V. P. Tereschenkov, P.P. Shirshov Institute of Oceanology, RAS, Moscow; and S. A. Dobroliubov, Moscow State University. dobro@ocean.geogr.msu.su



Cruise 36 of RV Professor Shtokman to the North Atlantic took place from 3 October to 22 December 1997. The cruise was a Russian contribution to the final stage of WOCE 1997–98 field activity and the ACCE (Atlantic Climate Change Experiment) project.

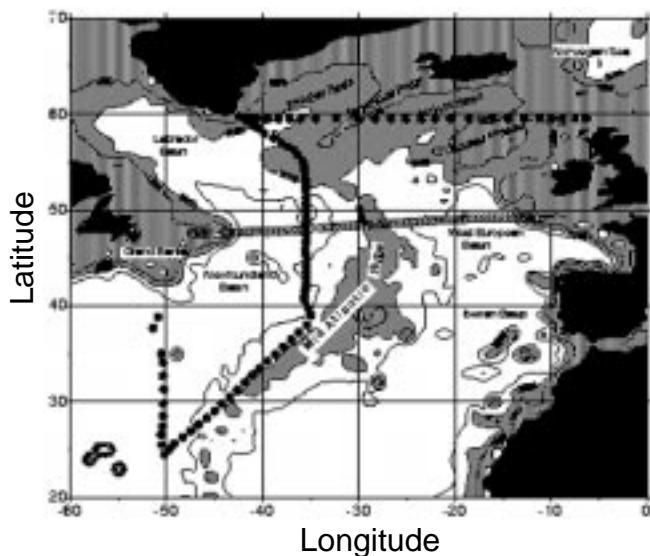


Figure 1. RV Professor Shtokman cruise 36 track. Position of CTD (•) and XBT(x) stations.

Cruise objectives were:

- to describe the contemporary thermohaline structure of the subpolar and subtropical gyres of the North Atlantic;
- to inspect the spatial variability of the water masses constituting the Northern and Western Deep Boundary Currents that provide return southward transport of modified surface waters from the high latitudes of the North Atlantic and adjacent seas of the Arctic Ocean;
- to determine the pathways of the Labrador Sea Water (LSW) from the source region in to the open ocean.

The observations were carried out at three hydrographic sections: a zonal section along 59.5°N, a meridional section along the western flank of MAR (AR5) and a meridional section along 50.5°W (AR13N). Overall 96 full depth CTD stations were occupied. Additionally, an XBT line along

48°N was occupied. The cruise track together with the station position is shown in Fig. 1.

At each CTD station continuous profiles of temperature and conductivity together with water samples from selected pressure levels were obtained. The water samples were then subjected to onboard laboratory determination of the sea water salinity and the oxygen content.

GO Mark-IIIC/WOCE CTD coupled with Benthos 2110 Altimeter and the GO Rosette multi-bottle array system (Model 1015), equipped with 24 x 2.5 l GO 1010 Niskin Bottles were used as primary tools to perform the above mentioned observations. Gohla Precision Unprotected and Protected Deep Sea Reversing thermometers were used to control the CTD pressure and temperature CTD measurements. All the equipment was kindly provided by the Bundesamt für Seeschifffahrt und

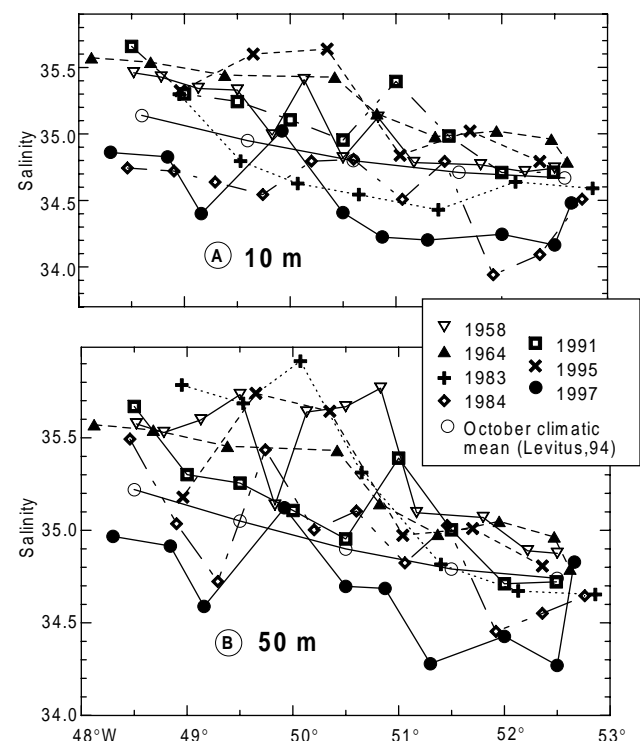


Figure 2. Salinity distribution at 10 m (a) and 50 m (b) levels in the area of Subpolar front on the AR5 section.

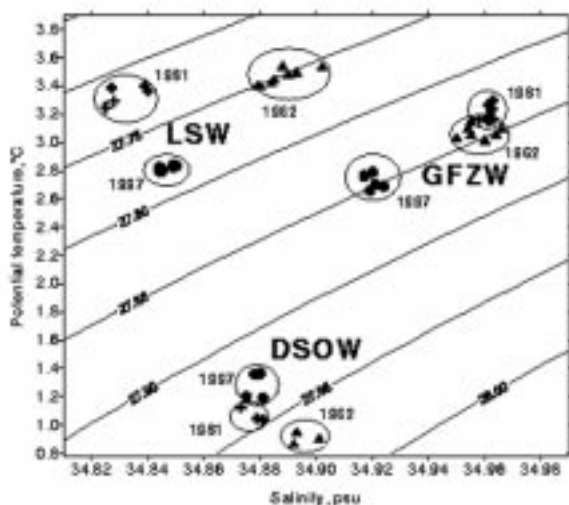


Figure 3. Water masses core properties.

Hydrographie (Hamburg, Germany).

For the needs of cruise planning a set of historical data has been collected. It incorporated observations gathered by the RV Erica Dan in 1962, RV Buffin in 1964, RV Knorr in 1983 and during the TTO (1981) and TOPOGULF (1983–84) experiments. Naturally, this provided an opportunity to infer the long term changes of ocean temperature and salinity structure in the survey area.

Preliminary results of such a comparison are as follows:

1. In October 1997 a negative salinity anomaly was spotted in upper 75 m layer in the region of North Atlantic subpolar front (in the latitudinal band 48°–52.5°N). The magnitude of the anomaly exceeds the well known Great Salinity Anomaly of the 1970–80s (Dickson et al., 1988). The observed salinity was 0.2–0.5 psu lower than the October climatic value (Fig. 2).
2. Significant changes of intermediate and deep water masses properties have occurred.

West of Reykjanes Ridge (in the Irminger and Newfoundland Basins) Gibbs Fracture Zone Water (GFZW) got warmer from 1962–64 to 1980s without any changes in salinity and after that till the beginning of 1990s it was subjected to profound both freshening and cooling of 0.04 psu and 0.4°C, respectively (Fig. 3). It is worth mentioning that in the Iceland Basin during the whole 1962–1997 time period GFZW experienced permanent freshening was accompanied by a less notable warming (not shown).

Changes of Denmark Strait Overflow Water (DSOW) were characterised by rather uniform behaviour. Thus, DSOW became warmer (0.2–0.3°C) and slightly fresher (0.02 psu) over the whole northern part of the North Atlantic (Fig. 3).

Continuing cooling of the LSW (0.5°C) was detected. This process is accompanied by the increase of the LSW layer thickness and density and by decrease of apparent oxygen utilisation seen all over the North Atlantic since the 1960s up to 1997. Freshening

(0.06 psu) of the LSW has occurred in the Irminger Basin during 1960s–1980s, and later on was followed by the increase of the LSW salinity (0.02–0.03 psu) (Fig. 3), which is in good agreement with the results of Dobroliubov et al., 1996; Koltermann and Sy, 1994; Read and Gould, 1992. At the same time in the Newfoundland Basin the freshening is still a prevailing tendency even today. The inconsistency in the LSW behaviour in different basins arises from different spreading time of the LSW from the formation region to certain locations (Koltermann et al., 1998).

3. Estimates of meridional mass transport across 59.5°N section show that the greatest flux of DSOW from Greenland Sea to the North Atlantic has occurred in 1981 (>11 Sv) and the lowest (7 Sv) in 1997. The maximum of the GFZW flux from the Norwegian Sea was detected in 1962 and 1997 and the minimum in 1982. The heat transport across 59.5°N to the east of Greenland was estimated to be 0.33 PW based on RV Professor Shtokman 1997 survey data. The calculations suggest that in the time period 1960–1997 intensification of Meridional Overturning Circulation (MOC) has occurred in early 1980s. This is in good agreement with the results of Koltermann et al. 1998 based on the analyses of the repeated 24.5°, 36° and 48°N zonal sections data.
4. The derived changes of the thermohaline structure suggest that at the phase of intensified MOC the preferable direction of the LSW spreading is north-east into the Irminger Basin, while at the period of reduced MOC the LSW moves more to the east and south east.

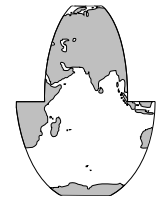
Acknowledgement

Cruise 36 of RV Professor Shtokman was funded by Russian Ministry of Science and Technology, Federal Research Programme “Research and development in the priority field of science and civil technology”, RFBR grants 95-05-16676 and 96-05-65059) and INTAS-RFBR-grant 95-972.

References

- Dickson, R. R., J. Meincke, S. A. Malmberg, and A. J. Lee, 1988: The “Great Salinity Anomaly” in the northern North Atlantic 1968–1982. *Progr. Oceanogr.*, 20, pp 103–151.
- Dobroliubov, S. A., V. P. Tereschenkov, and A. V. Sokov, 1996: Mass and heat fluxes at 36°N in the Atlantic: Comparison of 1993, 1981 and 1959 hydrographic surveys. *Int. WOCE Newsletter*, 22, pp 34–37.
- Koltermann, K. P., A. V. Sokov, V. P. Tereschenkov, S. A. Dobroliubov, K. Lorbacher, and A. Sy, 1998: A Decadal Changes in the Thermohaline Circulation of the North Atlantic. *Deep-Sea Res.* In press.
- Koltermann, K. P., and A. Sy, 1994: Western North Atlantic cools at intermediate depths. *Int. WOCE Newsletter*, 15, pp 5–6.
- Read, J. F., and W. J. Gould, 1992: Cooling and freshening of the subpolar North Atlantic Ocean since the 1960s. *Nature*, 360, pp 55–57.

TOPEX/POSEIDON Altimetry Captures Cycles of the Indian Ocean



Steven D. Meyers, Sujit Basu and James J. O'Brien, COAPS, Florida State University, Tallahassee, FL, USA. meyers@coaps.fsu.edu

Measurements of 1993–1996 sea-level variability in the Indian Ocean from the orbiting TOPEX/POSEIDON (TP) altimeter (Fu et al., 1994) reveal patterns of semiannual, annual and interannual cycles. These patterns are composed of both propagating and non-propagating features. Most off-equatorial sea level anomalies propagate westward as Rossby waves and equatorial anomalies propagate eastward as Kelvin waves. The seasonal cycle is found to be regular over the years examined, but the semi-annual (6 month) cycle is disrupted during 1994 for unknown reasons.

Gridded (1 degree by 1 degree) TP sea-level anomalies for 1993–1996 relative to the 4-year mean field were obtained from the Center for Space Research, the University of Texas at Austin (Tapley et al., 1994) from 10°S to 23°N and 40°E to 119°E. Subtraction of the 4-year mean effectively removes both the geoid and the mean currents, yielding a time-varying field dominated by the seasonal cycle. The average seasonal cycle is examined. Variability is also explored using Complex Empirical Orthogonal Functions (CEOFs, see Shriver et al., 1991), which breaks the data into a finite series of paired complex temporal and spatial functions. Here, the temporal functions are scalar functions in time and the spatial functions are scalar functions

depending upon latitude and longitude only. The product of each pair is referred to as a mode.

The seasonal cycle

The largest manifestation of the seasonal cycle in the Indian Ocean is the reversal of the monsoonal winds and the underlying ocean currents off Somalia. This TP dataset does not capture the Somali Current very well, probably due to the 1-degree gridding of the data. The average monthly sea level deviation indicates seasonal variability throughout the Indian basin. The average January sea-level from TP has positive and negative deviations from the mean state (Fig. 1) with spatial scales of several hundred to a few thousand kilometres. The south-west tip of India has a strong positive signal, corresponding to the Laccadive High (Bruce et al., 1994). West of India, the sea-level gradient indicates a northward current forming the eastern branch of an overall cyclonic circulation in the Arabian Sea. The winter circulation in the Bay of Bengal appears less coherent, though the eastern boundary appears to possess a coherent southward current. This current exits the Bay of Bengal with a strong westward component, loops

around the Laccadive High and moves northward into the Arabian Sea. This is a dramatic demonstration of the linkage between the two northern basins of the Indian Ocean.

Other features in January are the strong cyclonic circulations centred around 8°N just east of Somalia, and along the coast of Sumatra. Open isolines associated with the former feature are probably due to lack of coastal currents in the TP dataset. The Sumatra feature results from an eastward travelling upwelling Kelvin wave identified in longitude-time diagrams (not shown). A final feature is a weak anticyclonic circulation located round 10°S and 50°E.

The average July state is a rough opposite of the winter state. A relatively weak cyclonic circulation is found south of India. The eastern boundary current west of India has reversed direction and the overall circulation in the Arabian Sea now appears to be anticyclonic. The ocean off Somalia is also developing an anticyclonic motion. The central (65°E) equatorial region has a positive feature. This is the manifestation of the seasonally occurring downwelling Kelvin wave. The zonal structure along 10°S has been replaced by cross-meridional isolines in the westernmost part of the basin. The feature at 10°S and 50°E is now cyclonic.

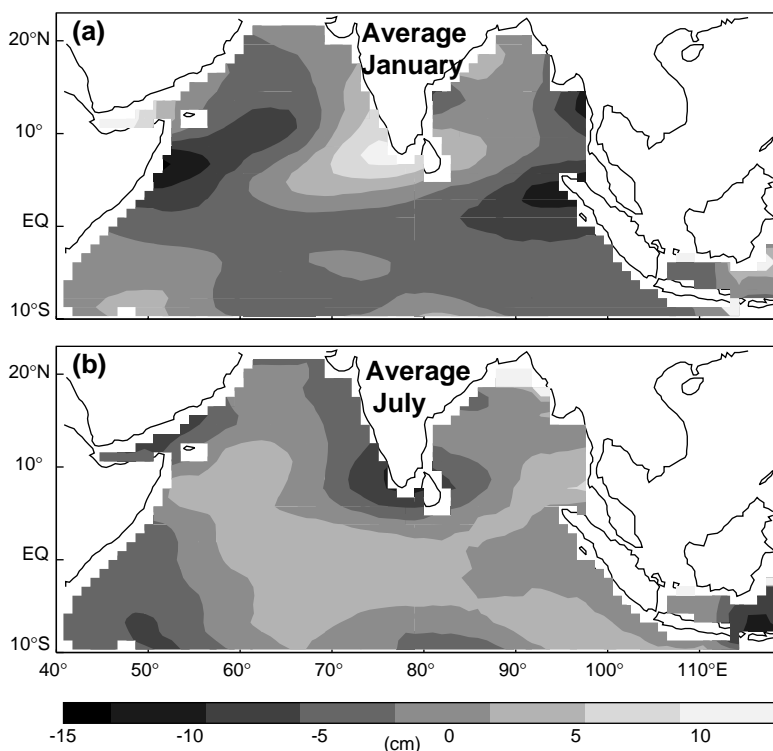


Figure 1. Monthly climatological average sea height from TOPEX. Deviations from a 4-year mean (a) January, (b) July. The grey scale bar indicated sea level in cm.

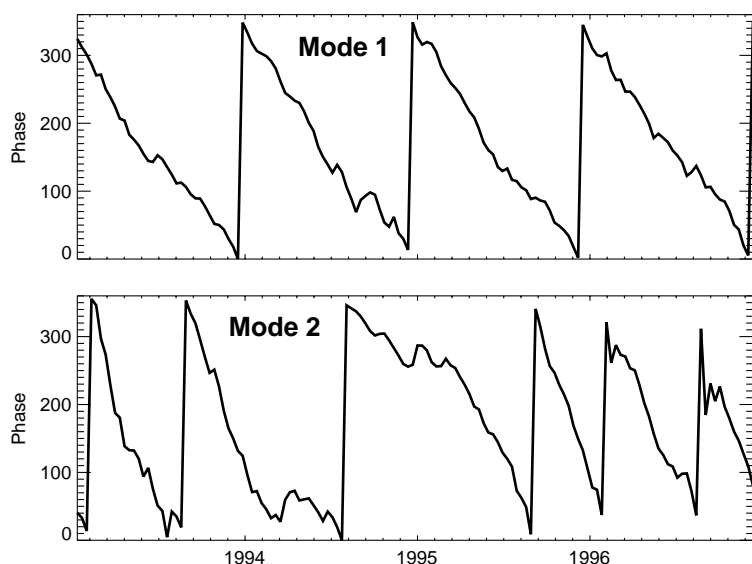


Figure 2. Phase of first and second mode temporal functions from CEOF analysis of TOPEX sea level variations.

The TP data are sufficient to resolve planetary wave propagation. The estimated phase speed of the equatorial Kelvin wave is 1.3 m/s (Basu et al., 1998). Westward propagating features are found at mid-latitudes and are identified as Rossby waves based on their location and propagation speed. In the eastern Arabian Sea the estimated speed at 15°N and 10°N is 17 cm/s and 25 cm/s, respectively.

CEOF analysis

The TP data are analysed using CEOF decomposition. The first mode, containing mostly annual variations, possesses about 42% of the total variance of the sea-level data. The second mode possesses about 24% of the total variance. The temporal phase of the first mode appears regular (Fig. 2). The phase rate of change is fairly constant with

little high-frequency fluctuation. The second mode has a semiannual frequency in the first and last year of the period of study. In the intervening time the dominant mode of variation is roughly a 1-year mode. To test whether this phenomenon is real or an artefact of the dataset, we used a 1.5-layer reduced gravity model of the Indian Ocean forced with the FSU winds. This type of model is known to faithfully represent the large-scale ocean currents and waves. The model sea level variations are also analysed with CEOF techniques. The first and second mode again display the annual and semi-annual cycle, respectively. The second mode possesses a nearly identical shift in the frequency of the temporal phase function. This implies the shift observed in TP data is real and is a wind-driven phenomena, since the only source of energy in the model is surface windstress.

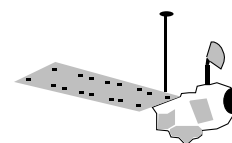
Orbiting altimeters continue to be powerful tools for studying the ocean circulation. New discoveries can be anticipated as multi-year records from existing instruments and their successor accumulate.

References

- Basu, S., S. D. Meyers, and J. J. O'Brien, 1998: Annual and interannual sea level variations in the Indian Ocean from TOPEX/POSEIDON observations and ocean model simulations. *J. Geophys. Res.*, submitted.
- Bruce, J. G., D. R. Johnson, and J. C. Kindle, 1994: Evidence for eddy formation in the eastern Arabian Sea during the northeast monsoon. *J. Geophys. Res.*, 99, 7651–7664.
- Fu, L.-L., E. J. Christensen, C. A. Y. Jr., M. Lefebvre, Y. Menard, M. Correr, and P. Escudier, 1994: TOPEX/POSEIDON mission overview. *J. Geophys. Res.*, 99C, 24,369–24,381.
- Shriver, J. F., M. A. Johnson, and J. J. O'Brien, 1991: Analysis of remotely forced oceanic Rossby waves off California. *J. Geophys. Res.*, 96C, 749–757.
- Tapley, B. D., D. P. Chambers, C. K. Shum, R. J. Eanes, and J. C. Ries, 1994: Accuracy assessment of the large-scale dynamic ocean topography from TOPEX/POSEIDON altimetry. *J. Geophys. Res.*, 99, 24,605–24,617.

The Along Track Scanning Radiometer Programme

Chris Mutlow, Rutherford Appleton Laboratory, Chilton, Didcot, Oxon. OX11 0QX, UK.
c.t.mutlow@rl.ac.uk



Following on from Victor Zlotnicki's interesting and useful article "Satellite Datasets for Ocean Research" in issue No. 30 of the WOCE Newsletter (1998), the purpose of this note is to inform the WOCE community of the new sea surface temperature (SST) and other data sets that are available to them from the Along Track Scanning Radiometer (ATSR) Programme.

The ATSR programme

The ATSR instruments are designed to provide: (1) a SST time series which will help establish if climate change is

taking place, (2) high spatial and temporal resolution SSTs for model validation, and (3) data for comparison with in situ observations of bulk SST, both for validation purposes and to understand the processes at the atmosphere-ocean interface.

The primary objective of the ATSR programme is to provide a long-term data-set of consistent and accurate observations of global SST to meet the needs of WCRP and the climate research community. To meet this goal the instruments were designed and built to meet the following objectives: (1) the measurement of SST averaged over 50 km by 50 km areas to an absolute accuracy of better than

0.5K (2σ) in conditions of up to 80% cloud cover, and (2) the generation of SST images with a pixel size of order 1 km square, and swath width 500 km, and relative pixel-to-pixel accuracy of 0.05K (2σ). The programme's secondary objectives include the provision of atmospheric parameters associated with aerosol, water vapour and cloud, as well as the measurement of land and ice surface radiances. With the addition of the vegetation channels on ATSR-2 and Advanced ATSR (AATSR), supplementary objectives include the assessment of the extent and seasonal variation of global vegetation, and evaluation of parameters such as leaf moisture and vegetation stress.

One of the features of the satellites that carry the ATSR series of instruments is that all the 1 km data collected by the sensor is stored on an on-board tape recorded at full resolution and down-linked to an ESA ground station each orbit. This has the advantage that the global data set from ATSR 1 km resolution is available from a single processing centre (i.e. the full resolution global 1 km data set is automatically collected during routine operations).

The ATSR instruments

The ATSR instruments are second generation space radiometers which build on the long heritage of the NOAA AVHRR sensors. ATSR exploits the multi-channel method pioneered in AVHRR but also uses new technology to improve instrument stability and calibration, detector signal to noise, and to provide observations of the same surface scene at two different angles. There are currently three ATSR instruments; all have a common specification, although there are some differences in the implementation. ATSR-1 was launched on the European Space Agency (ESA) ERS-1 satellite on 17 July 1991, as the test-bed for the ATSR concept. It carries infrared channels at 1.6, 3.7, 10.8 and 12.0 μm , and has no visible channels. Routine operation of ATSR-1 stopped when ERS-1 was put into hibernation in June 1996, but is still capable of operation, as even after nearly 7 years of use the S/N of the detectors is higher than a typical AVHRR at launch. The ATSR-2 and AATSR instruments are developments from the original ATSR-1 which, in addition to the ATSR-1's infrared channels, carry extra visible channels at 0.55, 0.67 and 0.87 μm for vegetation remote sensing.

ATSR-2 is flying on the ESA ERS-2 satellite, launched in April 1995, and is the current operational ATSR delivering SST and other data sets for users. AATSR will be launched towards the end of the decade on ESA's Envisat platform.

There was a significant overlap of the ATSR-1 and ATSR-2 missions, to allow cross-validation of the two sensors; it is expected that the ATSR-2 and AATSR missions will overlap similarly.

The ATSR-1 instrument and its unique features are described in detail in Edwards et al., 1990, and the visible channel additions to the ATSR-2 instrument are described in Gray et al., 1991.

Calibration

A key feature of ATSR sensors is their stable and accurate on-board calibration, a pre-requisite for providing a data set sensitive enough to support the detection of climate change. Each ATSR includes two ultra-stable black body targets for calibrating their infrared channels. Both these targets are viewed each scan, and their temperatures are set to cover the expected range of SST; one target is cold, usually around -10°C , and the other hot at around 30°C . The ATSR-2 and AATSR also include a visible calibration (VISCAL) system that provides a solar signal once per orbit for the calibration of the visible channels.

In addition to this in-flight calibration, each of the instruments has been subjected to a rigorous pre-flight calibration and characterisation to establish and test the sensor's key parameters and their stability. This testing is carried out by the scientists who use the final data, and who are independent of the instrument contractor.

Along track scanning

Application of the along track scanning technique is ATSR's most innovative feature, hence the sensor's name. Using this method, two observations of the scene are obtained through differing amounts of atmosphere; the "along track" view passes through a longer atmospheric path so is more affected by the atmosphere than the nadir view. By combining the data from these two views the ATSR provides a direct measurement of the effect of the atmosphere, thus yielding an improved atmospheric correction and overcoming the limitations inherent in nadir-only viewing instruments.

Instrument description

To use the along track method the ATSR's optical path is arranged to in a conical scan that provides two curved swaths that view the Earth's surface at different angles as the satellite orbits the Earth. First, the ATSR views the surface along the direction of the orbit track at an incidence angle near to 55° as it flies toward the scene. Then, some 150 seconds later, as the spacecraft passes over at the same point on the Earth's surface, ATSR records a second observation of the scene at an angle close to the nadir.

The forward/nadir view pairs of observations are used in the SST retrieval algorithm to generate the improved atmospheric correction.

ATSR's field of view comprises two 500 km-wide curved swaths, with 555 pixels across the nadir swath and 371 pixels across the forward swath. The nominal instantaneous field of view (IFOV) pixel size is 1 km^2 at the centre of the nadir swath and $1.5\text{ km} \times 2\text{ km}$ at the centre of the forward swath. Each pixel is the result of a 75 ms integration of the signal from the scene, calibration data is collected each 150 ms (i.e. each scan). The instrument's spectral channels are as described earlier in the text. This viewing geometry produces 500-km-wide

high-resolution infrared and, in the case of ATSR-2 and AATSR, visible images of the Earth's surface from which sea surface temperatures maps and other geophysical products can be retrieved through ground processing.

SST retrieval

Derivation of SST from ATSR makes use of either 2 infrared channels (10.8 and 12 μm), or all three infrared channels (3.7, 10.8 and 12 μm), and may use either one or both views. The selection of the set of coefficients to be used depends on the availability of the data. During the day a 2-channel retrieval is used.

The SST retrieval uses an algorithm that combines the brightness temperatures, T_i , from each channel, i , in the following way (after McClain et al., 1985):

$$T_{\text{SST}} = a_0 + \sum_{i=1}^N a_i T_i$$

where a_i are the retrieval coefficients derived from regression of brightness temperatures calculated from a large set of climatologically representative atmospheric temperature and humidity profiles using an atmospheric transmission model. The coefficients 'a' are given for three geographical regions: tropical, mid-latitude and polar, and also include a correction for the across track variation in airmass using 5 different across track bands. Full details of the retrieval method are given in Zavody et al., 1995.

Skin SST

Infrared radiometers observe the emission from, and hence the temperature of, the water layer within 0.1 mm of the surface. This layer is typically several tenths of a degree colder than the ocean a few millimetres beneath, and is known as the "skin" temperature.

The ATSR SST data are provided as a "skin" temperature rather than the pseudo-bulk temperatures that are provided by the AVHRR method of regressing satellite observation to buoy SST (see Mutlow et al., 1994; Zavody et al., 1995; and Murray et al., 1998, for further discussion of this). This approach has the advantage that, although the SST retrieval scheme includes climatological atmospheric data, the ATSR SST data set is independent of in situ bulk observation data set, unlike AVHRR.

Data quality

Considerable work has been done to validate the SST retrievals from the ATSR instruments through comparison with other data sets, including the NOAA blended analysis of AVHRR and in situ observations (see Mutlow et al., 1994; Zavody et al., 1995; and Murray et al., 1998, for further discussion of this).

From these it is clear that the ATSR instruments are delivering high quality "skin" SST data, to an accuracy and precision better than 0.5K (2σ), and that the technique of along track scanning brings considerable benefits,

particularly when 3.7 μm channel data is available. Recent results from ATSR-1 (see Murray et al., 1998) demonstrate that during the Mt. Pinatubo eruption the ATSR SST retrievals using the dual views at 3.7, 10.8 and 12.0 μm are relatively insensitive to the state of the atmosphere. The along track scanning method really does what the theoretical calculation predict, and is much less sensitive to errors in the modelling of atmospheric transmission than is the case for a nadir-only viewing instrument.

A CD-ROM containing the first 5-years of spatially-averaged SST data from ATSR-1 processed using the initial release of the algorithm can be obtained from the ATSR project at RAL.

Work on improving the retrievals continues, and this will result in a consistent ATSR-1, ATSR-2 and AATSR data set, an updated ATSR-1/2 data set will be released in late autumn.

Data products available

The following are a summary of the list of data products available to users from the ATSR instrument. These products come in two forms: (1) gridded image products covering a 512 km square area at the instrument resolution (nominally 1 km at nadir), and (2) spatially-averaged in latitude and longitude at 10 and 30 arc min resolutions.

The following gridded image products are available to user order: (1) brightness temperature/reflectance (GBT) images for all channels and views, and (2) retrieved SST (GSST) images. All ATSR images products are geolocated, the nadir and forward views are collocated, where appropriate, and contain cloud flagging information. A sample image showing the Gulf Stream given in fig. 1 (page 26).

The spatially-averaged products are ATSR's climate research products and are generated systematically by the project. The following are available: (1) spatially-averaged brightness temperatures and reflectances (ABT), separated into cloudy and clear pixels, and (2) spatially-averaged SST (ASST). A sample of a typical ATSR ASST 10 arc min composite is shown in fig. 2 (page 26).

How to get further information and order ATSR data

The ATSR Project is funded by the UK's Natural Environment Research Council, and is run by the ATSR Project team at the CCRLC's Rutherford Appleton Laboratory (RAL). Further information on the ATSR Programme can be obtained from: Dr Chris Mutlow, ATSR Project Scientist, RAL, Chilton, Didcot, Oxon., OX11 0QX, UK, Tel: +44-1235-446525, e-mail: c.t.mutlow@rl.ac.uk.

A CD-ROM containing the first 5-years of spatially-averaged SST data from ATSR-1 can be obtained from RAL.

The ATSR Project Web pages which contain the information on the programme are at <http://www.atsr.rl.ac.uk>. These pages also contain a link to

the UK ATSR Browse Facility which can be used to browse ATSR images before you order them.

ATSR data and full information on the all the products available readily available from ESA at: ERS Help Desk, Via Galileo Galilei, CP. 64, 0044 Frascati, Italy, Tel: +39-694180777, e-mail: irshelp@mail.esrin.esa.it, <http://www.esrin.esa.it>

It is also anticipated that ESA will start to operate a near-real-time service for ATSR images and spatially-averaged products later this year – watch the web pages for further announcements on this.

References

Edwards, T., et al., 1990: The along track scanning radiometer measurement of sea surface temperature from ERS-1. J. Br.

Interplanet. Soc. 43, 160–180.

Gray, P. F., et al., 1991: The optical system of the along track scanning radiometer MK II (ATSR-2). Proc. of ICSO '91, Toulouse.

McClain, E. P., W. G. Pishel, and C. G. Walton, 1985: Comparative performance of AVHRR-based multi-channel sea surface temperatures. J. Geophys. Res., 90, 11, 587–601.

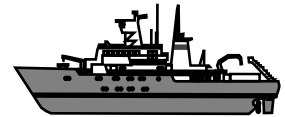
Murray, M. J., M. R. Allen, C. T. Mutlow, A. M. Zavody, T. S. Jones, and T. N. Forrester, 1998: Actual and Potential information in dual-view radiometric observations of sea surface temperature from ATSR. J. Geophys. Res., 103, 8153–8165.

Mutlow, C. T., A. M. Zavody, I. J. Barton, and D. T. Llewellyn-Jones, 1994: Sea surface temperature measurements by the along track scanning radiometer on the ERS-1 satellite: Early results. J. Geophys. Res., 99, 575–588.

Zavody, A. M., C. T. Mutlow, and D. T. Llewellyn-Jones, 1995: A radiative transfer scheme for SST retrieval for the ATSR. J. Geophys. Res., 100, 937–952.

At-Sea Test of a New XCTD System

Alexander Sy, Bundesamt für Seeschifffahrt und Hydrographie, Hamburg, Germany. sy@bsh.d400.de



Since the early days of WOCE it has been stated that the industrial production of expendable CTDs (XCTD) had to be extended with the accuracy and precision needed for large-scale measurement of heat and salt storage of the upper ocean in the WOCE voluntary observing ship programme. Comparative data from research vessels were to be used to check XCTDs accuracy (WCRP, 1988). As in the past we therefore took the opportunity of a WHP cruise in summer 1997 to test a new expendable device against a controlled and accurate CTD reference. The purpose of this kind of field evaluation is to check the manufacturer's claimed system performance independently, i.e. from a customer's point of view.

The new XCTD system tested was designed by Tsurumi-Seiki Co., Yokohama, Japan (TSK). It consists of a standard hand-held launcher, a digital converter (MK-100), a laptop PC and the expendable probe. The probe's nose contains the conductivity sensor and the thermistor. As is usual for expendable probes, depth is calculated by means of a depth fall rate formula and the elapsed time after the probe hit the water. Significant differences to Sippican's XCTD/MK-12 system are the higher sampling rate (25 Hz vs. 4 Hz) at about the same probe's drop speed and the use of an inductive conductivity sensor instead of an electrode type sensor.

A total of 24 calibrated XCTD probes were provided by TSK for this field test together with a complete deck's unit. The system's accuracy is claimed by TSK to be $\pm 0.02^\circ\text{C}$ (resolution 0.01°C) for temperature, $\pm 0.03\text{ mS/cm}$ (res. 0.017 mS/cm) for conductivity and $\pm 5\text{ m}$ (res. 0.17 m) or 2% for depth. The nominal depth range is 0–1000 m at a ship's speed of up to 12 knots. This accuracy is about an order of magnitude lower than the WOCE standard for CTD data so that XCTD quality deficiencies should be easily detectable.

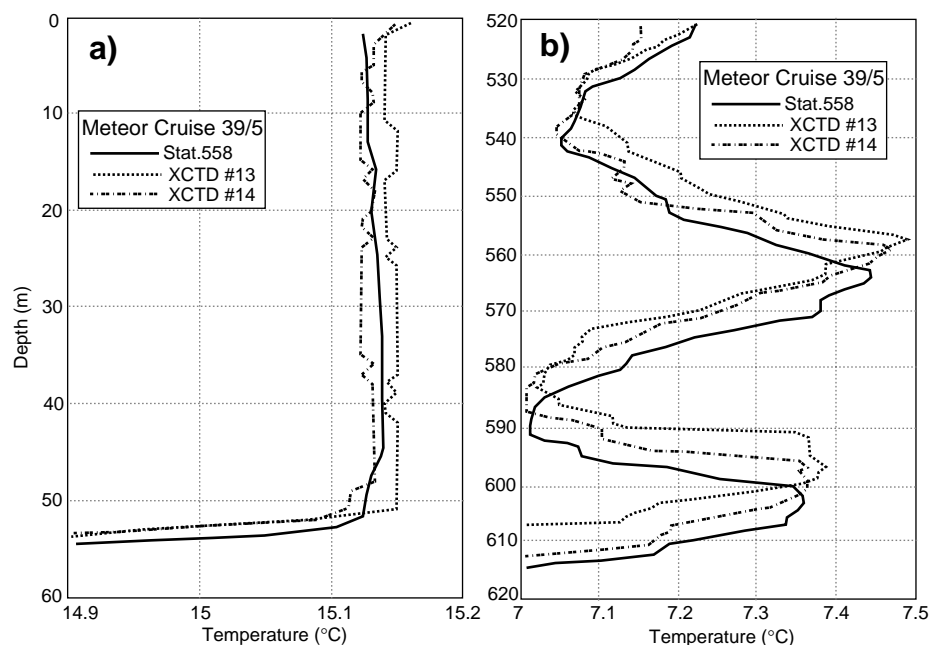


Figure 1. CTD and XCTD temperature profiles at stat. # 558, (a) upper 60 m, (b) deeper layers.

Operational details

The XCTD test sites are located in the eastern North Atlantic at WHP section A1/E from 52°N to 53.7°N and 17.1°W to 28°W. This area provides favourable conditions due to well developed hydrographic stratification in both temperature and salinity, which may be assumed to be sufficiently stable in relation to the time needed to drop 2 or 3 probes. The field test was carried out during “Meteor” cruise No. 39/5 from 2 to 9 September 1997 under good weather conditions with all 24 XCTD probes dropped at 9 regular CTD stations parallel with the down-profiling of a well calibrated NBIS MK-III B CTDO2 system. The test procedure was the same as that used in previous XCTD at-sea

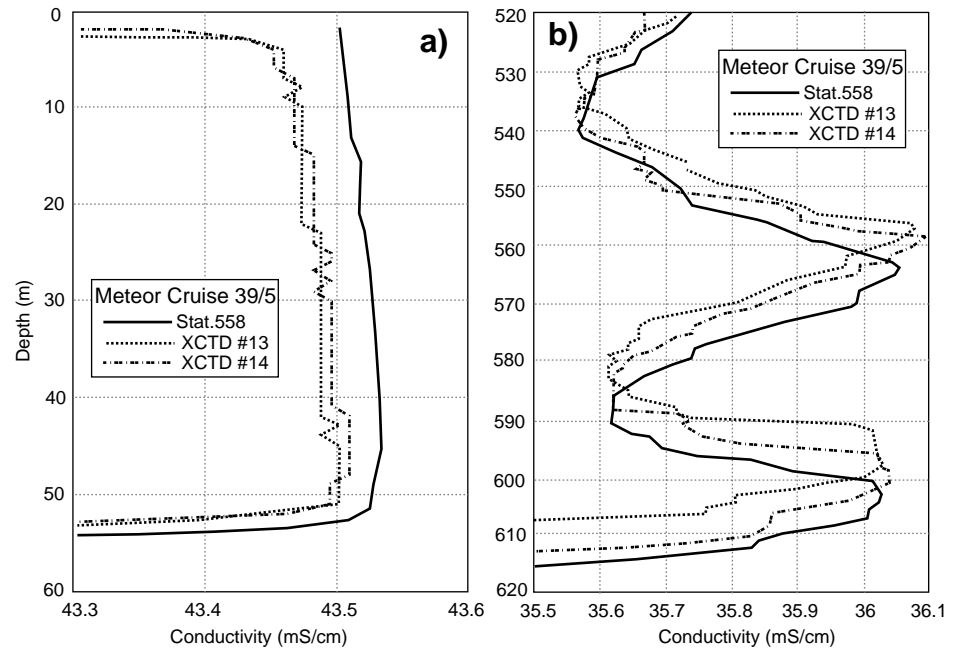


Figure 2. CTD and XCTD conductivity profiles at stat. # 558, (a) upper 60 m (c) deeper layers.

Table 1. Results on the accuracy of XCTD probes. Bold numbers mark where the accuracy found exceeded that given by the manufacturer. \pm means no significant deviation from CTD profile detectable.

XCTD Drop #	Mixed Layer			Thermocline (600–800 m)			Remarks
	ΔT [K]	ΔC [mS/cm]	Δz [m]	ΔT [K]	ΔC [mS/cm]	Δz [%]	
1							profile data lost
2	.01	-.02	1	\pm	\pm	-.6	
3	.01	-.01	-2	\pm	.01	.6	
4	\pm	-.03	-3	\pm	-.02	-1.5	
5	.01	-.02	2	\pm	.01	-.6	
6	\pm	-.04	-7	\pm	.01	-.8	fall rate too slow
7	\pm	-.02	\pm	\pm	\pm	-.3	
8	\pm	-.03	4	\pm	\pm	-.7	
9	\pm	-.03	13	\pm	\pm	2.2	
10	.01	-.03	1	\pm	\pm	-1.1	
11	.01	-.02	14	\pm	\pm	-.8	drop speed increase drop speed increase
12	.02	-.03	13	\pm	-.02	-1.1	
13	.01	-.04	-1	.02	\pm	-1.1	
14	-.01	-.03	-1	\pm	\pm	-.5	
15	.01	-.03	-2	\pm	\pm	\pm	
16	.01	-.03	-8	.01	\pm	-1.6	T drift below 450 m drop speed increase premature start
17	\pm	-.03	-2	\pm	.02	-1.0	
18	\pm	-.05	-1	.24	.01	-.4	
19	\pm	-.05	-4	\pm	-.02	-3.2	
20	\pm	\pm	40	.02	\pm	4.1	
21	\pm	-.05	-5	\pm	-.02	-.4	profile data lost
22	\pm	-.04	-4	\pm	-.01	-1.1	
23	\pm	-.04	-4	\pm	-.02	-1.1	
24							

trials (Sy, 1993; Sy, 1996). The temporal synchronisation of the CTD and XCTD profiles is close, lying mostly within a range of about 10 minutes. The CTD data were processed according to WOCE standards (WHP, 1994) and averaged to 1 dbar steps. XCTD data processing and averaging to 1 m steps was carried out by TSK's XCTD acquisition software.

All 24 probes were launched without mechanical problems. However, the acquisition software turned out to be extremely user-unfriendly so that the data of 2 complete profiles were lost due to handling errors. Also, the slow data saving procedures etc. proved to be disadvantageous for the test procedure because in order to keep up a close temporal relationship between CTD and XCTD traces only 2 to 3 probes could be dropped per station.

Test results

To obtain quantitative information that can be compared to manufacturer's numbers, data from the mixed layer and from

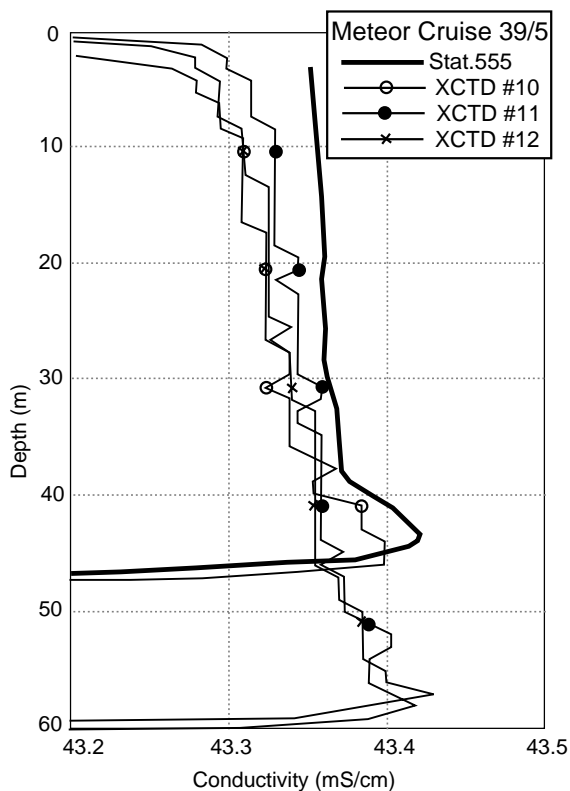


Figure 3. Example of a slow conductivity drift during the start phase and of too slow drop speed in the mixed layer.

the thermocline are investigated more closely for temperature (Fig. 1a, b) and conductivity (Fig. 2a, b). The homogeneous mixed layer is best for in-situ accuracy estimates, and the thermocline is essential for the depth fall rate evaluation. An overview of the test result is given in Table 1, with further details and remarks summarised as follows:

- All 24 probes dropped exceeded the full nominal depth/time range and covered 1059 m, i.e. no wire break or other serious malfunction like e.g. grounding problem occurred which would have terminated the measurement. That corresponds to a 100% successful drop rate.
- Data from 2 (presumably good) profiles (# 1, # 24) were lost due to software handling failures.
- Serious problems occurred in 2 drops. Temperature trace of drop # 18 started drifting at 450 m depth (thermistor insulation problem?) and the acquisition of drop # 20 started before the probe hit the water (noise problem?).
- Most probes started at a faster speed than defined but stayed within the specified depth error range of 2%.
- 3 profiles showed a significantly variable fall rate (speed of drops # 11, 12 and 19 increased with time). 1 probe descended from top to bottom slower than specified (drop # 9).

- 2 probes were faster than specified in the mixed layer (drop # 6, 16) and 3 probes were slower in the mixed layer (drop # 9, 11, 12 (Fig. 3)). Provided that these differences are not caused by short-term shifts of the mixed layer depth this may point towards hydrodynamic/stabilising problems or/and production intolerances.
- All temperature profiles (except the temperature drift event of drop # 18) are within the specified range in the mixed layer as well as in the thermocline (Fig. 1a, b).
- All conductivity profiles are within the specified range in the thermocline but 7 profiles are outside the accuracy range in the mixed layer by 0.01 to 0.02 mS/cm. The conductivity measurements show a drift between mixed layer and 600 m depth (average drift of 22 profiles = 0.03 mS/cm) which may point to a calibration problem (Fig. 2a, b).
- There is also some kind of small drift in conductivity within the mixed layer during the start phase which may point towards a (micro) air bubble problem (Fig. 3).
- All profiles show the probe's capability of very fast adaptation after entering the water (only about 5 m or less, Figs. 1a, 2a).
- A time-lag problem was not detected.
- The resolution was found as specified.

Conclusion

Taking everything into consideration the conclusion from this performance test is that the TSK XCTD system meets the claimed specifications. The system is close to providing the performance required by the oceanographic community for upper ocean thermal and salinity investigations. Although this development is too late for WOCE, it is just in time for the ongoing CLIVAR and GOOS programmes. The temperature is excellent, conductivity should be improved to achieve the same level as temperature, and the depth fall rate seems to be accurate. The variable fall rate of 3 from 24 probes, however, may point to some remaining hydrodynamical or stabilisation and/or production tolerance problems which have not yet been completely solved. Finally, the acquisition system has to be improved significantly to become a user-friendly, safe and acceptable system.

References

- Sy, A., 1993: Field evaluation of XCTD performance. WOCE Newsletter, 14, 33–37.
- Sy, A., 1996: Summary of field tests of the improved XCTD/MK-12 system, International WOCE Newsletter, 22, 11–13.
- WCRP, 1988: World Ocean Circulation Experiment Implementation Plan. WMO/TD No. 242 and 243. WOCE International Planning Office, Wormley, England.
- WHP, 1994: WOCE Operations Manual. WHPO 91-1, Rev. 1, November 1994. Woods Hole, MA, USA.

Note on Copyright

Permission to use any scientific material (text as well as figures) published in the International WOCE Newsletter should be obtained from the authors.

WOCE is a component of the World Climate Research Programme (WCRP), which was established by WMO and ICSU, and is carried out in association with IOC and SCOR. The scientific planning and development of WOCE is under the guidance of the Scientific Steering Group for WOCE, assisted by the WOCE International Project Office.

The International WOCE Newsletter is edited by Roberta Boscolo (roberta.boscolo@soc.soton.ac.uk) at the WOCE IPO at Southampton Oceanography Centre, Empress Dock, Southampton, SO14 3ZH, UK, Tel: 44-1703-596789, Fax: 44-1703-596204, e-mail: woceipo@soc.soton.ac.uk,

<http://www.soc.soton.ac.uk/OTHERS/woceipo/ipo.html>

We hope that colleagues will see this Newsletter as a means of reporting work in progress related to the Goals of WOCE as described in the Scientific Plan.

The editor will be pleased to send copies of the Newsletter to institutes and research scientists with an interest in WOCE or related research.